Author:
Lagos, Daniel A

Title:
Electronic Structure and Magnetic Properties of Transition Metal High Entropy Alloys

Electronic Structure and Magnetic Properties of Transition Metal High Entropy Alloys

Daniel Alejandro Lagos Llaguno

A dissertation submitted to the University of Bristol in accordance with the requirements for award of the degree of Doctor of Philosophy in the Faculty of Science

School of Physics

November 2019

Word Count:

42288

Abstract

The electronic structure and magnetisation of NiFeCoCr and NiFeCoCrPd high entropy alloys has been investigated. Using Ab-initio methods the momentum density of magnetic electrons and the magnetic structure of these alloys were determined. For this, special quasirandom structures and the coherent potential approximation were used for modelling the chemical disorder present in high entropy alloys. Also, magnetic Compton scattering experiments were done to validate the theoretical calculations.
The spin magnetic moment of NiFeCoCr and NiFeCoCrPd high entropy alloys have been measured by magnetic Compton scattering. Both theoretical methods overestimated the spin magnetic moment as was expected in transition metals alloys for the local density approximation and generalised gradient approximation level of density functional theory. The magnetic structure in these alloys shown most of the spin magnetic moments of Cr aligned in a opposite direction to the magnetic moments of the other elements. Previous works reports clustering or short range order of Cr in NiFeCoCr high entropy alloy. Analysing its magnetic Compton profiles this possible clustering has been discarded. Then, a ferrimagnetic structure in the strict sense is not possible in this compound.
Furthermore, the addition of Pd to NiFeCoCr high entropy alloy increased the spin magnetic moment of the resultant equiatomic alloy. The spin magnetic moment of NiFeCoCrPd high entropy alloy obtained by the special quasirandom structure method is close to the experimental value measured by magnetic Compton scattering.

Author's Declaration

I declare that the work in this dissertation was carried out in accordance with the requirements of the University's Regulations and Code of Practice for Research Degree Programmes and that it has not been submitted for any other academic award. Except where indicated by specific reference in the text, the work is the candidate's own work. Work done in collaboration with, or with the assistance of, others, is indicated as such. Any views expressed in the dissertation are those of the author.

D. A. Lagos
November 2019

Acknowledgments

First, I would like to thank to my supervisor Prof. Stephen Dugdale for his guidance and support of this research work. Next, I would like to acknowledge to my collaborator Mr. Daniel O'Neill for doing the experimental data analysis of the magnetic Compton profiles for NiFeCoCr and NiFeCoCrPd high entropy alloys. Also, many thanks to all my coworkers during the period between September 2016 and September 2019 at the office 4.28 of the H. H. Wills Physics Laboratory.
I want to express my gratitude to my family for their support and trust, especially to my mother Greta Llaguno. Thanks to my friends for their company, advice and doing my time more bearable in the United Kingdom.
Finally, I would like to thank to Secretaría de Educación Superior, Ciencia, Tecnología e Innovación (SENESCYT) for funding this study.

Contents

List of Figures

List of Tables

Glossary

Notation	Description	Page List
2D-ACAR	Two-Dimensional Angular Correlation of Annihilation Radiation	44
AE	All-Electron	29, 35, 36
APT	Atom Probe Tomography	67, 91
APW	Augmented Plane Wave	30–32, 37
ARPES	Angle Resolved Photon Spectrometry	53
ASA	Atomic Sphere Approximation	30, 43
ATAT	Alloy Theoretic Automated Toolkit	38–41, 69, 75, 85, 93, 98
BCC	Body Centred Cubic	vi, 8, 17, 29, 75
BFGS	Broyden-Fletcher-Goldfarb-Shanno	37, 69, 70, 85, 93
BSF	Bloch Spectral Function	viii, 65, 73, 75, 96
BZ	Brillouin Zone	vi, viii, ix, 8, 12, 13, 65, 66, 73, 78–82, 88, 101–107
CCA	Concentrated Complex Alloy	63, 67
CCD	Charge Coupled Device	53
CP	Compton Profile	3, 44–47, 51–53, 59, 66
CPA	Coherent Potential Approximation	2, 43, 69
DDSCS	Double Differential Scattering Cross Section	50, 52, 54–56, 59
DFT	Density Functional Theory	vii, viii, 2, 21, 22, 35, 37, 45, 67–71, 86, 92, 94
DOS	Density of States	vii, ix, 14, 17, 33, 65, 71, 72, 91, 95, 96, 105
DSP	Digital Signal Processing	58
EBS	Effective Band Structure	65, 73, 96
EDS	Energy Dispersive X-ray Spectrometry	67

Notation	Description	Page List
EMD	Electron Momentum Density	3, 21, 33, 44–46, 52, 66, 108
EMPW	Elliptical Multipole Wiggler	53, 55, 57
EMTO	Exact Muffin-Tin Orbitals	43
EMTO-CPA	Exact Muffin-Tin Orbital Coherent Potential Approximation	72
FCC	Face Centred Cubic	vi, 6, 8, 13, 17, 27, 63, 67, 73, 75, 76, 78, 91, 92, 98
FP	Full Potential	30
FP-LAPW	Full Potential Linearised Augmented Plane Wave	2, 29, 30, 33, 72
GGA	Gradient Generalised Approximation	2, 28, 29, 37, 76, 78, 89, 100, 101, 105, 108
GGA-PBE	Gradient Generalised Approximation Perdew Burke and Ernzerhof	69, 70, 85, 93
HCP	Hexagonal Closed Packing	75
HEA	High Entropy Alloy	vii–x, 2–4, 18–21, 43, 46, 53, 58, 63, 65–108
HEG	Homogeneous Electron Gas	26, 27
HK	Hohenberg-Kohn	22, 23
IA	Impulse Approximation	48, 50, 55
IBZ	Irreducible part of the Brillouin Zone	69, 70, 85, 93
IPM	Independent Particle Model	23
KKR	Koringa-Kohn-Rostoker	x, 2, 42, 43, 94
KKR-CPA	Koringa-Kohn-Rostoker Coherent Potential Approximation	vii–x, 43, 45, 65, 69–73, 75–77, 79–82, 87, 88, 93–95, 98–100, 102–107
KS	Kohn-Sham	2, 23–26, 29, 30, 32, 33, 37, 45
LAPW	Linearised Augmented Plane Wave	32
LDA	Local Density Approximation	vi, 2, 26–28, 37, 76, 78, 89, 100, 101, 105, 108
LDA-VWN	Local Density Approximation Vosko Wilk and Nusair	69, 93
LMTO	Linear Muffin-Tin Orbital	43

Notation	Description	Page List
LSDA	Local Spin Density Approximation	26, 27
MCA	Multi-Channel Analyser	58
MCP	Magnetic Compton Profile	viii, ix, 3, 44, 45, 47, 56, 57, 59, 61, 62, 69, 75–83, 86–89, 99–102, 105–108
MDME	Momentum Density of Magnetic Electrons	viii, ix, 2, 3, 44, 46, 47, 63, 66, 75, 78–82, 84, 85, 88–90, 101–107
MIR	Mott-Ioffe-Regel	92
NC	Norm-Conserving	35–37
OPW	Orthogonal Plane Wave	34
PAW	Projector Augmented Wave	2, 35, 65
PBE	Perdew Burke and Ernzerhof	28
PC	Primitive Cell	73, 75, 98
PDOS	Partial Density of States	vii, ix, 71–73, 95, 96
PK	Phillips and Kleinman	34, 35
PP	Pseudopotential	33–37, 69, 93
RAM	Random Access Memory	81, 82
SC	Supercell	65, 70, 73
SCF	Self Consistent Field	33
SDW	Spin Density Waves	14
SOC	Spin Orbit Coupling	70, 93
SP-CSA	Single Phase Concentrated Solid Solution Alloy	67
SPring-8	Super Photon ring 8 GeV	3, 52, 53, 66
SQS	Special Quasirandom Structure	vii–x, 2, 38, 39, 69–88, 93–107
SQUID	Superconducting Quantum Interference Device	57, 68, 92
SSD	Solid State Detector	58–60, 62
TM	Troullier and Martins	36
US	Ultrasoft	35, 37, 69, 93
UTS	Ultimate Tensile Strength	68
VTI	Variable Temperature Insert	59
VWN	Vosko Wilk and Nusair	43

Notation	Description	Page List
XMCD	X-ray Magnetic Circular Dichroism	x, 68, 70, 71, 88, 92–94, 105
XRD	X-ray Diffraction	4, 7, 9, 19, 67, 75, 98
YS	Yield Strength	68

Chapter 1

Introduction

Since ancient times mankind has been using metals to make a variety of objects, such as tools, weapons, jewellery, etc. The first metallic alloys appeared in the Bronze age [16]. Blacksmiths started to mix different metals and other elements with the aim to improve the properties of each pure element possesses by itself. These new materials gave a technological advantage to those civilisations which worked with them. Many of the alloys were developed empirically until the XX century. The development of quantum theory and the discovery of X-rays allowed an understanding of the microscopical structure of materials.

During the 1920s Hume-Rothery developed a set of rules that describes the conditions under which an element could dissolve in a metal and form a solid solution [17]. In 1926, Schrödinger proposed his celebrated equation making possible to understand the quantum nature of the matter [18]. After that, by 1928 Sommerfeld started to develop the electron theory of metals [19]. This model was successful explaining most of the Hume-Rothery rules [20]. However, the Hume-Rothery electron concentration rule could be explained only until 1936 by Mott and Jones using the ideas of Quantum Mechanics and the electron theory of Sommerfeld [21].

The simplest alloys are made with two different elements that means a binary alloy. In a binary solid solution, the element in bigger proportion is the solvent and the other element in smaller proportion is the solute. The magnetism of binary alloys has been studied experimentally. For instance, the Slater-Pauling curve collects the data of the ground state magnetisation of these alloys. Many theoretical models [22, 23, 24, 25] has been proposed by researchers to explain the

Slater-Pauling curve.

However, the study of magnetism can become a difficult task when the number of constituent elements in an alloy is greater than two and the definitions of solvent and solute are indistinguishable because their constituent elements can be in the same proportions. Nowadays thanks to development of high performance computing obtaining a quantum mechanical description of a solid like a High Entropy Alloy (HEA) is possible. For this, it is necessary to solve the many body problem resulting from the Schrödinger equation of the system. Also, the resulting theoretical calculations can be validated with X-ray experiments done in modern third generation synchrotron facilities.

The present work is focused in the study of magnetism in a couple of transition metal HEAs: NiFeCoCr and NiFeCoCrPd. The electronic structure of these alloys is elucidated through Density Functional Theory (DFT). From DFT, the key quantity to be determined is the Momentum Density of Magnetic Electrons (MDME) and its projections. The MDME help us to understand the origins of the magnetism in these HEAs. On the other hand, magnetic Compton scattering allows to get the one-dimensional projection of the MDME. In this way, it is possible to validate the electronic structure calculations and find limitations to the proposed theoretical approximations. Then, the configuration of this thesis is the following:

The second chapter presents basic concepts of crystallography at the beginning. Then, it is necessary to find a way to describe the behaviour of an electron in a metal. For this, the free electron model is presented. Also, the nearly free electron model and the Bloch theorem are described for developing the concept of Fermi surface. Hence, this work is focused in the magnetic properties of HEAs, the magnetism in transition metals and their alloys is discussed. Finally, the concept of HEAs is introduced and some of their properties are mentioned.

The third chapter introduces DFT. The methods used in this work to solve the Kohn-Sham (KS) equations are: the Full Potential Linearised Augmented Plane Wave (FP-LAPW), the Projector Augmented Wave (PAW) and the Koringa-Kohn-Rostoker (KKR). Also, the approximations for the exchange-correlation functional such as the Local Density Approximation (LDA) and the Gradient Generalised Approximation (GGA) are developed. On the other hand, the chemical disorder is tackled by the Coherent Potential Approximation (CPA) in the KKR method and also by a special supercell called Special Quasirandom Structure (SQS) jointly used with the FP-

LAPW method.

The fourth chapter presents to Compton scattering as a probe of the Electron Momentum Density (EMD). The theoretical details and the main equations of Compton scattering are developed. The concept of Compton Profile (CP) and Magnetic Compton Profile (MCP) are introduced. Also, the experimental details about the Super Photon ring 8 GeV (SPring-8) synchrotron and its Compton spectrometers are included. Finally, the data analysis for magnetic Compton scattering experiments is described step by step.

In the fifth chapter, the electronic structure of the equiatomic NiFeCoCr HEA is analysed. Also, the magnetic structure of this compound is discussed. The MCPs and the bi-dimensional projection of MDMEs are presented with the experimental data. On the other hand, the feasibility of short range ordering of Cr in NiFeCoCr HEA is analysed using magnetic Compton scattering.

In the sixth chapter Pd is added to the NiFeCoCr HEA. The electronic structure of the equiatomic NiFeCoCrPd HEA is analysed. The magnetic structure and the spin magnetic moment are determined. Also, the MCPs and the bi-dimensional projection of MDMEs of NiFeCoCrPd HEA are presented with the experimental data.

Finally, the results are reviewed and summarised in the seventh chapter.

Chapter 2

Electrons and Magnetism in Metals

In the present chapter, basic definitions are presented in order to describe the behaviour of an electron in a metal and also the origins of magnetism in metals and alloys. HEAs are crystalline alloys, then the mathematical description of the crystal lattice and the reciprocal space are fundamental for studying these complex materials. Also, a briefly description of X-ray Diffraction (XRD) is done owing to its historical and practical importance as a characterisation method of crystals.

The duality wave-particle of the electron shows its quantum nature. For this reason, the behaviour of an electron is well described by the Schrödinger equation. The Schrödinger equation is an expression of the energy conservation law in Quantum Mechanics. The potential energy term of this equation and the boundary conditions are modified to describe the electron dynamics inside a crystal lattice. In this way, the nearly free electron model, the Bloch theorem and Fermi surface are naturally introduced.

The role of spin to explain the presence of metallic magnetism in atoms is mentioned. Thus, the interactions between the spin of electrons in a crystal lattice results in the emerging of cooperative phenomena like ferromagnetism and antiferromagnetism. Also, the Stoner and the localised electron models are developed to explain the magnetism in some transition metal binary alloys. From those binary alloys where the magnetism is not explained by these theories emerges the necessity of a more complex theory that can satisfactory describe the magnetism in multicomponent alloys. Finally, the formal concept of HEA and its most important properties

are included.

2.1 Crystal Structure

A crystal is a periodic array of lattice points. A primitive cell is the periodic structure of minimum size in the lattice. A unit cell consist of a basis of atoms and a lattice. Translating a unit cell it is possible to determine the whole crystal structure. The lattice can be generated through a linear combination of basis vectors: $\mathbf{a_1}$, $\mathbf{a_2}$ and $\mathbf{a_3}$ in the following way:

$$\mathbf{R} = n_1\mathbf{a_1} + n_2\mathbf{a_2} + n_3\mathbf{a_3}, \tag{2.1}$$

where n_1, n_2 and n_3 are integers. Thus, every lattice point can be represented choosing a unique set of those integers. A basis of atoms must be associated with every lattice point. In three-dimensional space there are only fourteen possible ways of arranging identical points in a way that every one watch the same surroundings; those arrays are called Bravais lattices, see Fig. 2.1. For example, the Face Centred Cubic (FCC) structure has the highest possible density of packed

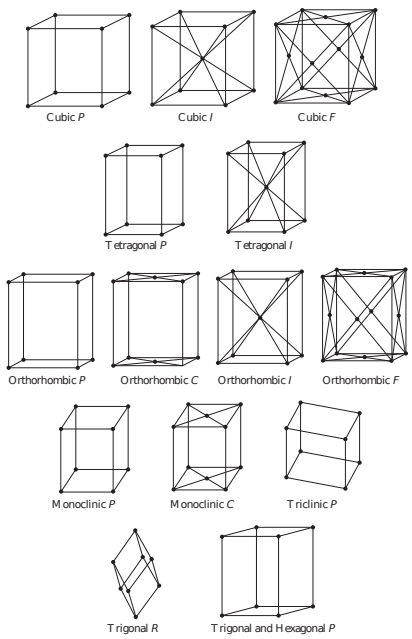

Figure 2.1: Bravais lattices in three dimensions. Cubic *F* corresponds to the FCC structure [1].

spheres. 24 elements crystallise in FCC structure. The nearest neighbours or coordination number for this array is 12.

2.2 The Reciprocal Space

Orientation, lattice vibrations, charge and momentum densities are just some quantities that could be obtained from crystals using different X-ray techniques. Indeed, one of the first techniques invented to characterise their properties was XRD. X-rays are useful to study arrays of atoms and molecules because their wavelength is in the order of the interatomic spacing. Therefore, X-ray experiments are in the quantum scale and the uncertainly principle must be considered during the measurements of the observables. Heisenberg expressed his uncertainly principle expressed in the following way [26]:

$$px - xp = \frac{h}{2\pi i} \tag{2.2}$$

where x is position and p the momentum. Here, these two variables are complementary, that means that the more precisely the position of a particle is determined, its momentum will be less precise. For example, in microscopy where is possible to recreate the image of a microscopic object recombining the rays scattered by the object through the lenses of the microscope [27]. Through this image it is possible to identify for example the morphology or constituent elements of the crystal. However, nothing can be asseverated about momentum related properties of the object at this scale through a direct space experimental technique. Thus, for studying the properties of crystals it becomes necessary to develop a technique associated with the momentum and so have a 'complete' [28] description of them.

Ewald (1913) and Laue (1914) were pioneers studying crystal properties in a space which is more convenient to work with momentum related quantities; this space is called the reciprocal space. As result of their experiences with XRD, they developed a notation for defining directions and crystallographic planes in this new reference system [29]. Thus, every point in reciprocal space could be expressed by a basis set of reciprocal lattice vectors $\mathbf{b_1}$, $\mathbf{b_2}$ and $\mathbf{b_3}$. Also, representing the periodicity of the crystal structure in reciprocal space could be done similarly to that in direct space.

$$\mathbf{G} = h\mathbf{b_1} + k\mathbf{b_2} + l\mathbf{b_3}, \tag{2.3}$$

where h, k and l are integers. The expression to relate the reciprocal lattice vectors $\mathbf{G}$ with the direct space vectors could be deduced from Bragg's Law, the Laue condition and the Fourier transform. All of them yield the same following expressions:

$$\mathbf{b_1} = 2\pi \frac{\mathbf{a_2} \times \mathbf{a_3}}{\mathbf{a_1} \cdot (\mathbf{a_2} \times \mathbf{a_3})}; \quad \mathbf{b_2} = 2\pi \frac{\mathbf{a_3} \times \mathbf{a_1}}{\mathbf{a_1} \cdot (\mathbf{a_2} \times \mathbf{a_3})}; \quad \mathbf{b_3} = 2\pi \frac{\mathbf{a_2} \times \mathbf{a_3}}{\mathbf{a_1} \cdot (\mathbf{a_2} \times \mathbf{a_3})} \tag{2.4}$$

For example, if one takes the FCC basis vectors in the direct space and using the Eq. 2.4 the resulting set of basis vectors generates a Body Centred Cubic (BCC) lattice in the reciprocal space. Now, connecting the central point of this BCC lattice to its nearby lattice points one gets eight line segments. Then, taking the midpoint between these connecting segments and drawing perpendicular planes to these bisections a volume is enclosed between those planes. The smallest volume constructed in this way is called the Wigner-Seitz cell. Therefore, the Wigner-Sietz cell of a BCC lattice in the reciprocal space corresponds to the first Brillouin Zone (BZ) of a FCC lattice in the direct space, as is shown in Fig. 2.2

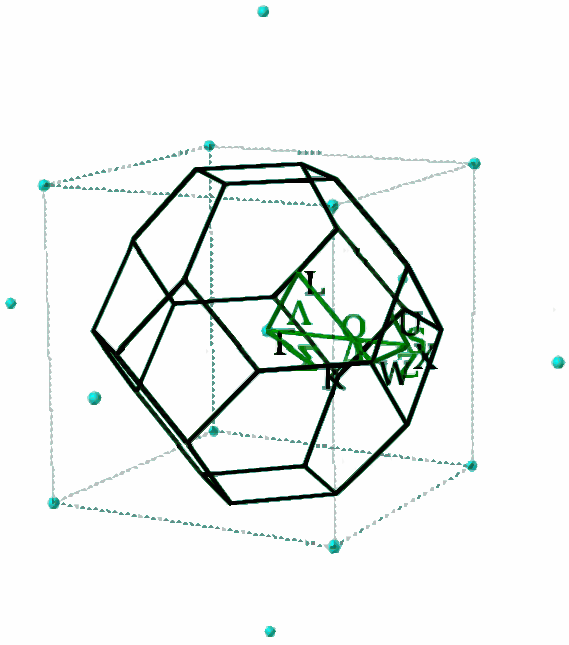

Figure 2.2: The first BZ of a FCC lattice with its high symmetry points labelled in black and the paths between them in green. The blue points in the reciprocal space reproduce a BCC lattice.

2.3 X-ray Diffraction

An XRD experiment consist of a X-ray beam hitting a crystal sample. Then, this incident beam is reflected (diffracted) by the crystal. Bragg formulated an explanation to this phenomena analysing the reflection of a collimated beam from flat crystal planes as is shown in Fig. 2.3. Constructive interference of diffracted beams is possible when the difference of optical paths is

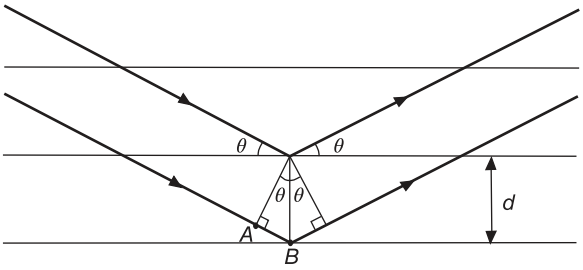

Figure 2.3: Diagram to derive the Bragg condition. d is the distance between crystallographic planes and θ is the incident angle [2].

an integer number n of wavelengths. Then, according to Fig. 2.3 the difference corresponds to $2AB$ where AB is the distance between the point A and B. Thus, $2AB{=}n\lambda$. Using the trigonometric relations to obtain an expression in function of the distance d between planes

$$n\lambda = 2dsin\theta \tag{2.5}$$

A similar situation will be fulfilled involving more than two planes. This expression is called the Bragg Law. From this, it is possible to infer that the upper limit on the wavelength is $\lambda < 2d$. Now, recreating the image of a microscopic object in reciprocal space is not a simple task like in the direct space because the recombination process of the scattered rays requires of a mathematical calculation [27]. There are three factors that intervene in the recombination of diffracted rays: direction, amplitude, phase. The direction of the beam is obtained identifying the Miller indices (*hkl*) of the crystal planes where the beam is diffracted. The amplitude is the Fourier transform of the scattering density $\rho(\mathbf{r})$ with respect to the scattering vector. However, there is no method available to measure the amplitude of each diffracted beam as a function of position and time. This drawback is known as the phase problem. Hence, in reality only the intensity of the beam can be measured, the phase is lost and the scattering density can not be

determined directly.

Applying mathematical methods is possible to get approximate phases of some X-ray reflections and thus reconstructing or solving the crystal structure. The key quantity that contains the information about the amplitude and phase of any X-ray reflection *hkl* is the structure factor defined as follows:

$$S_{hkl} = \sum_{\alpha} f_{\alpha} e^{-i\mathbf{G}_{hkl}\cdot\mathbf{r}_{\alpha}} \tag{2.6}$$

where $\mathbf{G}_{hkl}$ is the reciprocal lattice vector with components (*hkl*) which lies perpendicularly to the plane with the same indices (*hkl*) and f_{α} is the scattering factor of an atom located at $\mathbf{r}_{\alpha}$ within the unit cell. Moreover, the structure refinement consist in determining the phases of all X-rays reflections from known reflections. For this, an approximate structure can be proposed and its structure factor amplitudes are compared with the observed amplitudes.

2.4 Free Electron Model

The simplest approach to defining the Fermi surface in a crystal is using the free electron model inside an infinite potential well. In this model, electrons are confined in a cube of length *L*. Solving the Schrödinger equation (Eq. 2.7) for a free electron considering periodic boundary conditions results in a quantisation of the phase space.

$$-\frac{\hbar^2}{2m}\nabla^2\psi + V\psi = E\psi \tag{2.7}$$

The phase space correspond to a set of discrete points inside the cube. Each point of the phase space represents a state. Then, the wavenumbers k_x, k_y, k_z only can take values to represent those points. Thus, the wave function in a three-dimensional space takes the following form:

$$\psi(x,y,z) = \sqrt{\frac{1}{L^3}} e^{i\mathbf{k}\cdot\mathbf{r}} \tag{2.8}$$

A maximum of two electrons can occupy each point of the phase space as a consequence of Pauli exclusion principle. Electrons will occupy the available states following the Fermi-Dirac

distribution at finite temperatures.

$$f(E,T) = \frac{1}{1+e^{\frac{E-\mu}{K_B T}}} \tag{2.9}$$

Free electron energy dispersion relation, E(**k**), express the energy as a quadratic function of the wavevector $\mathbf{k}(k_x, k_y, k_z)$.

$$E(\mathbf{k}) = \frac{\hbar^2(k_x^2+k_y^2+k_z^2)}{2m} \tag{2.10}$$

Through this relation a constant energy surface is defined in a three-dimensional phase space, this spherical surface is the so called Fermi surface.

2.5 Bloch Theorem

The free electron model works well to describe the properties of metals which depends on the kinetic properties of conduction electrons, for instance: electrical and thermal conductivity and heat capacity. In this model the valence electrons of the constituent atoms become conduction electrons. Then, they can move freely many atomic distances through the volume of the metal. However, to generalize the concept of the Fermi surface in complex crystals is necessary to define our lattice using the spatial groups and a periodic potential which corresponds to the ionic attraction towards the electrons, see Fig. 2.4. This model is known as nearly free electron approximation.

In the nearly free electron model, solving the Schrödinger equation requires the application

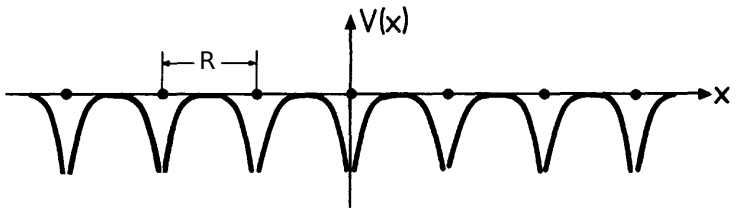

Figure 2.4: Schematic of a linear array of ions (solid ions) separated by a distance R and the corresponding periodic crystal potential $V(x)$ (solid curves).

of periodic boundary conditions. Then, the Bloch theorem states that the solutions of the

Schrödinger equation in three dimensions for an electron propagating in a periodic potential are plane waves multiplied by a periodic function $u_{\mathbf{k}}(\mathbf{r})$ with the same periodicity as the potential:

$$\psi_{\mathbf{k}}(\mathbf{r}) = e^{i\mathbf{k}\cdot\mathbf{r}} u_{\mathbf{k}}(\mathbf{r}) \tag{2.11}$$

where $u_{\mathbf{k}}(\mathbf{r})$ is a function with the periodicity of the crystal lattice and satisfies the relation

$$u_{\mathbf{k}}(\mathbf{r}) = u_{\mathbf{k}}(\mathbf{r}+\mathbf{R}) \tag{2.12}$$

where $\mathbf{R}$ is a lattice vector which defines the positions of each ion.

Then, the wavevectors $\mathbf{k}$ of each state terminate at points of the reciprocal space contained inside the first BZ. The shape of the BZ depends on the space group of the crystal.

As a consequence of the Bloch Theorem, the energy eigenvalues are periodic functions of the wavevectors $\mathbf{k}$, as follows

$$E(\mathbf{k}+\mathbf{G}') = E(\mathbf{k}) \tag{2.13}$$

where $\mathbf{G}'$ is an arbitrary reciprocal lattice vector. If one considers different values of the wavevector the positions of the energy levels change as well, and so a set of bands are obtained.

2.6 Fermi Surface

Electrons occupy the bands according to the Fermi-Dirac distribution in the nearly free electron model. At zero temperature, the Fermi energy is the energy of the topmost occupied state. The set of energy surfaces with an energy equal to the Fermi energy conform the Fermi surface. Then, this surface in the reciprocal space separates the occupied from the unoccupied electron states. Thereby, the Fermi surface will have a more complicated structure unlike the spherical shape of the free electron model. Fermi surface can be an open surface, close surface or present connectivity between other cells of the reciprocal space [30]. For example, the Fermi surface of Copper is represented in Fig. 2.5. The Fermi surface shape is influenced by the band structure of the metal and its interaction with the BZ. In a phase transition the Fermi surface can suffer modifications due to significant changes in the lattice constants and occupation number.

Models of electronic transport, thermal conduction, optical phenomenons, interactions of electrons with high magnetic fields are described through the Fermi surface. Therefore, the proper determination of the Fermi surface shape is important for the characterisation of the properties of metals and semiconductors because the dynamical properties of the electron depends where it is on the Fermi surface [31, 32, 33].

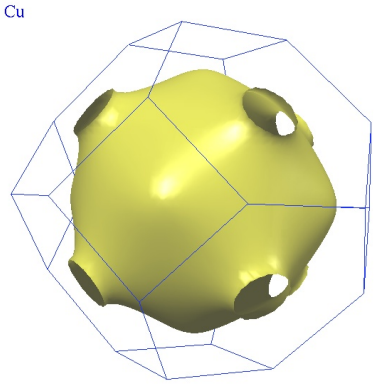

Figure 2.5: Fermi surface of Copper in yellow enclosed by its FCC BZ in blue [3].

2.7 Magnetism in Metals and Alloys

The electron has an intrinsic magnetic moment m_s due to a quantum property called spin s. Its spin magnetic moment is given by

$$\mathbf{m}_s = -g_e \frac{e}{2m_e c}\mathbf{s} \tag{2.14}$$

where $\mathbf{s}$ is the spin angular momentum of an electron with spin s=1/2, the constant g_e=2.0023 [5] is the g-factor of the electron, e electron charge, m_e electron mass and c speed of light. From the Eq. 2.14 the magnetic moment of the spin of an electron often called Bohr magneton can be defined as follows

$$\mu_B = \frac{e\hbar}{2m_e} = 9.274 \times 10^{-24} \quad [\mathrm{JT}^{-1}] \tag{2.15}$$

The spin of an electron plays a fundamental role in understanding magnetism. In a crystal the spins of electrons in each atom interact between them and also with an external magnetic field when this is available. There are three principal magnetic effects: paramagnetism, diamagnetism and cooperative magnetism. The first two could be analysed from the interactions of electrons in

a single atom with their nuclei but the last one only emerges when there are other atoms present. Ferromagnetism, antiferromagnetism and ferrimagnetism are the three magnetic cooperative phenomena. Transition metals are paramagnetic in the gas phase but in the solid phase some of them manifest ferromagnetism and antiferromagnetism. For instance, in the ground state: Fe, Ni, Co are ferromagnetic and Cr, Mn are antiferromagnetic [34]. These 3d transition metals have mobile unpaired electrons in the d-shell so they have a resultant magnetic moment **m**. Also, placing atoms of those magnetic metals in a crystal lattice their unpaired electrons interact between them because of exchange forces. In this way, the cooperative phenomena occurs aligning (parallel or antiparallel) the spins of magnetic carriers and binding their magnetics moments strongly [35]. A specific arrangement of the magnetic moments is called magnetic structure.

The metallic magnetism or itinerant magnetism could be explained by the Stoner model. Stoner used the molecular field concept to describe itinerant ferromagnetism. The molecular field produces an exchange potential which is due to Coulomb interaction. Thus, the exchange potential interacts with the electrons at the Fermi surface flipping their spins. Then, the atom reduces their energy changing the occupation of the spin bands and so it becomes ferromagnetic. The Stoner criterion for ferromagnetism is defined as follows:

$$g(E_F)U > 1 \tag{2.16}$$

where U is the exchange potential and g the Density of States (DOS).

On the other hand, antiferromagnetism could be explained through Spin Density Waves (SDW). SDW are oscillations in the magnitude of the spin and so antiferromagnetic order can occur. Cr is a typical example of SDW material.

Alloys are multicomponent systems which looks macroscopically homogeneous. The concentrations of the alloying elements can vary from tenths of percent to tens of percent [36]. It is possible to quantify the compositional disorder of an alloy by measuring the configurational entropy as a function of an order parameter. When the alloy has translational invariance or long range order this is an ordered alloy otherwise is a disordered alloy. However, disordered alloys may posses short range order [37, 36].

Disordered alloys in which its constituent elements are distributed randomly are called solid

solutions. Meanwhile, ordered alloys can be studied as single component crystals using the Bloch theorem, previous theoretical and experimental studies [38, 39] have shown that concepts like **k** vectors and Fermi surface derived from ordered structures can still be valid in solid solutions.

Bragg and Williams [40, 41, 42] developed one of the first successful models to explain the order-disorder transition in alloys induced by a change of temperature. Fig. 2.6a shows an arrangement of atoms composed by two metals A and B in equal proportion. It is possible to identify two sublattices formed by each specie. Thus, the positions occupied by A atoms are called α sites and the positions occupied by B atoms are called β sites. An A atom is called 'right' when is placed in a α site and 'wrong' when is in a β site. Similar criteria applies for B atoms.

The amplitude of thermal vibrations of the atoms increases when the alloy is heated. Then, some of the atoms acquire enough energy to leave their equilibrium positions and interchange positions with their nearest neighbours. This results in a certain number of atoms of both species becoming 'wrong' as is shown in Fig. 2.6c. The long range order is related with the amount of atoms placed in the 'right' sites. The long range order parameter, denoted by S, is defined as

$$S = \frac{r_\alpha - F_A}{1 - F_A} \tag{2.17}$$

where F_A is the fraction of atoms which are A atoms, r_α is the fraction of α sites still occupied by 'right' atoms. Then, $S = 1$ means a perfect order and $S = 0$ a perfect disorder.

The theory of Bragg and Williams does not consider the concept of short range order. This was later introduced by Bethe in his alloy theory [43]. Bethe considered interactions between pairs of atoms. The potential energy between pairs of atoms falls so rapid that the potential of an atom is only affected by those atoms which are nearest neighbours.

The short range order quantifies how well each atom is surrounded by unlikely neighbours. The fraction of pairs which are unlike is

$$q = \frac{Q_{AB}}{Q} \tag{2.18}$$

where Q_{AB} is the number of pairs AB and Q the total number of pairs in the lattice. Q depends of the number of atoms N and the number of nearest neighbours of each atom z as follows

$$Q = \frac{zN}{2} \tag{2.19}$$

Thus, the short range order parameter, represented by σ, is defined by

$$\sigma = \frac{q - q_{\text{rand}}}{q_{\text{max}} - q_{\text{rand}}} \tag{2.20}$$

where q_{max} is the maximum value of q at perfect order and q_{rand} a smaller value of q for a random arrangement of atoms. Therefore, the best ordered arrangement corresponds to a value of $\sigma = 1$ and the worst to $\sigma = 0$.

The perfection of short range order implies the perfection of long range order and conversely. Nevertheless, it is important to notice that in Fig. 2.6b. there are two domains separated by a line. The left side has perfect long range order and the right one does not have it. Then, $S = 0$ but $\sigma = 0.7$ and so the alloy presents certain short range order without any long range order.

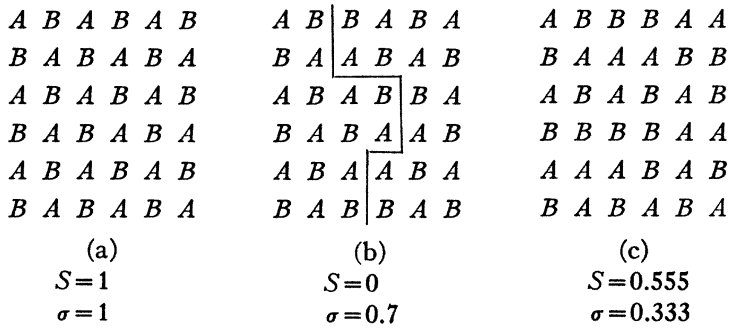

Figure 2.6: Bidimensional square lattices of metals A and B illustrating several degrees of large and short order in an alloy: (a) A lattice with perfect short and long range order. (b) A lattice with perfect long range order on the left side and without long range order on the right side. (c) A completely disordered lattice [4].

The simplest multicomponent system to analyse the magnetism is a binary alloy A_xB_{1-x}. For example, let A and B atoms of 3d transition metals and x is the atomic percent or the molar fraction. 3d transition metals can form binary alloys with an ordered or disordered structure depending on the composition and external variables like temperature or pressure [44, 45]. The

Slater-Pauling curve shows the ground state magnetisation of 3d transition metal binary alloys expressed as a function of the atomic concentration as shown in Fig. 2.7.

The three ferromagnetic elements Fe, Co, Ni have 4, 3, 2 vacancies in the 3d shell. According the

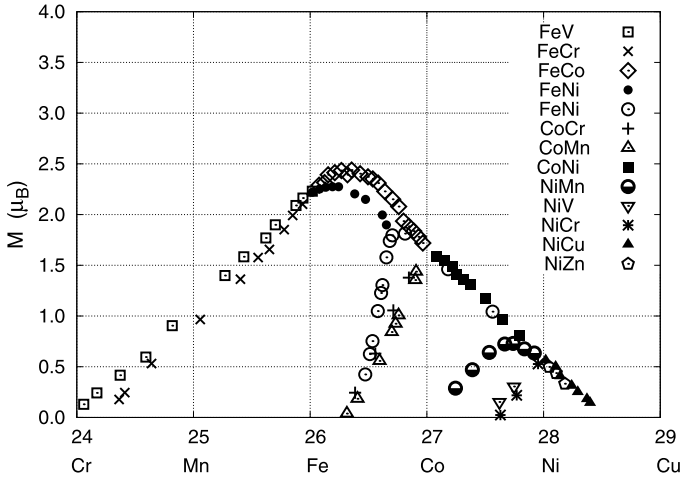

Figure 2.7: Slater-Pauling curve for 3d transition metal alloys as function of atomic number [5].

Hund's rules, one expects spin magnetic moments of 4, 3, 2 Bohr magnetons respectively [45]. However, they have non integer spin magnetic moments of 2.2, 1.7, and 0.6 instead. According to Stoner, only the itinerant behaviour of 3d electrons can explain these values hence changes in the occupation of the spin bands reduces the ground state energy of the atom compared with its non-magnetic phase. Here, the DOS curve preserves its shape in the magnetic and non-magnetic phase, this is also known as the rigid band model.

In the case of the binary transition metal alloys, the rigid band model works as well when all atoms are sharing a common 3d electron band, for example in Ni-Cu alloys. Other sections of the Slater-Pauling curve could be explained by a localised electron model where each atom contributes with a value equal to its individual spin magnetic moment multiplied by its concentration, for instance Co-Ni alloys. Also, at Z=26.7 the crystal structure of the alloys change from FCC (right side) to BCC (left side) independent of the component involved. A new structure corresponds to a different DOS curve, thus the filling of the spin bands will be different as well. Nevertheless, there are sections that can not be explained by any of the previous cases because it seems to be that the environment of the surrounding atoms affects the values of magnetic moment of each atom in the compound, such as Fe-Ni alloys [46]. Therefore, a more complex theory should be applied to explain the magnetic properties of transition metal alloys.

For this reason, Ab-initio methods plays a crucial role in the understanding of the electronic structure of multicomponent alloys and so making possible a better interpretation of their magnetic behaviour from a quantum mechanical perspective.

2.8 High Entropy Alloys

HEAs are alloys made of four or more elements having an equiatomic or close to equiatomic percentage. Atoms are placed in random positions along the crystal, thus each atom will be surrounded by different kinds of atoms, see Fig. 2.8. There are two main families of HEAs depending on if their essential elements are 3d transition metals or refractory metals. The 3d transition metal's family contains at least 4 or more of the following elements: Al, Co, Cr, Cu, Fe, Mn, Ni, Ti and V; meanwhile the refractory metals family contains 4 or more of the following elements: Cr, Hf, Mo, Nb, Ta, Ti, V, W, and Zr, plus Al [47]. The phase stability is

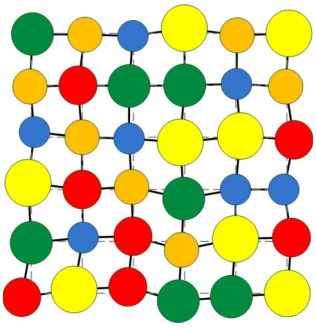

Figure 2.8: A scheme of a high entropy alloy. Each atomic specie has its own color [6].

granted through maximising the configurational disorder. Thus, atoms of distinct species form a homogeneous solid solution. Using the ideal solution model, the entropy of mixing per mole could be expressed as

$$\Delta S_{mix} = -R \sum_{n=1}^{n} c_i \ln c_i \tag{2.21}$$

where R is the gas constant, c_i the molar fraction of the ith element, n the total number of constituent elements. For an equiatomic alloy, all the elements are in the same proportion, the configurational entropy is given by

$$\Delta S_{mix} = -R\left(\frac{1}{n}\ln\frac{1}{n} + \frac{1}{n}\ln\frac{1}{n} + \cdots \frac{1}{n}\ln\frac{1}{n}\right) = -R\ln\frac{1}{n} = R\ln n \tag{2.22}$$

To design a high entropy alloy is convenient to take elements with similar atomic radius. For example, a common strategy is to take quartets with two neighbour elements of the same period of the periodic table and two more elements of the same group respectively. In an ample sense HEAs are single phase solid solutions which contains at least 4 principal elements in concentrations between 5% and 35%. The most common crystal structures for HEA are *cF4*-Cu ($Fm\bar{3}m$), *cI2*-W($Im\bar{3}m$) or *cP2*-CsCl ($Pm\bar{3}m$) [48].

There are four *core effects* present in HEAs: the high entropy effect, the lattice distortion effect, sluggish diffusion and the 'cocktail' effect. The high entropy effect could be explained from phase Gibbs' energy

$$G^{\emptyset} = H^{\emptyset} - T(S^{\emptyset}) \tag{2.23}$$

where $\emptyset$ could be a solid or a liquid phase. The entropy term $S^{\emptyset}$ not only contains the configurational entropy but also entropy terms from atomic vibrations, magnetic moments and electronic randomness. The high configurational entropy has a dominant effect over the other contributions [49]. On the other side, the enthalpy term $H^{\emptyset}$ could stabilise or destabilise the phase. However, in solid solutions entropy and enthalpy work together to stabilise the phase, this may favour the formation of solid solutions over intermetallic phases [50].

Lattice distortions will be present in HEAs because of atomic size difference, so strain and stress affect the crystalline structure. The displacement of each site depends on the atom occupying that site and the type of atoms surrounding it. Therefore, there will be a non-symmetrical bondings and electronic structure. Localised distortions around the solute atom will interact elastically with dislocations moving through the material, resulting in solid solution strengthening [50]. XRD experiments has shown a diminution of the peak intensity due to lattice straining because of an appearance of diffuse scattering. Strains present in HEAs increase the free energy of the lattice, helping to compensate the increment of the configurational entropy. Thus, phase stability and a severe strain can be achieved simultaneously [50].

Sluggish or slow diffusion kinetics in HEAs is originated by the fluctuations in potential energies of the lattice sites. The diffusing species could find difficulty in moving through the lattice because of temporary traps created by the different bonding configuration in each atom site and also by lattice distortions. The rate of diffusional phase transformation will be affected by sluggish diffusion because this phase transformation requires the cooperative diffusion between

the different species.

HEA's diffusion mechanism can be analysed using quasi-binary diffusion couples model described by Ficks' Second Law, and extending it to a n-component system [51]. This gives $(n-1)$ independent partial differential equations with their respective $(n-1)^2$ interdiffusion coefficients. Also, the temperature dependence of these diffusion coefficients could be determined by the Arrhenius equation. Then, it is possible to compare the diffusion of an element in different matrices. Unfortunately, there is not enough measurements of diffusion experiments in HEAs to confirm the slow diffusion rate of HEAs [50, 47, 52].

The cocktail effect opens the possibility to the appearance of unexpected properties from the combination of different elements. One of the most important motivations behind the engineering of alloys is to enhance the properties of an element mixing it with other elements. Also, it is possible to get a completely new average property from the mixture which is not present in any of their constituent elements. Properties of a composite not only come from its elements by mixture rule but also from the interactions between all the elements and from the severe lattice distortion. The properties of HEAs depends strongly on composition, electronic structure and microstructure. The cocktail effect in contrast to the other 'core effects' is not a hypothesis and it does need a proof [50].

A plethora of previous studies has been done to characterise the functional properties (thermal, electrical and magnetic), diffusion and mechanical properties. Furthermore, exotic properties has been reported in some HEAs like: high ductility, magnetocaloric effect, shape memory, excellent corrosion and wear resistance, great fatigue resistance and a high rate of β radiation scattering [53]. For these reasons, HEAs are an attractive area to research in physics nowadays.

Chapter 3

Ab-initio Electronic Structure Methods

The previous chapter has manifested the necessity of determining the electronic structure of a multicomponent alloy for a better understanding of its properties. This is not an easy task, since only solving the Schrödinger equation for an atom with more than one electron requires a numerical approximation. Therefore, an adequate quantum mechanical description of a many body system is fundamental to overcome this issue.

Ab-initio methods or from first principles methods allow the computational solution of the Schrödinger equation of many body systems like: atoms, molecules and solids. Nowadays, DFT has become a robust and accurate approach. Thereby, plane waves and Green's functions will be the essential pieces to formulate different methods within the framework of DFT in this chapter.

On the other hand, modelling the substitutional disorder present in a HEA for calculating its physical properties is crucial. For this purpose, a couple of options: a supercell method and a mean field theory are described in detail. Also, the relation between the EMD and the magnetic properties of a material is included.

3.1 Density Functional Theory

A crystal is modelled as a periodic array of atoms. In a crystal, the electrons are moving under the influence of Coulomb potential generated by the nuclei and the interaction forces between electrons. In order to solve the time-independent Schrödinger equation for this many body system, $\hat{H}|\Psi\rangle = E|\Psi\rangle$, the Hamiltonian of the problem is defined as follows:

$$\hat{H} = -\frac{\hbar^2}{2m_e}\sum_i \nabla_i^2 - \sum_{i,I}\frac{Z_I e^2}{|r_i - R_I|} + \frac{1}{2}\sum_{i\neq j}\frac{e^2}{|r_i - r_j|} - \sum_I \frac{\hbar^2}{2M_I}\nabla_I^2 + \frac{1}{2}\sum_{I\neq J}\frac{Z_I Z_J e^2}{|R_I - R_J|} \tag{3.1}$$

where the electrons are indexed with lowercase letters and nuclei with capital letters, Z and M are the nuclear charge and mass respectively.

To simplify the numerical calculations, the atomic unit system is defined such that $\hbar = m_e = e = 4\pi/\varepsilon_0 = 1$. Also, the nuclei of these atoms are considered static. This assumption of static nuclei is known as the Bohr-Oppenheimer approximation or adiabatic approximation [54]. Thus, the kinetic energy of the nuclei term is discarded and the last term in Eq. 3.1 which represents the interaction between nuclei becomes a constant. Therefore, only the terms related with the electrons remains as shown below

$$\hat{H} = \hat{T} + \hat{V}_{ext} + \hat{W} \tag{3.2}$$

where $\hat{T}$ is the electron kinetic energy, $\hat{V}_{ext}$ is the electron-nuclei energy and $\hat{W}$ is the electron-electron energy. DFT is one of the methods that can solve this many body problem.

The Hohenberg-Kohn (HK) theorems are the keystone of DFT. In this theory, the electron density is the key quantity to determine the electronic properties of the system. The first theorem establishes the existence of a one to one correspondence between the external potential $V_{ext}(\mathbf{r})$ in Eq. 3.2, the ground state $|\Psi_0\rangle$ which results from solving the Schrödinger equation and the associate ground state density $\rho_0(\mathbf{r})$, that is

$$V_{\text{ext}}(\mathbf{r}) \Longleftrightarrow |\Psi_0\rangle \Longleftrightarrow \rho_0(\mathbf{r}) = \langle\Psi_0|\hat{\rho}(\mathbf{r})|\Psi_0\rangle \tag{3.3}$$

Thus, $V_{ext}(\mathbf{r})$ including an additive constant, $|\Psi_0\rangle$ and $\rho_0(\mathbf{r})$ determine each other uniquely. Therefore, the ground state can be represented as a unique functional of the ground state density:

$$|\Psi_0\rangle = |\Psi[\rho_0]\rangle \tag{3.4}$$

The structure of the density is influenced by the geometry of the many particle system under study [55]. Also, any ground state observable can be represented as a functional of the ground state density. For example, the ground state energy is given by

$$E_0 = \langle\Psi[\rho_0]|\hat{H}|\Psi[\rho_0]\rangle = \langle\Psi[\rho_0]|\hat{T} + \hat{V}_{ext} + \hat{W}|\Psi[\rho_0]\rangle \tag{3.5}$$

where

$$F[\rho_0] = \langle\Psi[\rho_0]|\hat{T} + \hat{W}|\Psi[\rho_0]\rangle \tag{3.6}$$

Then, the functional $F[\rho_0]$ is universal because it does not depend on V_{ext}. This means that $F[\rho_0]$ is the same for atoms, molecules and solids.

The second theorem settles the Rayleigh-Ritz variational principle of the energy, so for any particular external potential V_{ext} corresponds its own ground state density ρ_0 and this density minimises the functional of the energy

$$E[\rho_0] = \min_{\rho} E[\rho] \tag{3.7}$$

where $E[\rho_0] = E_0$. Also, the functional of the energy has the following property:

$$E_0 < E[\rho] \text{ for } \rho \neq \rho_0 \tag{3.8}$$

Summarising, the HK theorems manifest three statements: invertibility, universality and variational access.

The KS approach basically replaces the many-body problem in Eq. 3.2 by an auxiliary independent particle problem. This is also called the Independent Particle Model (IPM). For this, there are two assumptions that need to be accomplished:

1. The exact V-representability of the density means the existence of a ground state density

of an auxiliary system of non-interacting particles equivalent to the ground state density of the interacting system.

2. The Hamiltonian of the auxiliary system must have the usual kinetic operator and an effective local potential $V_{\text{eff}}^{\sigma}(\mathbf{r})$ acting over an electron with spin σ at point $\mathbf{r}$ as below:

$$\hat{H}_{aux}^{\sigma} = -\frac{1}{2}\nabla^2 + V_{\text{eff}}^{\sigma}(\mathbf{r}) \tag{3.9}$$

Solving the N one-electron Schrödinger equations:

$$\left[-\frac{1}{2}\nabla^2 + V_{\text{eff}}^{\sigma}(\mathbf{r})\right]\phi_i^{\sigma} = \varepsilon_i^{\sigma}\phi_i^{\sigma} \tag{3.10}$$

each one of the N independent electrons in the system occupy one of the N^{σ} orbitals ϕ_i^{σ} in the ground state with the lowest eigenvalues ε_i^{σ} respectively. The eigenvalues ε_i^{σ} are assumed to be ordered as

$$\varepsilon_1^{\sigma} \leq \varepsilon_2^{\sigma} \leq \varepsilon_3^{\sigma} \leq \ldots \tag{3.11}$$

Thereby, the density of the auxiliary system can be expressed as a function of the KS orbitals ϕ_i^{σ} as follows

$$\rho(\mathbf{r}) = \sum_{\sigma}\rho(\mathbf{r},\sigma) = \sum_{\sigma}\sum_{i=1}^{N^{\sigma}}|\phi_i^{\sigma}(\mathbf{r})|^2 \tag{3.12}$$

Thus, the KS approach consists in rewrite the ground state energy of the many body interacting system of Eq. 3.1 as a functional of the density of the auxiliary system as shown below

$$E_{KS} = T_s[\rho] + \int V_{ext}(\mathbf{r})\rho(\mathbf{r})d\mathbf{r} + E_{Hartree}[\rho] + E_{II} + E_{xc}[\rho] \tag{3.13}$$

where T_s is the independent particle kinetic energy given as a functional of the KS orbitals, $V_{ext}(\mathbf{r})$ is the external potential due to the nuclei and other non-spin dependent external fields, E_{II} is an additive constant which represents the interaction between nuclei, $E_{Hartree}$ is the Coulomb interaction energy acting with itself defined as

$$E_{Hartree}[\rho] = \frac{1}{2}\int \frac{\rho(\mathbf{r})\rho(\mathbf{r}')}{|\mathbf{r}\text{-}\mathbf{r}'|}d^3\mathbf{r}d^3\mathbf{r}' \tag{3.14}$$

In Eq. 3.13, only the exchange-correlation term $E_{xc}[\rho]$ is not an explicit function of the density, but it could be approximated as a local or nearly local functional of the density. Also, the exchange-correlation functional groups all the many body effects of exchange and correlation not contained in T_s, $E_{Hartree}$ and E_{ext}.

Next, minimising the total ground state energy E_{KS} with respect to either the density $\rho(\mathbf{r},\sigma)$ or the effective potential $V^{\sigma}_{\text{eff}}(\mathbf{r})$ is possible to get the KS equations:

$$\left(-\frac{1}{2}\nabla^2 + V_{ext}(\mathbf{r}) + V_{Hartree}(\mathbf{r}) + V^{\sigma}_{xc}(\mathbf{r}) - \varepsilon^{\sigma}_i\right)\phi^{\sigma}_i = 0 \tag{3.15}$$

where ε^{σ}_i are the eigenvalues, then the effective Hamiltonian is given by

$$H^{\sigma}_{KS}(\mathbf{r}) = -\frac{1}{2}\nabla^2 + V^{\sigma}_{KS} \tag{3.16}$$

where V^{σ}_{KS} is the KS potential which gather the following terms:

$$V^{\sigma}_{KS} = V_{ext}(\mathbf{r}) + V_{Hartree}(\mathbf{r}) + V^{\sigma}_{xc}(\mathbf{r}) \tag{3.17}$$

For any interacting system there is a unique corresponding $V^{\sigma}_{KS}(\mathbf{r}) \equiv V^{\sigma}_{\text{eff}}(\mathbf{r})\big|_{\text{min}}$. The KS potential only gives the exact ground state density and energy of the interacting system. The KS potential must be found self-consistently with the resulting density from the KS orbitals. Also, KS orbitals are not true wave functions, so they do not reproduce the exact ground state Ψ_0 of the interacting system [56].

3.2 Local Density Approximation

As a consequence of the second KS theorem, the exchange-correlation energy depends only on the electron density. Thus, the exchange-correlation energy is represented as:

$$E^{LDA}_{xc}[\rho] = \int \rho(\mathbf{r})\varepsilon_{xc}[\rho(\mathbf{r})]\,d\mathbf{r} \tag{3.18}$$

where $\varepsilon_{xc}[\rho(\mathbf{r})]$ is an energy per electron at point $\mathbf{r}$ that depends on the density in some neighbourhood of the point $\mathbf{r}$. A system of electrons with constant density throughout all the space is called a Homogeneous Electron Gas (HEG), to describe its exchange-correlation energy, ε_{xc}, per electron there are several approaches from numerical and analytical methods, but in general the leading term is proportional to $\rho^{1/3}$ [57, 58]. In the KS approach, the electron density defined in Eq. 3.12 is obtained by summing over all occupied states according the Aufbau principle, that is filling the lowest available energy levels before filling the higher levels.

In a crystal, there is a certain electron density $\rho(\mathbf{r})$ at each point $\mathbf{r}$ in the space. LDA rests

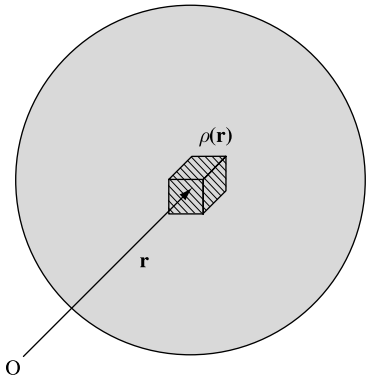

Figure 3.1: Illustration of the Local Density Approximation (LDA). The shaded volume is the immediate vicinity of the point $\mathbf{r}$. $\rho(\mathbf{r})$ is the electron density at $\mathbf{r}$ [7].

in two basic assumptions: the exchange and the correlation effects come principally from the immediate vicinity of a point $\mathbf{r}$ and these exchange and correlation effects do not depend strongly on the variations of the electron density in the vicinity of $\mathbf{r}$ [57]. Then, the exchange-correlation contribution can be calculated by integrating over the volume of the system the corresponding energy density calculated at the values that the electron density $\rho(\mathbf{r})$ assumes at every point $\mathbf{r}$ in the volume, this is shown in Fig. 3.1.

The exchange-correlation potential is related to the exchange-correlation energy by [59]:

$$V_{xc} = \frac{\partial E_{xc}[\rho]}{\partial \rho} \tag{3.19}$$

Considering the spin of the electron a more general expression for LDA called Local Spin Density Approximation (LSDA) can be formulated. Neglecting the correction of the non-

interacting kinetic energy [60], LSDA can be approximated as below

$$E_{xc}^{LSDA}[\rho\uparrow,\rho\downarrow] \approx \int d^3r(\varepsilon_x^{hom}[\rho\uparrow(\mathbf{r}),\rho\downarrow(\mathbf{r})] + \varepsilon_c^{hom}[\rho\uparrow(\mathbf{r}),\rho\downarrow(\mathbf{r})]) \tag{3.20}$$

where ε_x^{hom} and ε_c^{hom} are the energies per electron of the HEG for the exchange and the correlation respectively. The exchange per electron in a polarised system has the following form [61]

$$\varepsilon_x^{hom}(\rho,\zeta) = \varepsilon_x^{hom}(\rho,0) + [\varepsilon_x^{hom}(\rho,1) - \varepsilon_x^{hom}(\rho,0)]f(\zeta) \tag{3.21}$$

with

$$f(\zeta) = \frac{1}{2}\frac{(1+\zeta)^{4/3} + (1-\zeta)^{4/3} - 2}{2^{1/3} - 1} \tag{3.22}$$

where $\zeta = (\rho\uparrow - \rho\downarrow)/\rho$ is the relative spin polarisation. Then, the correlation per electron is defined as [61]

$$\varepsilon_c^{hom}(\rho,\zeta) = \varepsilon_c^{hom}(\rho,0) + [\varepsilon_c^{hom}(\rho,1) - \varepsilon_c^{hom}(\rho,0)]f(\zeta) \tag{3.23}$$

LDA is normally an accurate method for metallic systems where the electrons have a nearly free behaviour. However, it can present problems if it is applied in systems with strongly varying electron densities for example in finite systems like atoms where the density continuously approaches to zero outside the atom [55].

3.3 Generalised Gradient Approximation

One of the most famous failures of the LDA approximation that shows the necessity of a new approximation was the prediction of the ground state of Fe as paramagnetic FCC. The non-local nature of magnetic interactions in Fe makes LDA not applicable [62, 63]. To find a solution to this problem a LDA exchange-correlation energy correction using the gradients of the density was proposed. Thus, the new exchange correlation energy could be expressed as

$$E_{xc} = E_{xc}^{LDA} - \Delta E_{xc} \tag{3.24}$$

where ΔE_{xc} is the non-local contribution of the LDA exchange-correlation energy. A first attempt to correct the inhomogeneity of the LDA approximation in terms of a gradient expansion was done through a Taylor expansion of ΔE_{xc} [55]. For this, a weakly inhomogeneous electron gas is considered which means that all density gradients of the electron gas are small. As a result, only the exchange term was significantly improved compared with the original LDA but the correlation term presented worse results than LDA. Also, this gradient expansion gives a wrong ground state of Fe as well [64].

However, by applying a regularisation to ΔE_{xc} [65, 66] it is possible to define the GGA functionals as follows

$$\xi = \left(\frac{\nabla \rho(\mathbf{r})}{2[3\pi^2 \rho(\mathbf{r})]^{1/3} \rho(\mathbf{r})} \right)^2 \tag{3.25}$$

$$\Delta E_{xc}[\rho] = \int d^3 r \varepsilon_x^{hom}(\rho) \xi g_{xc}(\rho, \xi) \tag{3.26}$$

$$g_{xc}(\rho, \xi) = \begin{cases} C_{xc}(\rho) & for \quad \xi \to 0 \\ 0 & for \quad \xi \to \infty \end{cases} \tag{3.27}$$

where ξ is the dimensionless density gradient and C_{xc} is the gradient coefficient. Therefore, according to the Eq. 3.24 the spin-dependent exchange-correlation energy for the GGA adopts the form

$$E_{xc}^{GGA}[\rho\uparrow, \rho\downarrow] = \int d^3 r F_{xc}(\rho\uparrow, \rho\downarrow, |\nabla\rho\uparrow|, |\nabla\rho\downarrow|, ...) \tag{3.28}$$

where F_{xc} is a dimensionless enhancement factor that modifies the LDA expression according to the variation of the density in the vicinity of a considered point. There are many ways to define F_{xc}, the right choice depends on the observable to be determined and the system to be analysed: atom, molecule or solid. For bulk metals, the Perdew, Burke and Ernzerhof (PBE) GGA satisfies energetically conditions of the gradient-corrected non-locality. Here, the exchange-correlation energy can be separate as the sum of the exchange and correlation terms. Then, the correlation contribution has the following form [67]

$$E_c^{GGA}[\rho\uparrow, \rho\downarrow] = \int d^3 r \rho(\mathbf{r}) [\varepsilon_c^{hom}(r_s, \zeta) + D(r_s, \zeta, t)] \tag{3.29}$$

where $r_s = (3/4\pi\rho)^{1/3}$ is the radius of a sphere containing exactly one electron and it is called local Seitz radius, ζ is the relative spin polarisation and $t = |\nabla\rho|/2\phi k_s \rho$ is a dimensionless

gradient. Here, $k_s = \sqrt{4k_F/\pi a_0}$ is the Thomas-Fermi screening wave number, $\phi(\zeta) = [(1+\zeta)^{2/3} + (1-\zeta)^{2/3}]/2$ is the spin-scaling factor. Then

$$D = \left(\frac{e^2\gamma\phi^3}{a_0}\right) ln\left(1 + \frac{\beta t^2}{\gamma}\left[\frac{1+At^2}{1+At^2+A^2t^4}\right]\right) \tag{3.30}$$

where

$$A = \frac{\beta}{\gamma}\left[e^{\left(\frac{-\varepsilon_c^{hom} a_0}{e^2\gamma\phi^3}\right)} - 1\right]^{-1}, \tag{3.31}$$

$a_0 = \hbar^2/me^2$, $\beta = 0.066$ and $\gamma = 0.031$. Next, the exchange energy is defined by

$$E_x^{GGA}[\rho\uparrow, \rho\downarrow] = \int d^3r\rho(\mathbf{r})\varepsilon_x^{hom}(\rho)F_x(r_s,\zeta,s) \tag{3.32}$$

where $F_x(r_s,\zeta,s)$ is the spin polarised enhancement factor and $s = |\nabla\rho|/2k_F\rho$ is a dimensionless density gradient. If $\zeta = 1$ and $r_s \to 0$ then $F_x(r_s,\zeta,s) \to F_x(s)$. Here, $F_x(s) = 1 + \kappa - \kappa/(1 + \mu s^2/\kappa)$ with $\kappa = 1.245$ [68] and $\mu = 0.235$. Therefore, if s=0 then $F_x = 1$ and the local approximation is recovered and when $s \to \infty$ then $F_x = constant$.

GGA produces larger lattice constants, which implies a reduction of the bulk moduli. Thus, it predicts the right ground state of Fe as ferromagnetic BCC [64]. Also, the non-local nature of GGA affects the stability of the valence and semi-core spin states, and therefore the magnetisation [55].

3.4 Full Potential Linearised Augmented Plane Wave Method

Electrons are described by plane waves in the Bloch theorem, this way to represent electrons being the simplest and intuitive in condensed matter physics. The interaction of the screened nucleus with the electron is modelled using an attractive potential.

The Elk code is an All-Electron (AE) open source software oriented to calculate the electronic structure of crystalline solids. It uses the FP-LAPW method. Elk can solve the KS equations (Eqs. 3.15 and 3.16) for external fields such as: V_{ext}, $\mathbf{B}_{ext}$, $\mathbf{E}(\mathbf{r})$=-$\nabla V(\mathbf{r})$ and $\mathbf{A}$. The solution of

KS equations are done in two steps: In the first-variational step, Elk solves the KS equation with the following Hamiltonian [69]:

$$\hat{H} = \hat{T}_s + \hat{V}_{ext} + \mathbf{E}\cdot\hat{\mathbf{r}} + \hat{V}_{xc} \tag{3.33}$$

where $\hat{T}_s$ is the kinetic energy, $\hat{V}_{ext}$ is the external potential, $\mathbf{E}$ is the electric field and $\hat{V}_{xc}$ is the exchange-correlation potential. Then, Eq. 3.33 is diagonalised with $\hat{H}|\phi_i\rangle = \varepsilon_i|\phi_i\rangle$ where ϕ_i is a KS orbital and ε_i is an eigenvalue of the energy. Next, in the second-variational step the magnetic fields, spin orbit coupling and $\mathbf{A}$ vector potential are aggregated using the first-variational step as a basis:

$$H_{ij} = \varepsilon_i\delta_{ij} + \langle\phi_i|\,\boldsymbol{\sigma}\cdot\left(\hat{\mathbf{B}}_{ext} + \hat{\mathbf{B}}_{xc}\right) + \boldsymbol{\sigma}\cdot\hat{L} + \mathbf{A}\cdot\hat{\nabla}\,\big|\phi_j\big\rangle \tag{3.34}$$

where σ is a Pauli spin matrix and $\hat{L}$ the orbital angular momentum. Elk do not separate the KS equations into spin-up and spin-down orbitals, densities and potentials, instead Elk treats magnetism as non-collinear which depends on the scalar density $\rho(\mathbf{r})$ and the magnetisation field $\mathbf{m}(\mathbf{r})$. For this purpose, it requires variational spinor wavefunctions [69]:

$$\phi_{i\mathbf{k}}(r) = \begin{pmatrix} U^{\uparrow}_{i\mathbf{k}}(\mathbf{r}) \\ U^{\downarrow}_{i\mathbf{k}}(\mathbf{r}) \end{pmatrix} \times e^{i\mathbf{k}\cdot\mathbf{r}} \tag{3.35}$$

thus the density and the magnetisation are given by $\rho(\mathbf{r}) = \sum_{i\mathbf{k}} \phi^{\dagger}_{i\mathbf{k}}(\mathbf{r})\cdot\phi_{i\mathbf{k}}(\mathbf{r})$ and $m(\mathbf{r}) = \sum_{i\mathbf{k}} \phi^{\dagger}_{i\mathbf{k}}(\mathbf{r})\sigma\phi_{i\mathbf{k}}(\mathbf{r})$ respectively. Also, Elk calculates systems with spin spiral states.

The FP-LAPW method is based on the Augmented Plane Wave (APW) method. In the APW method and its predecessors, the unit cell is partitioned into non-overlapping atomic spheres centred around the atomic sites called muffin-tins and an interstitial region, this is called the Atomic Sphere Approximation (ASA). Then, the potential of several atoms in a crystal lattice has a form of a muffin-tin, see Fig. 3.2b. Therefore, the electron is affected by the nuclear potential inside the muffin-tin radius, r_{MT}, but between atoms, in the interstitial part, it behaves as a free electron.

On the other hand, the Full Potential (FP) method considers the nuclei potential not just inside a finite radius but also in the interstitial part, i.e. between the wells that forms the muffin-tin. Thus, the potentials are approximated smoothly as shown in Fig. 3.2a.

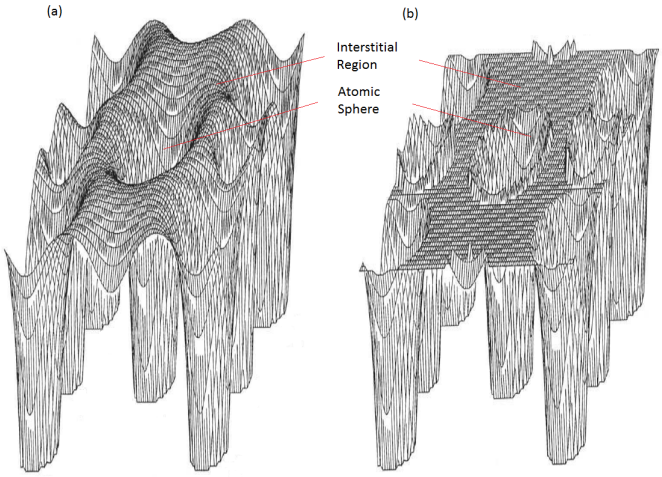

Figure 3.2: Scheme of a crystal potential. (a) Full potential; (b) Muffin-tin potential.

Hence, the APW method considers a spherical symmetry of the potential inside the muffin-tin S and a constant potential in the interstitial region I, then the wave function is expressed as [70]

$$\varphi_{\mathbf{k}}(\mathbf{r}) = \begin{cases} \Omega^{-1/2} \sum_{\mathbf{G}} c_{\mathbf{G}} e^{i(\mathbf{G}+\mathbf{k})\cdot\mathbf{r}} & \mathbf{r} \in I \\ \sum_{lm} A_{lm} u_l(r) Y_{lm}(\hat{\mathbf{r}}) & \mathbf{r} \in S \end{cases} \tag{3.36}$$

where Ω is the cell volume, $\mathbf{G}$ is a reciprocal lattice vector, $\mathbf{k}$ is the crystal momentum, $c_{\mathbf{G}}$ and A_{lm} are expansion coefficients, $Y_{lm}(\hat{\mathbf{r}})$ are the spherical harmonics and $u_l(r)$ are the radial solutions of the Schrödinger equation:

$$\left[-\frac{d^2}{dr^2} + \frac{l(l+1)}{r^2} + V(r) - E_l \right] r u_l(r) = 0 \tag{3.37}$$

where E_l is an energy parameter, $V(r)$ is the spherical component of the potential in S. The continuity is guaranteed by the expansion coefficients, they should match for each lm at the sphere boundary, this yields

$$A_{lm} = \frac{4\pi i^l}{\Omega^{1/2} u_l(r_{MT}, E_l)} \sum_{\mathbf{G}} c_{\mathbf{G}} j_l\left(|\mathbf{k}+\mathbf{G}| r_{MT}\right) Y^*_{lm}(\mathbf{k}+\mathbf{G}) \tag{3.38}$$

One of the main problems of the APW method is the huge time expended in order to find the energy eigenvalues. In order to eliminate the energy dependence of the APW basis set, a

linearisation of the solutions of the radial Schrödinger equation in the energy is done expanding $u_l(r,E)$ in Taylor series around E_l [7]:

$$u_l(r,E) = u_l(r,E_l) + (E-E_l)\dot{u}_l(r,E_l) + \mathscr{O}((E-E_l)^2) \tag{3.39}$$

where E_l is the linearisation energy and it belongs to an appropriate energy window. This is called the Linearised Augmented Plane Wave (LAPW) method.

Solving the KS equation with the LAPW method, the wave function has necessarily two representations to satisfy the boundary conditions between the interstitial I and the sphere boundary S regions as shown

$$\varphi_{\mathbf{k}}(\mathbf{r}) = \begin{cases} \Omega^{-1/2}\sum_{\mathbf{G}} c_{\mathbf{G}} e^{i(\mathbf{G}+\mathbf{k})\cdot\mathbf{r}} & \mathbf{r}\in I \\ \sum_{lm}[A_{lm}u_l(r) + B_{lm}\dot{u}_l(r)]Y_{lm}(\hat{\mathbf{r}}) & \mathbf{r}\in S \end{cases} \tag{3.40}$$

where $\dot{u}_l(r)$ are the energy derivatives of the radial functions and the coefficients A_{lm} and B_{lm} are determined using the continuity criteria of the wave function and its first derivative in the boundaries of both regions. Thus, in the interstitial region, augmented plane waves are used as the first basis set and inside the muffin-tin, radial solutions of the Schrödinger equation and radial functions form a linear combination which is used to describe the behaviour of the electron. It is important to mention that the number of basis functions in the LAPW method is higher than in the APW method [71].

The augmented plane wave plus local orbital (APW+lo) method combines the advantages of an energy independent basis set and does not require a higher plane wave cut-off than the original APW basis functions. Also, APW does not offer enough flexibility to find solutions around a fixed energy parameter E_l. Then, using a complementary basis set of local orbitals the variational freedom can be improved specially for quantum numbers $l \leq 3$. Then, these local orbital extension is defined as

$$\varphi_{\mathbf{k}}(\mathbf{r})^{lo}_{lm} = \begin{cases} 0 & \mathbf{r}\in I \\ [a^{lo}_{lm}u_l(r,E_l) + b^{lo}_{lm}\dot{u}_l(r,E_l)]Y_{lm}(\hat{\mathbf{r}}) & \mathbf{r}\in S \end{cases} \tag{3.41}$$

where the $\varphi_{\mathbf{k}}(\mathbf{r})^{lo}_{lm}$ are local because they are defined only within the muffin-tin sphere S [71].

In this way, atomic-like orbitals conform the second basis functions. Both basis sets satisfied continuity and differentiability conditions at the boundary, thus a_{lm}^{lo} and b_{lm}^{lo} can be determined. In the FP-LAPW method, the potential is defined as follows [59]:

$$V(\mathbf{r}) = \begin{cases} \sum_{\mathbf{k}} V_{\mathbf{k}} e^{i\mathbf{k}\cdot\mathbf{r}} & \mathbf{r} \in I \\ \sum_{lm} V_{lm}(r) Y_{lm}(\hat{\mathbf{r}}) & \mathbf{r} \in S \end{cases} \tag{3.42}$$

Thus, the potential $V(\mathbf{r})$ in Eq. 3.42 is expanded into lattice harmonics (inside each atomic sphere S) and as a Fourier series (in the interstitial region I) with an analogous representation for the charge density $\rho(\mathbf{r})$. Hence, $\varphi_{\mathbf{k}}$ form a basis to expand the KS orbitals as follows:

$$\phi_i = \sum_{\mathbf{k}} c_{i\mathbf{k}} \varphi_{\mathbf{k}}(\mathbf{r}) \tag{3.43}$$

where $c_{i\mathbf{k}}$ are expansion coefficients. Solving the KS equations means to determine the $c_{i\mathbf{k}}$ coefficients which minimise the total energy. Then, the coefficients of the density expansion are used in each iteration to create the Coulomb potential via the solution of the Poisson's equation and construct the exchange-correlation potential.

Consequently, the effective potential in the KS equations can be found due to the density being known, but conversely, the density can be obtained solving the KS equations which requires the knowledge of the potential. This dilemma can only be solved iteratively by the Self Consistent Field (SCF) cycle.

After self-consistency is reached, quantities like total energy, DOS, charge or spin densities, band structure, EMD, among others can be obtained.

3.5 Pseudopotential Method

In most of the atoms, core electrons can be considered fixed because they are quite strongly bound due to the nuclear attraction. Also, core electrons are almost unaffected by the motion of the valence ones. Then, the valence electrons feel a small effective potential due to the cancellation of the attractive nuclear potential and the repulsive potential of the core electrons. This effective potential is called Pseudopotential (PP) [54]. Also, a PP can include some valence

electrons and this could be useful for solving a particular problem.

There are two types of PPs: empirical and Ab-initio. Empirical PPs are designed to fit atomic or solid state experimental data. In contrast, Ab-initio PPs are generated from theoretical calculations trying to fit the valence properties of the atom.

To understand the formalism behind the PP method is important to know its predecessor: the Orthogonal Plane Wave (OPW) method. OPW considers an electron as nearly free in the interstitial region. On the other hand, in the core region the wave function must oscillate rapidly because the kinetic energy is higher than in the interstitial region. Trying to reproduce a high number nodes with planes waves is computationally too expensive. Then, a linear combination of Bloch functions constructed from atomic orbitals is used to represent the wave function in the core region. Also, core states could be assumed the same for molecules or solids as in the atom. Now, to describe the valence states an orthogonalised plane wave is defined as the sum of a plane wave and a linear combination of Bloch wave functions, the coefficients of the linear combination are determined so that the OPW is orthogonal to each core electron. Only few OPW functions are necessary to get the energy eigenvalues of a solid [72].

Phillips and Kleinman (PK) used OPW functions to solve the Schrödinger equation for the valence states [73]

$$\hat{H}\psi_i^v(\mathbf{r}) = \left[-\frac{1}{2}\nabla^2 + V(\mathbf{r})\right]\psi_i^v(\mathbf{r}) = \varepsilon_i^v\psi_i^v(\mathbf{r}) \tag{3.44}$$

where the V is the total effective potential. Then, the pseudostates are defined by

$$\tilde{\psi}_i^v(\mathbf{r}) = \psi_i^v(\mathbf{r}) + \sum_j a_j^{vc}\psi_j^c(\mathbf{r}) \tag{3.45}$$

where $a_j^{vc} = <\psi_j^c|\tilde{\psi}_i^v>$. Applying $\hat{H}$ to $\tilde{\psi}_i^v(\mathbf{r})$ gives the following expression

$$\hat{H}^{\mathrm{PK}}\tilde{\psi}_i^v(\mathbf{r}) \equiv \left[-\frac{1}{2}\nabla^2 + \hat{V}^{\mathrm{PK}}\right]\tilde{\psi}_i^v(\mathbf{r}) = \varepsilon_i^v\tilde{\psi}_i^v(\mathbf{r}) \tag{3.46}$$

where the PP $\hat{V}^{\mathrm{PK}} = V + \hat{V}^{\mathrm{R}}$. $\hat{V}^{\mathrm{R}}$ is a non-local operator acting on $\tilde{\psi}_i^v(\mathbf{r})$ in the following way:

$$\hat{V}^R\tilde{\psi}_i^v(\mathbf{r}) = \sum_j \left(\varepsilon_i^v - \varepsilon_j^c\right)\left\langle\psi_j^c|\tilde{\psi}_i^v\right\rangle\psi_j^c(\mathbf{r}) \tag{3.47}$$

$\hat{V}^{\mathrm{R}}$ is repulsive due to $\left(\varepsilon_i^v - \varepsilon_j^c\right)$ is always positive. Therefore, $\hat{V}^{\mathrm{PK}}$ is weaker than the total effective potential V. Also, $\hat{V}^{\mathrm{PK}}$ is a semilocal potential because V is a local potential and $\hat{V}^{\mathrm{R}}$ is non-local. It is important to mention that the contribution of $\hat{V}^{\mathrm{R}}$ outside the core region is negligible, then $\hat{V}^{\mathrm{PK}} = V$ in the interstitial region. Furthermore, the pseudostates $\tilde{\psi}_i^v(\mathbf{r})$ are not orthonormal because the complete function $\psi_i^v(\mathbf{r})$ also contains the sum over core orbitals.

Ab-initio PP can be created in three steps. First, atomic levels and orbitals are generated from DFT calculations. Second, the PP is generated from atomic results. Third, a validation of the PP is done. If not, the previous step must be done differently.

The first step is done considering a spherically symmetric self-consistent Hamiltonian. The atomic state is defined by the electronic state given by the principal quantum number and the angular momentum. Then, a radial Schrödinger equation is solved to get the one-electron states. The second step could be done in several ways hence since PK the PP theory has evolved considerably. Nowadays, there are three main PP methods: Norm-Conserving (NC), Ultrasoft (US) and PAW sets. In all of them, the most important part is the generation of 'pseudo-orbitals' from atomic AE orbitals. Finally, the third step is designed to check the accuracy and the computational cost of the selected method. In the following paragraphs, NC PP, US PP methods will be discussed because they were used in the present work.

In a NC PP, the pseudostates $\tilde{\psi}(\mathbf{r})$ are normalised and are solutions of a model potential chosen to reproduce the valence properties of an AE calculation. Outside a some core radius r_c the pseudo wave functions (and potential) are constructed to be equal to the AE valence wave functions. Whereas inside r_c the pseudo wave functions differ from the AE wave functions, but the norm is constrained to be the same:

$$\int_0^{r_c} \mathrm{d}r r^2 \tilde{\psi}^*(r)\tilde{\psi}(r) = \int_0^{r_c} \mathrm{d}r r^2 \psi^*(r)\psi(r) \tag{3.48}$$

The imposition of NC ensures not only that the logarithmic derivative of the pseudo and AE wave function match at the reference energy E, but also that the first derivative with respect to E matches as well. Furthermore, the PP is dependent of the angular momenta l because the wave function and eigenvalue are different for different l. This kind of PPs are called semi-local.

The NC PP is transferable, that is the same PP used in atomic calculations can be used for molecules and solid state calculations. Also, NC PP is soft as possible, meaning that it should

allow expansion of $\tilde{\psi}_i^v(\mathbf{r})$ using as few plane waves as possible. Hence, plane waves are expanded in Fourier components, the 'hardness' of a PP is associated with the number of components needed to describe the valence properties to a given accuracy. Furthermore, the pseudo charge density should reproduce the valence charge density as accurately as possible.

Troullier and Martins (TM) invented a method for constructing NC PPs which uses analytic functions to represent $\tilde{\psi}(\mathbf{r})$ inside r_c [74]. Then, atomic orbitals in the core region are replaced with smooth nodeless pseudo orbitals. The TM is a robust method which uses an exponential of a polynomial as pseudo orbitals [75].

On the other hand, Vanderbilt proposed pseudo wave functions $\tilde{\psi}$ which are equal to AE wave functions outside r_c, as NC PPs, but inside r_c they are allowed to be as soft as possible [76]. For this, the NC condition is removed but some problems could appear because of this, such as: a non-trivial overlap into the secular equation, the pseudo charge density does not correspond to $\sum \tilde{\psi}^* \tilde{\psi}$ and the PPs become less transferable [70].

In the formulation of Vanderbilt, the total energy is written as

$$E = \sum_{occ} \langle \tilde{\psi}_j | T + V^{NL} | \tilde{\psi}_j \rangle + \int d^3\mathbf{r} V^L(\mathbf{r}) \rho(\mathbf{r}) + \frac{1}{2} \int d^3\mathbf{r} d^3\mathbf{r}' \frac{\rho(\mathbf{r}) \rho(\mathbf{r}')}{|\mathbf{r} - \mathbf{r}'|} + E_{xc}[\rho] + E_{II} \tag{3.49}$$

where T is the kinetic energy, V^L is the local component of the PP and V^{NL} is the non-local separable 'ultrasoft' PP defined by

$$V^{NL} = \sum_{mn} D_{nm}^{(0)} |\beta_n\rangle \langle \beta_m| \tag{3.50}$$

where $D_{nm}^{(0)}$ are coefficients and β_n are local functions which come from

$$|\beta_n\rangle = \sum_m \left(B^{-1}\right)_{mn} |\chi_m\rangle \tag{3.51}$$

where $B_{mn} = \langle \tilde{\psi}_n | \chi_m \rangle$ and χ_m is a local wave function which vanishes beyond r_c where $V^{AE} = V^L$ and $\tilde{\psi}_j(\mathbf{r}) = \psi_j(\mathbf{r})$. The difference in the norm between an AE wave function and a pseudo wave function is

$$Q_{nm}(\mathbf{r}) = \psi_n^*(\mathbf{r}) \psi_m(\mathbf{r}) - \tilde{\psi}_n^*(\mathbf{r}) \tilde{\psi}_m(\mathbf{r}) \tag{3.52}$$

Then, the unscreened or bare ion matrix $D_{nm}^{(0)}$ can be obtained by

$$D_{nm}^{(0)} = B_{nm} - \int d^3 r V_{ion}^{L}(\mathbf{r}) Q_{nm}(\mathbf{r}) \tag{3.53}$$

where V_{ion}^{L} is the local bare ion PP, that is $V_{ion}^{L} = V^{L} - V^{Hartree} - V^{xc}$. Thus, the secular equation could be solved by iterative methods and this is defined as

$$\left(T + V^{\mathrm{L}} + V^{\mathrm{NL}} - \varepsilon_j S\right) |\tilde{\psi}_j\rangle = 0 \tag{3.54}$$

where S is the non-local overlap operator with the integral defined inside r_c as follows

$$S = \mathbf{1} + \sum_{nm} \int d^3\mathbf{r} Q_{nm}(\mathbf{r}) |\beta_n\rangle\langle\beta_m| \tag{3.55}$$

The full density could be constructed using Eq. 3.52 which represents an augmentation inside r_c in the following way:

$$\rho(\mathbf{r}) = \sum_{occ} \left[\tilde{\psi}_j^*(\mathbf{r}) \tilde{\psi}_j(\mathbf{r}) + \sum_{mn} Q_{nm}(\mathbf{r}) < \tilde{\psi}_j |\beta_n >< \beta_m| \tilde{\psi}_j > \right] \tag{3.56}$$

the augmentation term changes along with the wave functions during the self-consistent cycle. Then, the PP also evolves during the calculation hence the augmentation term also contributes to it. Thus, it is feasible to use large values of r_c in the US PP generation. This means that is possible to get very soft PPs, without sacrificing the accuracy of the calculation.

Quantum Espresso is a integrated suite of computer codes designed for electronic structure calculations based on DFT. In its package PWscf, the KS orbitals are expanded over a finite plane wave basis set. Also, the interaction ion-electron can be represented by NC PPs, US PPs and APW sets. PWscf can use LDA and GGA exchange-correlation functionals. Also, it is able to work with spin polarisation and non-collinear magnetism. The structural optimisation is performed using the Broyden-Fletcher-Goldfarb-Shanno (BFGS) algorithm [77] or damped dynamics. Microscopic degrees of freedom (i.e. the atomic coordinates) and/or the macroscopic ones (shape and size of the unit cell) can be involved in the structural optimisation process [78]. The next couple of sections deal with different approaches for describing the compositional disorder in alloys.

3.6 Special Quasirandom Structure

A SQS is a special periodic supercell with a finite number N of lattice sites which mimics the correlation functions of an infinite substitutional random alloy [79]. Modelling random alloys with these periodic structures only introduces errors beyond a certain distance, hence interactions between distant neighbours contribute less to the total energy than those from close neighbours. This makes SQS an attractive method to represent the atomic configuration of a random alloy [80]. It is possible to reproduce a SQS preserving the overall concentration and nearest-neighbour correlation functions of a random alloy.

Alloy Theoretic Automated Toolkit (ATAT) is a code used to generate the SQS. First, as initial parameter a random supercell configuration σ^{rnd} is needed. Also, the number of components of the alloy M_i and their molar fraction, and also the crystal group of the alloy should be defined.

Then, a cluster file is generated through the command *corrdump* where the range of pairs, triplets, etc. is entered. A cluster is a list of lattice sites considered in the calculation of a particular correlation function [81].

Next, the routine *mcsqs* performs a search of the best SQS. Also, the total number of atoms N for the required SQS must be chosen in this step. *mcsqs* is a Monte Carlo algorithm which minimises the following objective function [82]:

$$Q = -\omega L + \sum_{\alpha \in \mathbb{A}} |\Delta\rho_\alpha(\sigma)| \tag{3.57}$$

where $\mathbb{A}$ is a user-specified set of clusters, ω is a user-specified weight, L is the largest l such that $\Delta\rho_\alpha(\sigma) = 0$ for all clusters α with $diam(\alpha) \leq l$ where $diam(\alpha)$ is the length of the largest pair contained in the cluster α. The second term in Eq. 3.57 is a sum of the difference between the randomness of a candidate SQS and the true random configuration given by

$$\Delta\rho_\alpha(\sigma) = \rho_\alpha(\sigma) - \rho_\alpha(\sigma^{rnd}) \tag{3.58}$$

where $\rho_\alpha(\sigma^{rnd})$ and $\rho_\alpha(\sigma)$ are the correlations of the fully disordered state and a candidate SQS respectively. Then, $\rho_\alpha(\sigma)$ is the correlation associated with a cluster α and it is defined as:

$$\rho_\alpha(\sigma) \equiv \langle \Gamma_{\alpha'}(\sigma) \rangle_\alpha \tag{3.59}$$

where the average $\langle \ldots \rangle_\alpha$ is taken over all the clusters α' equivalent by symmetry to cluster α. A configuration σ is represented as a vector specifying the number of chemical species that can occupy the lattice site i. In an alloy where site i can host M_i distinct chemical species, as a result σ_i takes values from 0 to $M_i - 1$. $\Gamma_\alpha(\sigma)$ is a cluster function defined as:

$$\Gamma_\alpha(\sigma) = \prod_i \gamma_{\alpha_i, M_i}(\sigma_i) \tag{3.60}$$

where α_i is a numerical index, ranging from 0 to $M_i - 1$, which represents the compositional degree of freedom considered in the cluster. If site i does not belong to the cluster, then $\alpha_i = 0$. Also, the cluster function satisfies $\gamma_{0,M_i}(\sigma_i)$=1 and the following orthogonality condition:

$$\frac{1}{M_i} \sum_{\sigma_i=0}^{M_i-1} \gamma_{\alpha_i, M_i}(\sigma_i)\, \gamma_{\beta_i, M_i}(\sigma_i) = \begin{cases} 1 & if \quad \alpha_i = \beta_i \\ 0 & otherwise \end{cases} \tag{3.61}$$

Finally, for a multicomponent system ATAT uses the following choice for $\gamma_{\alpha_i, M_i}(\sigma_i)$ [82]:

$$\gamma_{\alpha_i, M_i}(\sigma_i) = \begin{cases} 1 & if \quad \alpha_i = 0 \\ -\cos\left(2\pi \left[\frac{\alpha_i}{2}\right] \frac{\sigma_i}{M}\right) & if \quad \alpha_i > 0 \quad and \quad \text{odd} \\ -\sin\left(2\pi \left[\frac{\alpha_i}{2}\right] \frac{\sigma_i}{M}\right) & if \quad \alpha_i > 0 \quad and \quad \text{even} \end{cases} \tag{3.62}$$

where [...] denotes the 'round up' operation, α_i and σ_i can range from 0 to $M_i - 1$ as previously stated.

The configuration σ which gives the minimum value of the Eq. 3.57 is selected as the best SQS. Then, the SQS lattice parameter is scaled to its experimental value of the alloy. In this way, the coordinates of each atom in the SQS could be used as part of the input file of Elk or Quantum Espresso.

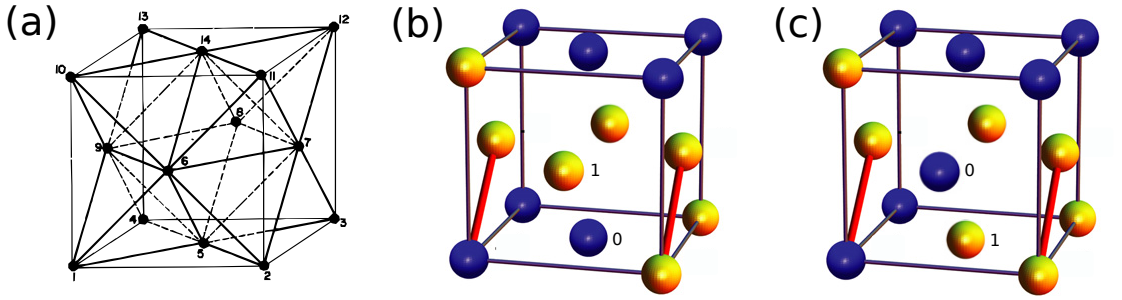

Figure 3.3: FCC cell of a binary alloy $A_{0.5}B_{0.5}$ with A atoms (yellow) and B atoms (blue). (a) FCC structure F$m3m$; (b) Initial configuration σ^{rnd}; (c) New configuration σ. The red lines correspond to the shortest nearest neighbours distance between pairs of atoms [8].

The generation of a SQS of 14 atoms for a FCC binary alloy $A_{0.5}B_{0.5}$ is described in the following paragraphs as an example. First, a FCC cell with atoms placed in random positions is created (see Fig. 3.3b.). The numeration shown in Fig. 3.3a. is used to identify the lattice sites of the cell. Following the notation above, for a binary alloy $M_i = 2$ and so σ_i can take values of 1 or 0 for the atoms A and B respectively. Then, each possible factor of Eq. 3.60 is defined according to Eq. 3.62 as follows: $\gamma_{0,2}(0) = +1$, $\gamma_{0,2}(1) = +1$, $\gamma_{1,2}(0) = -1$ and $\gamma_{1,2}(1) = +1$.

Next, taking the site 1 in Fig. 3.3a. as the origin is possible to define all the pairs of neighbours relative to this site. These are: (1,5), (1,2), (1,7), (1,3) and (1,12) with a multiplicity of 3, 3, 3, 3 and 1 respectively. These pairs of atoms are ordered according their distance from the origin. ATAT allows to chose the range or cut-off length L for pairs, triplets, quadruplets, etc.. For this example, the first neighbours distance equal to $\frac{\sqrt{2}L}{2}$ is taken where L is the lattice parameter. Thus, only the pairs with a distance between atoms like (1,5) (red lines in Fig. 3.3) are selected as elements of the set $\mathbb{A}$ in Eq. 3.57.

The initial configuration vector σ^{rnd} corresponds to:

$$\sigma^{rnd} = (0,1,1,0,0,1,1,1,1,1,0,0,0,0)$$

Then, the cluster function for the pair (1,5) is given by:

$$\Gamma_{(1,5)}(\sigma^{rnd}) = \gamma_{1,2}(\sigma_1) \times \gamma_{1,2}(\sigma_5) = \gamma_{1,2}(0) \times \gamma_{1,2}(0) = (-1) \times (-1) = 1$$

Note that the pair (1,5) corresponds to a pair of atoms BB. There are 36 pairs in total with the same range in Fig. 3.3b. However, 10 are AA, 5 are BB and 21 are AB. Thus, the correlations

associated with the set of pairs equivalent to *AA*, *BB* and *AB* are calculated as follows:

$$\rho_{AA}(\sigma^{rnd}) = \left\langle \Gamma_{\{(2,7),\ldots\}}(\sigma^{rnd}) \right\rangle_{AA} = \frac{1}{10}\left(\sum_{i=1}^{10} 1\right) = 1$$

$$\rho_{BB}(\sigma^{rnd}) = \left\langle \Gamma_{\{(1,5),\ldots\}}(\sigma^{rnd}) \right\rangle_{BB} = \frac{1}{5}\left(\sum_{i=1}^{5} 1\right) = 1$$

$$\rho_{AB}(\sigma^{rnd}) = \left\langle \Gamma_{\{(1,6),\ldots\}}(\sigma^{rnd}) \right\rangle_{AB} = \frac{1}{21}\left(\sum_{i=1}^{21} (-1)\right) = -1$$

Next, the atoms of the sites 5 and 6 of Fig. 3.3b. are swapped. This movement is called a Monte Carlo step. Then, the new configuration vector σ of Fig. 3.3c. is given by:

$$\sigma = (0,1,1,0,1,0,1,1,1,1,0,0,0,0)$$

Following the same procedure and constrains used for σ^{rnd}, one can obtain the correlation associated to the pairs of atoms *AA*, *BB* and *AB* for the new configuration. Thus, the new configuration has 11 pairs *AA*, 6 pairs *BB* and 19 pairs *AB* with correlations values of $\rho_{AA}(\sigma) = 1$, $\rho_{BB}(\sigma) = 1$ and $\rho_{AB}(\sigma) = -1$ respectively.

After that, assuming $w = 1$ and $L = 1$ in Eq. 3.57 is possible to calculate the objective function for the candidate SQS as bellow:

$$Q = -1 \times \frac{\sqrt{2}}{2} + |\Delta\rho_{AA}(\sigma)| + |\Delta\rho_{BB}(\sigma)| + |\Delta\rho_{AB}(\sigma)| \tag{3.63}$$

$$Q = -1 \times \frac{\sqrt{2}}{2} + |1-1| + |1-1| + |-1+1| = -\frac{\sqrt{2}}{2} \tag{3.64}$$

Finally, ATAT uses the Metropolis algorithm to decide if the new configuration is accepted or not [81]. For this, a random number $p_0 \in [0,1]$ is generated. Then, if $p_0 < \min(1, exp(-Q/T))$ the swap is accepted, otherwise do not.

Several atomic swaps are done until find one configuration with the minimum value of Q and so the best SQS is found.

3.7 Koringa-Kohn-Rostoker Method

The KKR method is based in multiple scattering theory. A muffin-tin potential is placed around each atom site, thus the electron, represented by the free propagator, travels between atom sites and it gets scattered due to the spherical potentials. Thereby, all this problem can be formulated in terms of Green's functions.

According to the multiple scattering theory the Green's function $G(\varepsilon, \mathbf{r}, \mathbf{r}')$ describes the propagation of a particle from point $\mathbf{r}$ to $\mathbf{r}'$ at energy ε. The Green's function is defined by

$$G(\varepsilon) = (\varepsilon - H)^{-1} \tag{3.65}$$

where H is the Hamiltonian of the system. Therefore, the Schrödinger equation can be expressed as

$$\left[\frac{\hbar^2}{2m_e}\nabla^2 + \varepsilon\right] G\left(\varepsilon, \mathbf{r}, \mathbf{r}'\right) = \delta\left(\mathbf{r} - \mathbf{r}'\right) \tag{3.66}$$

From perturbation theory is possible to express the Green's function G in power series of the free particle propagator G_0 and scattering matrix elements t as follows

$$\begin{aligned} G &= G_0 + G_0 t G_0 + G_0 t G_0 t G_0 + \cdots \\ G &= G_0 + G_0 t G \end{aligned} \tag{3.67}$$

Now, one can define the full multiple scattering matrix T or t-matrix for the whole system as

$$\begin{aligned} T &= t + t G_0 t + t G_0 t G_0 t + \cdots \\ T &= t + t G_0 T \\ T &= (t^{-1} - G_0)^{-1} \end{aligned} \tag{3.68}$$

where each term in the series represents one of the possible scattering processes. Thus, it is possible to express G as

$$G = G_0 + G_0 T G_0 \tag{3.69}$$

which means that is enough to know T to determine G. Also, finding the zeros of the determinant:

$$det(t^{-1} - G_0) = 0 \tag{3.70}$$

is possible to obtain the eigenfunctions of the system as function of ε. In multiple scattering by muffin-tin potentials G_0 depends only on the crystalline structure and ε, and t represents the effects of the potential inside each atomic sphere. One great advantage of this method is that the spectral representation of the Green's functions and other physical properties of the system are calculated as integrals over the energy.

The CPA is useful for modelling random alloys when is combined with Green's function based methods, for instance: KKR, Exact Muffin-Tin Orbitals (EMTO) and Linear Muffin-Tin Orbital (LMTO). CPA is an effective medium theory where an average of the scattering amplitude is done in each site. Therefore, the electron is propagating through this effective medium represented by the coherent potential.

The t-matrix can be expressed by the scattering path operator τ^{nm} as follows [83]:

$$T = \sum_{n,m} \tau^{nm} \tag{3.71}$$

Then, the CPA condition defines the path operator for a binary alloy as

$$x_{\mathrm{A}} \underline{\tau}_{\mathrm{A}}^{nn} + x_{\mathrm{B}} \underline{\tau}_{\mathrm{B}}^{nn} = \underline{\tau}_{\mathrm{CPA}}^{nn} \tag{3.72}$$

where the matrices $\underline{\tau}$ are projected scattering path operators and the relative concentrations of the elements A and B are x_{A} and x_{B} respectively. Therefore, the scattering properties $\underline{\tau}_{\alpha}^{nn}$ of an α atom embedded in the CPA medium, in other words a substitutional impurity is given by

$$\underline{\tau}_{\alpha}^{nn} = \underline{\tau}_{\mathrm{CPA}}^{nn} \left[1 + \left(\underline{t}_{\alpha}^{-1} - \underline{t}_{\mathrm{CPA}}^{-1} \right) \underline{\tau}_{\mathrm{CPA}}^{nn} \right]^{-1} \tag{3.73}$$

where $\underline{t}_{\alpha}$ and $\underline{t}_{CPA}$ are the single site t-matrices of the element α and the CPA medium respectively.

In the present work, KKR-CPA calculations in the ASA mode with the Vosko, Wilk and Nusair (VWN) exchange-correlation functional [84] of HEAs were done by Prof. S. B. Dugdale with

the SPR-KKR package.

3.8 Electron Momentum Densities

In this section, only the theoretical details related with the determination of the EMD by Ab-initio methods are described and the experimental ones will be discussed in the following chapter.

The electronic structure of a material can be investigated from the EMD [85]. The EMD is defined as

$$\rho(\mathbf{p}) = \sum_{\sigma,\mathbf{k},j} n_{\sigma,\mathbf{k},j} \left| \int \psi_{\sigma,\mathbf{k},j}(\mathbf{r}) \mathrm{e}^{-\mathrm{i}\mathbf{p}\cdot\mathbf{r}} \mathrm{d}\mathbf{r} \right|^2 \tag{3.74}$$

where $\psi_{\sigma,\mathbf{k},j}(\mathbf{r})$ is the electronic wave function with wave vector $\mathbf{k}$ in the band j and with spin polarisation σ and $n_{\sigma,\mathbf{k},j}$ is its occupation number density.

In the literature of this field of study [9, 86, 87] a 'projection' means an integration of the EMD along one determined spatial direction. Thus, it is possible to get a once-projected EMD or a bi-dimensional EMD which can be experimentally probed by the Two-Dimensional Angular Correlation of Annihilation Radiation (2D-ACAR) technique [88]. Also, one can integrate twice the EMD and obtain the so-called CP as follows

$$J(p_z) = \iint \rho(\mathbf{p}) \mathrm{d}p_x \mathrm{d}p_y \tag{3.75}$$

The CP can be measured experimentally with inelastic X-ray scattering in the high energy transfer regime. This kind of X-ray experiments are known as Compton scattering. Then, the calculated CP is normalised and convoluted with the experimental resolution for its analysis.

Considering separately each spin polarisation σ, spin-up and spin-down, in the Eq. 3.74 one can obtain their contributions to the EMD $\rho_\uparrow(\mathbf{p})$ and $\rho_\downarrow(\mathbf{p})$ respectively. Hence, the EMD is equal to $\rho(\mathbf{p}) = \rho_\uparrow(\mathbf{p}) + \rho_\downarrow(\mathbf{p})$. Then, the MCP can be defined as

$$J_{mag}(p_z) = \iint \rho_{mag}(\mathbf{p}) dp_x dp_y \tag{3.76}$$

where $\rho_{mag}(\mathbf{p}) = \rho_\uparrow(\mathbf{p}) - \rho_\downarrow(\mathbf{p})$ is the so called MDME [89, 90]. MCP can be measured by Magnetic Compton scattering [11]. Magnetic Compton scattering allows the characterisation

of magnetic properties over diverse materials [91]. In the present work, MCPs were calculated using the Elk code in the framework of the DFT. In addition, MCPs with KKR-CPA method were done by Prof. S.B. Dugdale for comparison reasons.

Elk code writes the EMD according to the Eq. 3.74 with the difference that now the Fourier transform is applied over the KS orbital $\psi_{\sigma,\mathbf{k},j}(\mathbf{r})$ with wave vector $\mathbf{k}$ in the band j and with spin polarisation σ. Then, one gets the following expression:

$$\rho(\mathbf{p}) = \sum_{\sigma,\mathbf{k},j} n_{\sigma,\mathbf{k},j} \left|\chi_{\sigma,\mathbf{k},j}(\mathbf{p})\right|^2 \tag{3.77}$$

where $\chi_{\sigma,\mathbf{k},j}(\mathbf{p})$ is the KS orbital in the momentum space. Thus, the EMD is obtained summing over all the $\mathbf{G}+\mathbf{k}$ vectors up to an adequate maximum length. However, summing separately each spin polarisation is possible to get $\rho_\sigma(\mathbf{p})$. In this way, one can obtain the CP or the MCP according to the needs. The projection of the EMD is done using the trapezoidal method [92].

On the other hand, SPR-KKR represents the electronic structure in terms of the electronic Green's function $G(\varepsilon,\mathbf{r},\mathbf{r}')$ instead of Bloch wave functions and eigenvalues. The Green's function in the momentum space is given by [93]

$$G_{\sigma\sigma'}\left(\varepsilon,\mathbf{p},\mathbf{p}'\right) = \frac{1}{N\Omega}\int d^3r \int d^3r' \Phi^*_{\mathbf{p}\sigma}(\mathbf{r}) \mathrm{Im}\, G^+\left(\varepsilon,\mathbf{r},\mathbf{r}'\right) \Phi_{\mathbf{p}'\sigma'}\left(\mathbf{r}'\right) \tag{3.78}$$

where σ is the spin polarisation, Ω is the volume of the unit cell, N is the number of electrons in the unit cell and $\Phi_{\mathbf{p}\sigma}$ are the eigenfunctions of the momentum operator. Then, the spin polarised momentum density $\rho_\sigma(\mathbf{p})$ in terms of the Green's function in momentum space is written as

$$\rho_\sigma(\mathbf{p}) = -\frac{1}{\pi}\int_0^{E_F} \mathrm{Im}\, G_\sigma\left(\varepsilon,\mathbf{p},\mathbf{p}\right) d\varepsilon \tag{3.79}$$

where E_F is the Fermi energy. Thus, the MCP could be calculated like in Eq. 3.76.

Chapter 4

Experimental Methods

In the previous chapter, the EMD was introduced as one of the key quantities to understand the electronic structure of HEAs. Interpreting the data from EMD and MDME is not trivial. To achieve this, the present chapter contains a review of the theory and experimental foundation of Compton scattering which goes back to times of A. Compton. The Compton effect was the first theory of the scattering of X-rays [94] and it was an important landmark in the consolidation of Quantum Mechanics at the begging of the XX century.

A few years later, P.A.M. Dirac combined the other revolutionary theory of the last century, the Special Relativity of A. Einstein, with Quantum Mechanics and got a relativistic description of the electron [95, 96]. However, his theory was not well received by the scientific community because a new particle, the positron with the same mass as the electron but opposite charge, emerged from his equation [97].

At that time, discovering antimatter was not in the plans of most of the experimental physicists. However, a most accessible way to confirm the theory of Dirac could be done using the Compton effect. Actually, O. Klein and Y. Nishina calculated the Compton scattering cross section from the relativistic theory of the electron of Dirac with that intention [98, 97].

J. W. DuMond was one of the first scientist in applying Compton scattering as an experimental physics tool. By 1929, he found the first experimental evidence of the Fermi-Dirac distribution function of the electron gas [99]. Also, DuMond and his colleagues measured the first CPs in light elements like H, He and Be [9].

After 30 years, M. J. Cooper revived the interest in Compton scattering trying to observe the correlations of the electron gas in Na [9]. Through this technique, it is possible to obtain the momentum electron density which offers a more intuitive way to study the bonds and orbitals in a huge variety of compounds. Also, in 1978 W. Schülke did the first Fermi surface reconstruction on Li [100] from CPs expanding the possible applications of Compton scattering.

On the other hand, in 1970 P. M. Platzman and N. Tzoar proposed magnetic Compton scattering as a probe to measure the MDME [101]. By 1976, N. Sakai and K. Ono were the first ones in measuring a MCP experimenting with Fe [102]. Nowadays, the technological advances like third generation synchrotrons make possible to get high resolutions and counting rates in charge and magnetic Compton scattering experiments. Thus, this technique has become an important method of characterisation of advanced materials [103].

4.1 Compton Scattering

Compton effect is the scattering of X-rays or γ-rays by electrons. This is named in honour of its discoverer Arthur Compton [94, 104, 105]. Fig. 4.1 shows an incident beam hitting a stationary electron after which the light is scattered with an angle Θ and the electron suffers a recoil. Applying the principles of conservation of momentum and conservation of energy, the decrease in the photon energy is:

$$\lambda_f - \lambda_i = \frac{h}{mc}(1 - cos\Theta)$$

$$\Delta\lambda = \frac{h}{mc}(1 - cos\Theta) \tag{4.1}$$

where λ_f is the wavelength of the photon scattered at angle Θ, λ_i is the wavelength of the incident photon, m is the mass of the electron and c is the speed of light. However, no information about the target nature is included in Eq. 4.1.

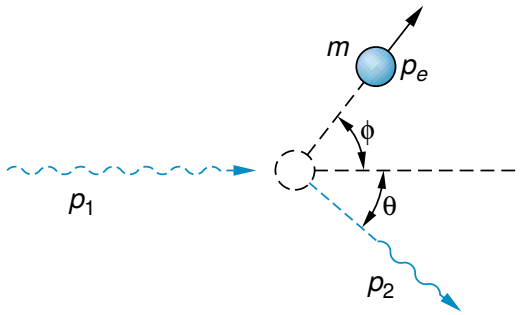

Figure 4.1: The Compton effect is the scattering of X-rays and it is analysed as a collision between a photon with initial momentum $\mathbf{p}_1$ and a steady electron with mass m. After the collision the photon is scattered in an angle θ and a momentum $\mathbf{p}_2$ and the electron is scattered in an angle ϕ and a momentum $\mathbf{p}_e$.

A different scenario occurs when the photon is scattered by electrons of atoms or molecules. DuMond and Jauncey supposed that the collision between the photon and the electron in an atom must be impulsive, meaning that they interact briefly [9]. Thus, the other electrons can not relax to take the hole left by the recoiling electron. Therefore, the potential seen by the target electron remains invariable before and immediately after the collision. Then, the target electron is moving but unbound as shown in Fig. 4.2. This supposition can be fulfilled if the energy of the beam is much higher than the electron binding energy and it is called the Impulse Approximation (IA).

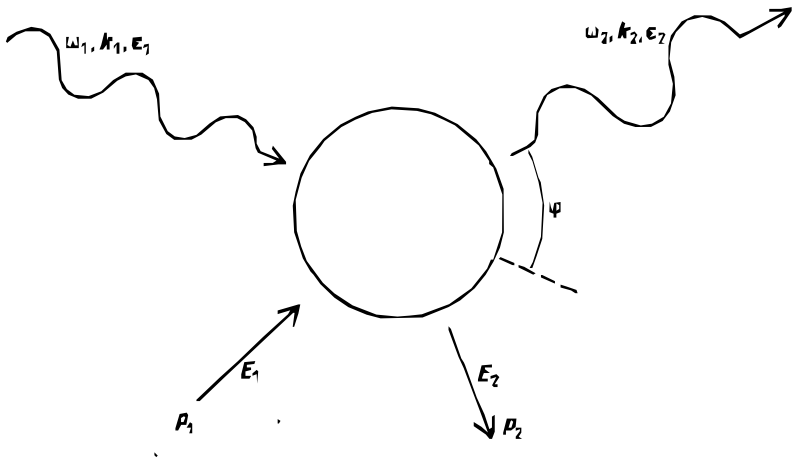

Figure 4.2: Schematic diagram of the Compton scattering interaction between an incoming photon with wavevector $\mathbf{k}_1$, energy ω_1 and unit polarisation vector ε_1 and a moving electron with momentum $\mathbf{p}_1$ and energy E_1. After the collision the photon is scattered at angle φ with wavevector $\mathbf{k}_2$, energy ω_2 and unit polarisation vector ε_2 and the electron have a resultant momentum $\mathbf{p}_2$ and energy E_2 [9]. ω is the energy when atomic units are adopted that is $e = \hbar = m = 1$ and c=137.

Then, the conservation equation can be written in the following way:

$$E_1 - E_2 = \frac{1}{2m}\left[\mathbf{p} + \hbar\left(\mathbf{k}_1 - \mathbf{k}_2\right)\right]^2 - \frac{\mathbf{p}^2}{2m}$$

$$E_1 - E_2 = \frac{\hbar^2 |\mathbf{q}|^2}{2m} + \frac{\hbar \mathbf{q}\cdot\mathbf{p}}{m} \tag{4.2}$$

where $\mathbf{q} = \mathbf{k}_1 - \mathbf{k}_2$ is the scattering vector. By 1925, Jauncey had this great idea to relate de Doppler broadening, $\Delta E = E_1 - E_2$, of the Compton scattered beam to the motion of target electrons through of the scattering vector.

In 1928, Klein and Nishina formulated a quantum mechanical treatment of Compton scattering [98] trying to confirm the validity of Dirac theory. Then, they did a semi-classical approach of the Compton scattering cross-section using the Dirac equation. Thus, the Klein-Nishina cross-section for a free, stationary electron without taking account the polarisation of the photon and the electron can be written as [106]

$$\frac{\mathrm{d}\sigma}{\mathrm{d}\Omega_{\mathbf{KN}}} = \frac{r_e^2}{2}\left(\frac{\omega_2}{\omega_1}\right)^2\left[\left(1+\cos^2\phi\right) + \frac{\hbar\left(\omega_1 - \omega_2\right)}{mc^2}\left(1-\cos\phi\right)\right] \tag{4.3}$$

where $r_e = e^2/mc^2$ is the classical electron radius, $\hbar\omega_1$ and $\hbar\omega_2$ are the incident and scattered photon energies respectively, and ϕ is the scattering angle.

After that, the cross section of Compton scattering has been derived by several scientists, the differences between approximations depends on the amount of energy of the incident photon. For the sake of simplicity, a non-relativistic approach is going to be used in the present work.

An inelastic X-ray or Compton scattering experiment uses a collimated beam of monochromatic photons, taking a certain infinitesimal solid angle element $d\Omega$ of the scattered beam and analysing its energy dependence with respect to a resolution $d\omega_2$. Thus, neglecting all resonance phenomena, the non-relativistic Double Differential Scattering Cross Section (DDSCS) for inelastic X-ray derived from the first order perturbation or weak coupling limit (Born Approximation) is composed of two factors [9]:

$$\frac{d^2\sigma}{d\Omega d\omega_2} = \left(\frac{d\sigma}{d\Omega}\right)_{\text{Th}} S(\mathbf{q},\omega) \tag{4.4}$$

where $S(\mathbf{q},\omega)$ is the dynamic structure factor and $(d\sigma/d\Omega)_{\text{Th}}$ is the Thompson scattering cross section which corresponds to the elastic scattering of photons. The Thomson term is valid only for low energies, hence for high energies the Eq. 4.3 must be used instead.

Now, using the Fermi golden rule is possible to get the probability amplitude of an electron passing from an initial state i to a final state f after being hit by the photon beam. Then, the probability amplitude is going to be proportional the inelastic term $S(\mathbf{q},\omega)$ of the DDSCS. Assuming that the initial and final states of the electron can be represented by plane waves due to IA, Eq. 4.4 transforms into [85]

$$\frac{d^2\sigma}{d\Omega d\omega_2} = \left(\frac{d\sigma}{d\Omega}\right)_{\text{Th}} \sum_{\mathbf{p}_f} \left|\langle I|e^{i\mathbf{q}\cdot\mathbf{r}}|\mathbf{p}_f\rangle\right|^2 \times \delta\left[\mathscr{E}\left(\mathbf{p}_f\right) - \mathscr{E}\left(\mathbf{p}_f - \hbar\mathbf{q}\right) - \hbar\omega\right] \tag{4.5}$$

where $\mathscr{E}$ is the kinetic energy as a function of the moment. Replacing Eq. 4.2 inside the δ-function and by defining $\mathbf{p} \equiv \mathbf{p_f} - \hbar\mathbf{q}$ to change the sum over final states $\mathbf{p_f}$ to a $\mathbf{p}$ integration, one gets:

$$\frac{d^2\sigma}{d\Omega d\omega_2} = \left(\frac{1}{2\pi\hbar}\right)^3 \left(\frac{d\sigma}{d\Omega}\right)_{\text{Th}} \int |\langle I \mid \mathbf{p}\rangle|^2 \times \delta\left(\frac{\hbar^2 q^2}{2m} + \frac{\hbar\mathbf{p}\cdot\mathbf{q}}{m} - \hbar\omega\right) d\mathbf{p} \tag{4.6}$$

The p-space integral extends over a plane in the momentum space perpendicular to **q**, where the distance p_q of this plane from the origin of the momentum space is determined by

$$p_q = \frac{\omega m}{q} - \frac{\hbar q}{2} \tag{4.7}$$

where $\mathbf{q} \equiv \mathbf{k}_1 - \mathbf{k}_2$. Choosing **q** to lie in the z-direction so that $p_q = p_z$, one can write the Eq. 4.6 as follows

$$\frac{d^2\sigma}{d\Omega d\omega_2} = \left(\frac{d\sigma}{d\Omega}\right)_{\text{Th}} \left(\frac{m}{\hbar q}\right) \iint \rho\left(p_x, p_y, p_z = p_q\right) dp_x dp_y$$

$$\frac{d^2\sigma}{d\Omega d\omega_2} = \left(\frac{d\sigma}{d\Omega}\right)_{\text{Th}} \left(\frac{m}{\hbar q}\right) J\left(p_q\right) \tag{4.8}$$

where the term $J(p_q)$ is the CP. The area under the CP corresponds to the number of electrons Z per formula unit:

$$\int_{-\infty}^{+\infty} J\left(p_z\right) \mathrm{d}p_z = Z \tag{4.9}$$

In the case of a many electron system, one considers a system composed by i independent particles described by single particle wave functions $\psi_i(r_j)$, then each scattering process will involve just one particle, j, of the system. The momentum density can be expressed by summing up all occupied single-electron states of the system, i:

$$\rho\left(\mathbf{p}\right) = \left(\frac{1}{2\pi\hbar}\right)^3 |\langle I \mid \mathbf{p}\rangle|^2 = \left(\frac{1}{2\pi\hbar}\right)^3 \sum_i^{occ} \left| \int \psi_i\left(\mathbf{r}\right) e^{\frac{-i\mathbf{p}\cdot\mathbf{r}}{\hbar}} d\mathbf{r} \right|^2$$

$$= \sum_i^{occ} \left|\chi_i\left(\mathbf{p}\right)\right|^2 \tag{4.10}$$

where $\chi_i(\mathbf{p})$ is the Fourier transform of the i-th wave function. The N-particle density matrix derived from N-particle wave functions, Ψ_N, has the following form:

$$\Gamma_N\left(\mathbf{r}_1, \mathbf{r}_2, \ldots, \mathbf{r}_N \mid \mathbf{r}'_1, \mathbf{r}'_2, \ldots, \mathbf{r}'_N\right) \equiv$$

$$\Psi_N\left(\mathbf{r}_1, \mathbf{r}_2, \ldots, \mathbf{r}_N\right) \Psi_N^*\left(\mathbf{r}'_1, \mathbf{r}'_2, \ldots, \mathbf{r}'_N\right) \tag{4.11}$$

Then, the one-particle reduced density matrix is defined:

$$\Gamma_1\left(\mathbf{r}_1 \mid \mathbf{r}'_1\right) \equiv N \int \Gamma_N\left(\mathbf{r}_1, \mathbf{r}_2, \ldots, \mathbf{r}_N \mid \mathbf{r}'_1, \mathbf{r}'_2, \ldots, \mathbf{r}'_N\right) d\mathbf{r}_2 \ldots d\mathbf{r}_N \tag{4.12}$$

In the momentum space the one-particle reduced density matrix is the six-dimensional Fourier transform of the one-particle reduced density matrix in the position space:

$$\Gamma_1\left(\mathbf{p}_1 \mid \mathbf{p}_1'\right) \equiv \left(\frac{1}{2\pi\hbar}\right)^3 \int \Gamma_1\left(\mathbf{r}_1 \mid \mathbf{r}_1'\right) e^{\left[-\frac{i\left(\mathbf{p}_1\cdot\mathbf{r}_1 - \mathbf{p}_1'\cdot\mathbf{r}_1'\right)}{\hbar}\right]} d\mathbf{r}_1 d\mathbf{r}_1' \tag{4.13}$$

According to the impulse approximation the DDSCS for a system of particles can defined by the one-particle reduced density matrix, as follows [85]:

$$\begin{aligned}\frac{d^2\sigma}{d\Omega d\omega_2} = \left(\frac{d\sigma}{d\Omega}\right)_{\mathrm{Th}} \left(\frac{1}{2\pi\hbar}\right) \int dt e^{\left[-i\omega t + \frac{i\mathscr{E}\left(\mathbf{p}_{f1}\right)t}{\hbar} - \frac{i\mathscr{E}\left(\mathbf{p}_{f1}-\hbar\mathbf{q}\right)t}{\hbar}\right]} \\ \times \sum_{\mathbf{p}_{f1}} \iint e^{\left[i\left(\frac{\mathbf{p}_{f1}}{\hbar}-\mathbf{q}\right)\cdot\mathbf{r}_1\right]} e^{\left[-i\left(\frac{\mathbf{p}_{f1}}{\hbar}-\mathbf{q}\right)\cdot\mathbf{r}_1'\right]} \Gamma_1\left(\mathbf{r}_1 \mid \mathbf{r}_1'\right) d\mathbf{r}_1 d\mathbf{r}_1'\end{aligned} \tag{4.14}$$

where $\mathbf{p}_{f1} - \hbar\mathbf{q} = \mathbf{p}_1$ and $\mathscr{E}\left(\mathbf{p}_{f1}\right) = \mathbf{p}_{f1}^2/2m$. Now, replacing the Eq. 4.13 into Eq. 4.14, performing the $\mathbf{p}_1$ integration and the δ function property for integrals one can write the DDSCS as:

$$\frac{d^2\sigma}{d\Omega d\omega_2} = \left(\frac{d\sigma}{d\Omega}\right)_{\mathrm{Th}} \int \Gamma_1\left(\mathbf{p} \mid \mathbf{p}\right) \delta\left(\hbar\omega - \frac{\hbar^2 q^2}{2m} - \frac{\hbar\mathbf{p}\cdot\mathbf{q}}{m}\right) d\mathbf{p} \tag{4.15}$$

where the diagonal element of the one-particle reduced density matrix $\Gamma_1(\mathbf{p}|\mathbf{p}) = \rho(\mathbf{p})$. Therefore, Eq. 4.15 is the many electron equivalent of the Eq. 4.6. Thus, the CP can be evaluated from the integral in Eq. 4.15. Also, one can infer that Compton scattering is an experimental technique which allows direct access to the ground state EMD of a many body system. Also, from the EMD is possible to determine the Fermi surface topology, analyse the charge transfer in a compound and test the accuracy of theoretical models for electronic structure, just to mention some applications [86, 107, 108].

The Compton scattering experiments for this work were done in the SPring-8 synchrotron. Barium impregnated tungsten is the main component of the electron thermionic gun of SPring-8. Then, the emitted electrons are bunched in a beam and then accelerated up to 1 giga-electron volts (GeV) in the linear accelerator 'LINAC'. After that, the electron beam is injected in a booster synchrotron. It consists of a network of bending and quadrupole magnets where the electron beam is again accelerated up to 8 GeV. Next, the electron beam is injected to the storage ring. The storage ring has a circumference of 1436 m and it has 45 cells. A cell is composed by 2 bending magnets, 10 quadrupole magnets and 7 sextupole magnets. Thus, the

synchrotron radiation is extracted from the bending magnets. Between cells there are straight sections which contains the insertion devices. The insertion device used for Compton scattering experiments is the Elliptical Multipole Wiggler (EMPW) which produces linearly or circularly polarised photons [109].

BL08W is the only one of the 57 beamlines in SPring-8 which has an EMPW. Also, it delivers X-rays from 100 Kilo-electron volts (KeV) up to a maximum energy of 300 KeV, the highest of all the beamlines [109]. The X-rays generated by the wiggler are sent to the experimental station where the Compton scattering spectrometer, shown in Fig. 4.3, is located. There, the X-rays are focused and monochromatised by a double bent monochromator of Si 400. Next, the light beam hits the sample, the absorption is low due to the high energy of the X-rays, thus the bulk of the sample is probed. Following this, the scattered beam pass by a Ge 620 analyser. Subsequently,

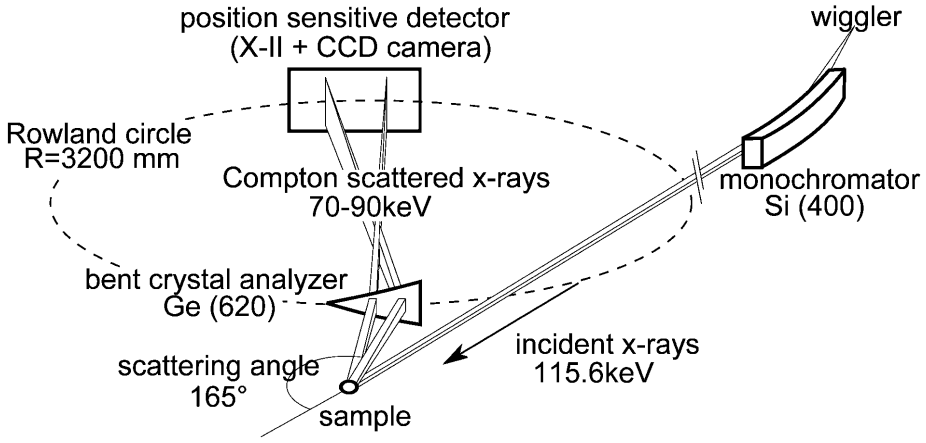

Figure 4.3: The high resolution Compton scattering spectrometer [10].

the beam is collected by a Charge Coupled Device (CCD) detector. Then, the collected spectrum can be stored as an image file where the ordered axis is the number of channel of the CCD and the abscissa is the number of photon counts. The CP could be obtained from the spectrum after a data analysis process.

For the study of HEAs, Compton scattering has been chosen over other characterisation methods. For example: Angle Resolved Photon Spectrometry (ARPES) is difficult since it is impossible to cleave the HEA to get a clean surface, positron annihilation is hindered by the fact that positrons could be trapped in any vacancies present in the samples and quantum oscillations are difficult to detect because the electron mean free path in HEAs is short [14].

4.2 Magnetic Compton Scattering

Magnetic Compton scattering is a powerful technique to measure the spin polarised electron momentum density due to the X-rays interact with the charge and the magnetic moment of an electronic system. Blume [110] derived the magnetic contribution to the relativistic DDSCS. The interaction of the electrons with the quantised electromagnetic field is given by the following Hamiltonian:

$$\begin{aligned} H' =& \frac{e^2}{2mc^2}\sum_j \mathbf{A}^2(\mathbf{r}_j) - \frac{e}{mc}\sum_j \mathbf{A}(\mathbf{r}_j)\cdot\mathbf{p}_j - \frac{e\hbar}{mc}\sum_j \mathbf{s}_j\cdot[\nabla\times\mathbf{A}(\mathbf{r}_j)] \\ & - \frac{\hbar}{2(mc)^2}\frac{e^2}{c^2}\sum_j \mathbf{s}_j\cdot\left[\frac{\partial\mathbf{A}(\mathbf{r}_j)}{\partial t}\times\mathbf{A}(\mathbf{r}_j)\right] \end{aligned} \tag{4.16}$$

where the summation is over all the electrons, $\mathbf{A}$ is the potential vector, $\mathbf{p}$ is the momentum operator of the electrons and $\mathbf{s}_j$ is the spin vector operator. The third term corresponds to the potential energy of the spin magnetic moment in the presence of the radiation magnetic field and the fourth term is part of the spin-orbit coupling.

The Fermi golden rule until the second order of perturbation is used to calculate the transition probability. Thus, the quadratic terms of Eq. 4.16 are included in the first order term and its linear terms in the second order term [110]. Finally, the DDSCS can be obtained multiplying the transition probability by the density of final states and dividing by the incident flux, so that

$$\begin{aligned} \frac{d^2\sigma}{d\Omega d\omega_2} = r_e^2(\omega_2/\omega_1)\sum_F & |\langle F|\sum_j \exp(i\mathbf{q}\cdot\mathbf{r}_j)|I\rangle(\hat{\varepsilon}_1\cdot\hat{\varepsilon}_2^*) \\ & -i\left(\hbar\omega_1/mc^2\right)\langle F|\sum_j \exp(i\mathbf{q}\cdot\mathbf{r}_j) \\ & \times\left(i\left(\mathbf{q}\times\mathbf{p}_j/\hbar\mathbf{k}_1^2\right)\cdot\mathbf{C}+\mathbf{s}_j\cdot\mathbf{B}\right)|I\rangle\,|^2 \\ & \times\delta(E_I-E_F-\hbar\omega) \end{aligned} \tag{4.17}$$

where $\mathbf{C}=\hat{\varepsilon}_2^*\times\hat{\varepsilon}_1$, $\mathbf{B}=(\hat{\varepsilon}_2^*\times\hat{\varepsilon}_1)+(\hat{\mathbf{k}}_2\times\hat{\varepsilon}_2^*)(\hat{\mathbf{k}}_2\cdot\hat{\varepsilon}_1)-(\hat{\mathbf{k}}_1\times\hat{\varepsilon}_1^*)(\hat{\mathbf{k}}_1\cdot\hat{\varepsilon}_2^*)-(\hat{\mathbf{k}}_2\times\hat{\varepsilon}_2^*)(\hat{\mathbf{k}}_1\times\hat{\varepsilon}_1)$, the incoming photon has a unit wavevector $\hat{\mathbf{k}}_1$, energy ω_1 and unit polarisation vector $\hat{\varepsilon}_1$ and the

scattered photon has a unit wavevector $\hat{\mathbf{k}}_2$, energy ω_2 and unit polarisation vector $\hat{\varepsilon}_2$. Also, the complex conjugate of the unit polarisation vectors is denoted by asterisk.

The first term of Eq. 4.17 represents the charge scattering and the second term represents the magnetic scattering conformed by the orbital and spin contribution. Then, **C** and **B** give the polarisation dependence of each magnetic contribution respectively.

Now, considering the one electron case in the IA, using plane waves $exp(i\mathbf{p}_f \cdot \mathbf{r}/\hbar)$ for the final states and the cancellation of the potential energy in the energy-conserving δ function is possible to estimate the orbital magnetic DDSCS from the Eq. 4.17. Then, the orbital magnetic DDSCS is expressed as

$$\left(\frac{d^2\sigma}{d\Omega d\omega_2}\right)_{\text{orb mag}} = r_e^2\left(\omega_2/\omega_1\right)\left(\hbar\omega_1/mc^2\right)\sum_{\mathbf{p}}|\langle I|\mathbf{p}\rangle|^2\left(\hat{\varepsilon}_1\cdot\hat{\varepsilon}_2^*\right)\times \left(\mathbf{q}\times\mathbf{p}/\hbar\mathbf{k}_1^2\right)\cdot\left(\hat{\varepsilon}_2^*\times\hat{\varepsilon}_1\right)\delta\left(\hbar\omega-\hbar^2q^2/2m-\hbar\mathbf{p}\cdot\mathbf{q}/m\right) \tag{4.18}$$

The Eq. 4.18 reduces to zero assuming that the atomic orbitals of the electrons in the state $|I\rangle$ possess inversion symmetry in the momentum space and transforming the summation into an integral as in the procedure to get Eq. 4.6.

Neglecting the contribution of the orbital momentum in magnetic Compton scattering experiments is achieved using a circularly polarised X-ray beam generated by the EMPW and choosing the geometry shown in Fig. 4.4 . The use of circularly polarised X-rays can be justified

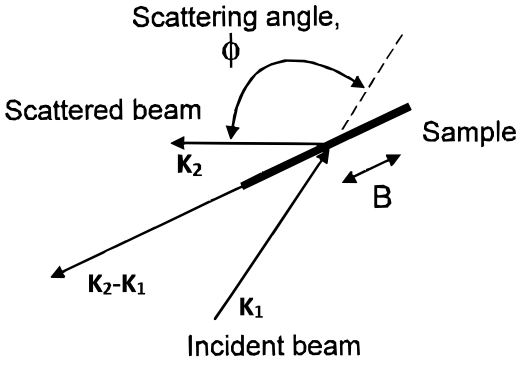

Figure 4.4: The scattering geometry adopted in a magnetic Compton scattering experiment [11].

considering the second factor in Eq. 4.17 which represents the magnetic scattering amplitude. From this factor, it is possible to get the interference term which is proportional to the difference $\rho_\uparrow(\mathbf{p}) - \rho_\downarrow(\mathbf{p})$. Then, the interference term can be found if the structure is non-centrosymmetric

or only if the polarisation factors of the second term are complex. Indeed, complex polarisation factors will occur if the incident photon is circularly polarised or if the degree of circular polarisation of the scattered photon can be determined.

The selected geometry is motivated because the magnitude of the magnetic scattering cross section depends on the angle of the incident photon. Then, the maximum value of the magnetic scattering cross section is achieved for a scattering angle of 180° [106] this is called back-scattering geometry. Therefore, the external magnetic field also has to be parallel to the scattering vector.

After the orbital magnetic contribution has been discarded from the DDSCS in Eq. 4.17. The resultant DDSCS, first derived by Platzman and Tzoar [101], can be written as [111]:

$$\frac{d^2\sigma}{d\Omega dE_2} = \left(\frac{e^2}{mc^2}\right)^2 \left(\frac{m}{2\hbar K}\right) \left(\frac{E_2}{E_1}\right)^2 \times \left\{ \left[1+\cos^2\phi + P_l \sin^2\phi + \frac{(k_1-k_2)}{mc^2}(1-\cos\phi)\right] J(p_z) + \left[(\cos\phi - 1) P_c \hat{\sigma} \cdot \frac{(\mathbf{k}_1 \cos\phi + \mathbf{k}_2)}{mc}\right] J_{mag}(p_z) \right\} \tag{4.19}$$

where E_1 and E_2 are the incident and scattered photon energies respectively, P_l and P_c describe the linear and circular polarisations respectively, and $\hat{\sigma}$ is a unit vector parallel to the direction of the sample magnetisation. To align the magnetic moment of the sample parallel or antiparallel to the scattering vector, $\mathbf{k}_1 cos\phi + \mathbf{k}_2$, a reversible magnetic field is applied. The strength of the applied magnetic field depends on the residual magnetisation of the sample that means how difficult is to reverse the magnetisation of the sample. Then, the sign of the $J_{mag}(p_z)$ term in Eq. 4.19 can be reversed changing the direction of the field or the sense of the circular polarisation. Next, subtracting two spectra obtained with two opposite field directions, so the charge scattering term is cancelled, one can isolate the magnetic term $J_{mag}(p_z)$ also known as the MCP:

$$J_{mag}(p_z) = \iint \left[\rho_\uparrow(\mathbf{p}) - \rho_\downarrow(\mathbf{p})\right] dp_x dp_y \tag{4.20}$$

where $\rho_\uparrow(\mathbf{p})$ and $\rho_\downarrow(\mathbf{p})$ represent the spin polarised electron momentum density for the majority and minority spin bands respectively and the z-axis is parallel to the scattering vector $\mathbf{K} =$

$\mathbf{k}_1 - \mathbf{k}_2$. Thereby, only unpaired spin electrons are considered and some systematic error sources are eliminated. Finally, the resultant magnetic Compton spectra is corrected similarly to the conventional Compton spectra.

A great variety of magnetic materials could be studied with magnetic Compton scattering. Ferromagnetic, ferrimagnetic and paramagnetic materials with a large induced spin moment by large fields can be probed. However, no magnetic signal can be obtained from antiferromagnets with this method because Compton scattering is an incoherent process [112].

The area under the MCP corresponds to the total spin moment μ_s per formula unit or the number of unpaired electrons per formula unit:

$$\int_{-\infty}^{+\infty} J_{mag}(p_z)\,\mathrm{d}p_z = \mu_s \tag{4.21}$$

The MCP can be interpreted through electronic structure calculations because is possible to identify which states contribute to the spin density. Also, partial spin moments and their orientation with respect to external fields can be obtained. Finally, the orbital spin moment also can be determined because this is the difference between the bulk magnetic moment and the spin magnetic moment. The bulk magnetic moment can be measured using auxiliary techniques as Superconducting Quantum Interference Device (SQUID) magnetometry.

Fig. 4.5 show the magnetic Compton scattering spectrometer. It consists of a EMPW where the

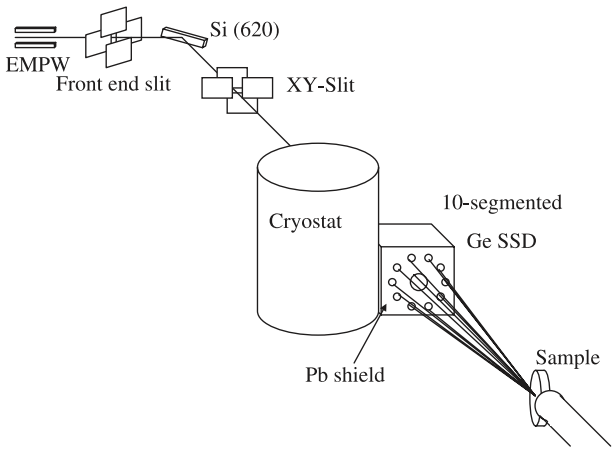

Figure 4.5: Schematic view of experimental setup of a magnetic Compton scattering [12].

circularly polarised X-rays are emitted, then the X-rays pass through a XY slit which is used to remove the unwanted part of the synchrotron radiation and to reduce the heat load over the

next components [113, 114]. After that, the circularly polarised X-rays are monochromatised to 175 KeV using an asymmetric Johann type Si 620 single crystal. Following this, the X-ray beam passes through the central hole of a Pb shield and hits the sample mounted inside the 'Spectromag'. Thus, the X-rays are scattered in an angle of 173° towards the Pb shield which contains a 10 segmented Ge Solid State Detector (SSD) each one with a Digital Signal Processing (DSP)-based Multi-Channel Analyser (MCA) system. Each section of the Ge SSD creates a charge pulse by the absorption of an X-ray. Next, the charge pulse is converted to a voltage pulse and analysed in the MCA system. The momentum resolution of the spectrometer is 0.45 atomic units (a.u.) where 1 a.u. $=1.99\times10^{-24}$ Kgms^{-1} and the maximum count rate is $\sim$ 1 million counts per second [12].

The Spectromag designed by Oxford Instruments shown in Fig. 4.6 has three main sections. On

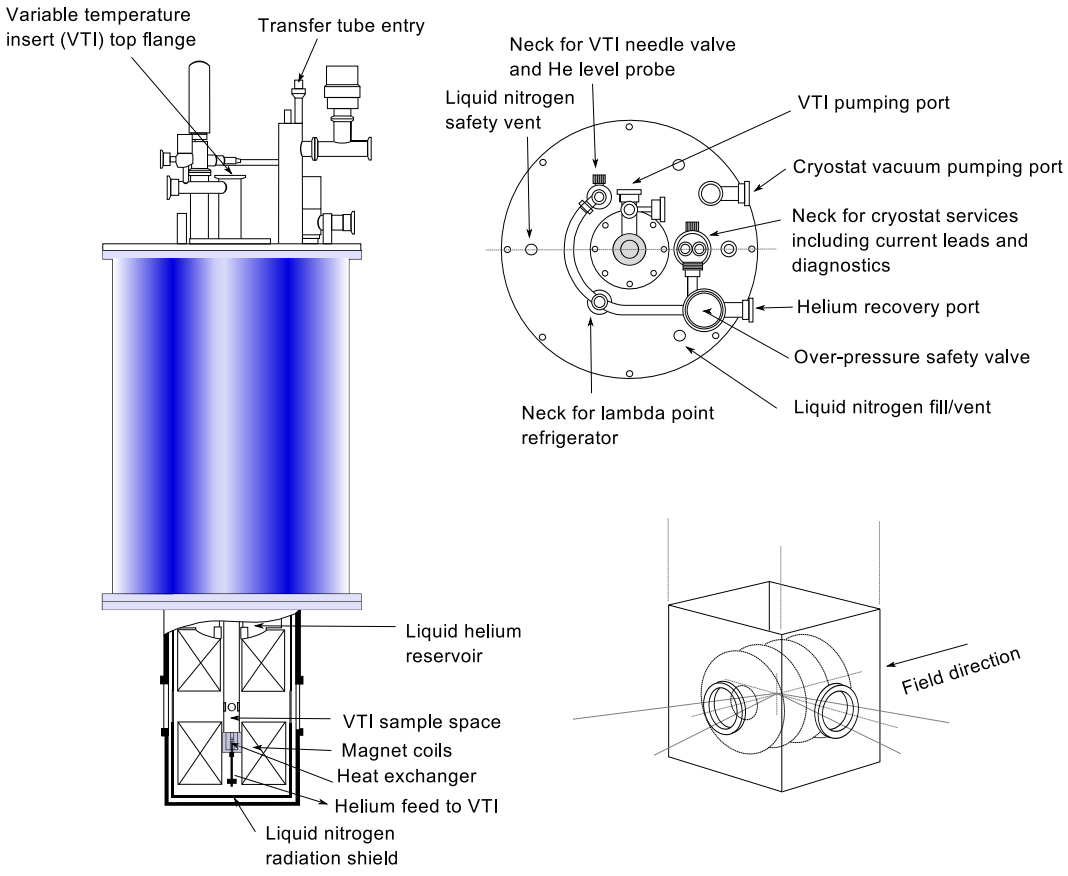

Figure 4.6: Schematic diagram of the Spectromag used in the HEAs experiments on BL08W [13].

the top, one can find a set of vents, ports and valves to control the input and output of refrigerant liquids needed to cold down the sample and the superconducting magnet. Also, there is an entry

for the Variable Temperature Insert (VTI) which contains the sample holder attached to a micro-goniometer. The cryostat system is placed in the middle section, it includes the storage tanks for liquid He and N_2. Liquid He is necessary for cooling down the magnet coils and the sample. At the bottom, one can find a chamber with two optical windows for X-ray access. The magnet coils of the magnet are located in this section as well. Thus, a maximum field of 9 T is generated by the superconducting magnet. The tip of the VTI can be placed between the superconducting magnet facing to the optical windows. Further, liquid N_2 is used as a radiation shield of the chamber.

4.3 Data Analysis

In a magnetic Compton scattering experiment the registered spectrum I is a convolution of the DDSCS shown in Eq. 4.19 with the resolution function of the magnetic Compton spectrometer. To start an experiment is necessary to align the sample in a determined direction. Next, the magnetic field is applied in the direction of the scattering vector as in Fig. 4.4. Subsequently, the X-ray beam is scattered and the photon counts are registered by the SSD. All the events not related with single magnetic Compton scattering are considered as background. Next, the field is reversed, hence one subtracts two spectra with two opposite magnetisations to obtain the MCP. Also, as a consequence of this operation the background contributions are suppressed. The data is taken in the following field direction sequence: '$+,-,-,+,-,+,+,-$' to minimize the effects due to the polarisation of the beam is changing slowly over time then it is necessary to average over that. The signs $+$, $-$ represents the two possible field directions. Then, the time of measurement is divided into cycles, for example $+,-,-,+$ where each sign represents a number of scans. Thus, the spectra can be easily normalised to the monitor count number, proportional to the mean intensity of the synchrotron beam and time of the measurement, registered by the detector. In this way, the possibility of introducing systematic errors into the data is reduced.
The first step of the data analysis is to fit the peaks of the measured CP with the correspondent peaks $K_{\alpha 1,2}$ and $K_{\beta 1,2}$ of the fluorescent spectra of Pb as can be seen in Fig. 4.7 courtesy of Daniel O'Neill. The peaks of Pb have a well defined energy which allows to relate the channel number with the energy Thus, it is possible to get the energy calibration of the spectra. The

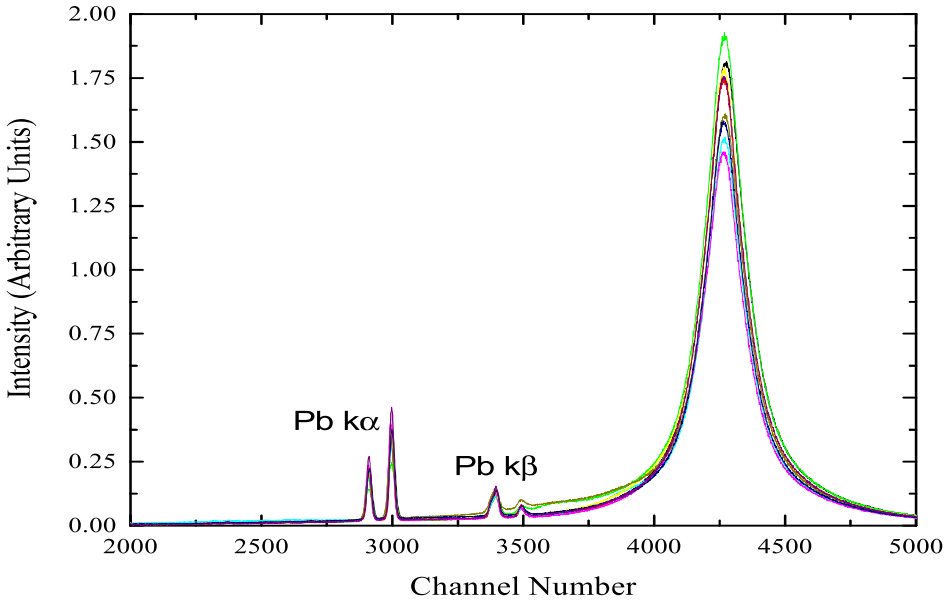

Figure 4.7: Raw Ni data collected at 300 K and 1 T. The differences between Compton peaks of each detector is due to their different calibrations and this is fixed relating the channel number with the well defined energy of Pb fluorescence peaks.

next step in the data processing consists in conversion of the energy scale of the spectrum to the momentum scale using the relativistic relationship [115]:

$$p_z = \left[\frac{|\mathbf{q}|}{2} + \frac{(E_2 - E_1)}{2} \sqrt{1 + \frac{2mc^2}{E_2 E_1 (1 - \cos\phi)}} \right] \cdot \frac{1}{\alpha mc^2} \tag{4.22}$$

where p_z has the same direction of the scattering vector and it is expressed in a.u., the energy is in KeV, the factor $1/\alpha mc^2 = 137.036/511$ where α is the fine-structure constant, $|\mathbf{q}|$ is the length of the scattering vector:

$$|\mathbf{q}| = |\mathbf{k}_1 - \mathbf{k}_2| = \sqrt{E_2^2 + E_1^2 - 2E_1 E_2 \cos\phi} \tag{4.23}$$

Subsequently, the data sets taken in each field direction are checked looking for some anomalies in the spectra such as discontinuities or missing features. Hence, the Ge SSD is segmented in ten parts each one collects one spectrum. If some spectra presents a non-symmetric shape, it is possible that the respective segment of the detector is failing. Thus, it is possible to recognize which spectrum should be excluded from the analysis.

Another reason that can affect the shape of the spectrum is the variation in the count rates. This problem could be solved normalising the spectrum for comparison purposes. However,

significant variations in the count rate can be associated with failures in determined segment of the detector or a wrong scattering geometry in the experiment. Once the quality of data has been insured, the spectrum of each segment of detector are ready to be summed.

Then, the spectrum of all the segments of the detector are summed taking account the direction of the magnetic field. Thus, the MCP is calculated taking difference between the total spectrum of both directions of magnetisation. The experimental statistics can be improved because the MCP is symmetrical about $p_z = 0$. Then, the MCP is folded and binned to double the number of data points. In this way, one gets the *folded* MCP.

After that, it is possible to estimate the error in a counting process such as the number of photons detected during a magnetic Compton scattering experiment [116]. The Poisson distribution is useful to solve this issue, hence for a large number of collected counts N the respective error is equal to $\sqrt{N}$ [117]. Also, this error is propagated when the spectrum are summed and in the MCP folding and binning.

Following this, the MCP should be normalised to the number of unpaired electrons per formula unit, that is to the magnetic moment in Bohr magnetons. The ratio between the magnetic scattering compared and the charge scattering is called the 'flipping ratio' and it is defined such that [118]

$$R = \frac{I^{\uparrow} - I^{\downarrow}}{I^{\uparrow} + I^{\downarrow}} \tag{4.24}$$

where $I^{\uparrow}$ and $I^{\downarrow}$ are the integrated Compton scattered spectra intensities for opposite sample magnetisations. Then, the 'flipping ratio' is proportional to the spin moment per electron contributing to the MCP. However, to determine this ratio is necessary to know for example: the degree of circular polarisation of the incident photons and the response of the detector to a photon of a given energy. Unfortunately, those parameters are very difficult to measure with enough accuracy to get a MCP in absolute units of number of electrons per momentum unit [85]. For this reason, one should measure the MCP of a reference sample with a well known spin magnetic moment, such as Ni which posses a spin magnetic moment equal to 0.56 μ_B [11], in exactly the same experimental conditions. Thus, it is possible to get a relation between the spin magnetic moments of the reference sample and the unknown sample as follows:

$$\mu_{\mathrm{s}}(\mathrm{sample}) = \frac{R_{\mathrm{sample}}}{R_{\mathrm{Ni}}} \frac{Z_{\mathrm{sample}}}{Z_{\mathrm{Ni}}} \mu_{\mathrm{s}}(\mathrm{Ni}) \tag{4.25}$$

where R_{sample} and R_{Ni} are the flipping ratios of the unknown sample and Ni, the Z_{sample} and Z_{Ni} is the number of electrons in the unknown sample and Ni contributing to the total Compton scattering intensity.

Finally, it is possible to determine the resolution of the experiment by the relations:

$$p_z = mc\frac{E_2 - E_1 + \frac{E_1 E_2}{mc^2}(1-\cos\phi)}{\sqrt{E_1^2 + E_2^2 - 2E_1E_2\cos\phi}} \tag{4.26}$$

$$\Delta p_z = \sqrt{\left(\frac{\partial p_z}{\partial E_1}\Delta E_1\right)^2 + \left(\frac{\partial p_z}{\partial E_2}\Delta E_2\right)^2 + \left(\frac{\partial p_z}{\partial \phi}\Delta\phi\right)^2} \tag{4.27}$$

where E_1 and E_2 are the incident and the scattered X-ray energies, ϕ is the scattering angle and mc^2 the rest mass energy of the electron [85]. In Eq. 4.27, the energy broadening in the first term ΔE_1 corresponds to the source, the second ΔE_2 to the detector and $\Delta\phi$ is the geometrical broadening.

The goal is to set up the parameters of the experiment trying to obtain a good resolution, hence it is important to observe with detail the low momentum region of the MCP, that is only in the first few a.u. where the valence electrons contribute to the 'Fermi surface features'. The high momentum region of the MCP does not have many surprises because the core levels contribution becomes more important and it resembles the Hartree-Fock profiles of the free atom. The most tightly bound electrons are unaware that they are in a crystal. For instance, the source broadening is related to the energy spread of the beam caused by the monochromator in synchrotron experiments, thus the smallest broadening is achieved in backscattering where ϕ is close to 180°. Additionally, the detector broadening in Ge SSD depends on the energy of the scattered photon, then depending on if its energy is low or high there are some scattering angles which can improve the resolution of the detector. Finally, the geometrical broadening depends on the finite sizes of the sample, source, detector and also other optics elements used in the experiment. Thus, for magnetic Compton scattering the backscattering geometry reduces the geometrical broadening [85].

Chapter 5

The Electronic Structure and Magnetisation of NiFeCoCr HEA

The magnetism of transition metal alloys has been studied for a long time. For example, the Slater-Pauling curve for binary alloys shown in Ch. 2 is evidence of this. However, while the number of constituent elements is increased the chemical disorder of the alloy may increase as well. Then, unexpected and promising properties could emerge due to the complexity of the alloy.

There are seven families of Concentrated Complex Alloys (CCAs) [47] depending on their constituent elements: 3d transition metals, refractory metals, light metals, lanthanide (4f) transition metals, brasses and bronzes, precious metals and interstitial compounds (borides, carbides and nitrides).

The 3d transition metals in equiatomic proportions form FCC solid solutions [119]. This solid solutions can be binary, ternary, quaternary, etc. For instance, NiFeCoCrMn is the so called Cantor alloy [120]. Adding Pd to the elements of the Cantor alloy, one gets a new set of alloys called Cantor-Wu alloys [119]. The last decade, many studies have been done with the goal of unveiling the electrical and thermal transport, mechanical and magnetic properties of these alloys, especially of NiFeCoCr HEA [121, 122, 119, 123].

In the present chapter, the electronic structure of the NiFeCoCr HEA will be studied from Ab-initio methods. Also, using the MDME, details about the electrons responsible for its magnetic

properties will be elucidated.

5.1 Fermi Surface Smearing in Disordered Alloys

HEAs present a lack of translational symmetry or long range order. However, the concepts of BZ and Fermi surface can be resurrected in these disordered systems as was mentioned in Ch. 1. Finding the energy dispersion relation in disordered alloys requires a sophisticated analysis according to the method used to calculate the electronic structure, for instance: Effective Band Structure (EBS) for Supercell (SC) calculations with the PAW method or Bloch Spectral Functions (BSFs) for the KKR-CPA method [80, 124].

Actually, modelling Ni-based HEAs by the KKR-CPA method clearly shows that the Bloch states are not eigenstates of the system as a consequence of the random site occupancy by different elements [14]. Then, the electron states have finite lifetimes due to the chemical disorder and the bands are smeared in both energy, E (resulting in a finite electron lifetime) and crystal momentum, $\mathbf{k}$ (finite mean free path) [125]. As shown in Fig. 5.1, the BSFs look smeared out near the Fermi energy for binary and quaternary alloys. The presence of smearing in the BSF of ternary Ni-alloys such as NiCoFe and NiCoCr also has been reported by Jin *et al.* [33]. A couple

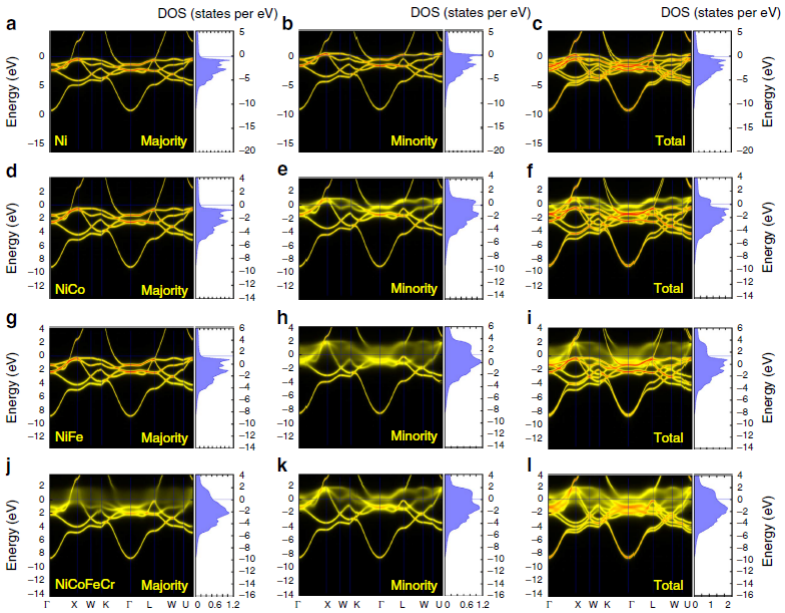

Figure 5.1: Bloch spectral function of majority spin, minority spin and total, and density of states (DOS) of (a), (b) and (c) Ni, (d), (e) and (f) NiCo, (g), (h) and (i) NiFe and (j), (k) and (l) NiFeCoCr HEA [14].

of obvious questions emerge from the smearing in the band structure owing to the compositional disorder, namely how the compositional disorder affects the shape of the Fermi surface in 3d

transition metals HEAs, and how the MDME smearing influences the magnetic properties of those alloys?.

The first question has already been answered by Robarts *et al.* [125]. Therefore, the next sections aim to give a comprehensive account of the magnetism in NiFeCoCr HEA by MDME studies.

The experimental work done by our group to determine the Fermi surface of NiFeCoCr HEA was done using high-resolution Compton scattering. The CPs were measured on a single crystal of NiFeCoCr using the SPring-8 spectrometer shown in Fig. 4.3. The sample was prepared by arc melting Ni, Fe, Co and Cr in a water-cooled copper hearth, under an Ar atmosphere [125]. Then, it was cut into a semi circle shape using electro-discharge machining, and it was electrolytically polished to remove any damaged provoked during the cutting. Finally, the sample with approximate dimensions of $1.7\times4\times7.5$ mm was placed on a sample holder provided with a goniometer.

The CPs were measured along 15 'special directions' within the BZ at room temperature, see Table 5.1. This particular set of crystallographic directions [15] is chosen because of the cubic symmetry of NiFeCoCr HEA. The goal was to reconstruct the 3D EMD from the measured CPs by lattice harmonic expansion in the method proposed by Kontrym-Sznajd and Samsel-Czekala [126].

The incident X-ray energy was 115 KeV and the momentum resolution was estimated to be 0.10 a.u.. The whole experiment last five days and each CP contained about 800,000 counts in the Compton peak. Also, background measurements were taken for subsequent corrections in the data analysis. The results of this experiment were published on [125].

Table 5.1: The set of 15 'special directions' measured in the Compton scattering experiment, taken from [15]. The [100] direction is specified by (θ, ϕ) being (90°,0°) and [110] by (90°, 45°).

Number	ϕ (degrees)	θ (degrees)
1	4.52	85.54
2	13.50	85.62
3	13.50	76.86
4	22.50	85.84
5	22.50	77.49
6	22.54	69.10
7	31.50	86.16
8	31.50	78.43
9	31.50	70.54
10	31.50	62.41
11	40.50	86.62
12	40.50	79.80
13	40.51	72.81
14	40.44	65.59
15	41.15	58.82

5.2 Equiatomic NiFeCoCr HEA

NiFeCoCr HEA belongs to the most studied families of HEAs: 3d transition metal CCAs or Single Phase Concentrated Solid Solution Alloys (SP-CSAs) [14]. This family can be considered extensions of stainless steels and superalloys because those compounds contains Fe, Cr and Ni as principal elements [47].

Energy Dispersive X-ray Spectrometry (EDS) revealed a uniform chemical composition without visible segregation of any constituent element in equiatomic NiFeCoCr HEA [127]. Atom Probe Tomography (APT) has proved that there is not clustering or short-range order [128]. Also, there is not evidence of long-range chemical ordering from either neutron and anomalous X-ray scattering [121]. Their atoms are placed in a FCC structure according powder XRD experiments, where the lattice parameter corresponds to a=3.58 Å [129]. The migration of its constituent species was investigated by DFT where Cr presented the lowest migration energy followed by Co, Fe and Ni [130].

At room temperature NiFeCoCr is paramagnetic, since its Curie temperature T_C is $\approx$120

K [33, 131]. Several values of saturation magnetisation at room temperature have been reported, and they depend on the method for the synthesis of the sample. For instance: 0.03 μ_B/atom with a sample prepared by arc melting using 96.06% Fe and pure Co, Cr and Ni [132], 0.24 μ_B/atom with a sample prepared arc melting with the appropriate amounts of pure Ni, Fe, Co and Cr [33], and $\approx$0.14 μ_B/atom with a sample prepared by ball milling pure elemental powders [133]. The magnetisation at 1.8 K is $\approx$0.53 μ_B/atom [133].

The single crystal sample used in the magnetic Compton scattering experiments was prepared by arc melting Ni, Fe, Co and Cr in a water-cooled copper hearth, under an Ar atmosphere [125] with approximate dimensions of $3\times3\times2$ mm. The bulk magnetic moment measured on a SQUID was 0.248 μ_B/atom. The spin magnetic moment obtained by magnetic Compton scattering was 0.231 μ_B/atom. Therefore, the orbital magnetic moment corresponds to 0.017 μ_B/atom.

On the other hand, DFT calculations show the ferromagnetic behaviour of Ni, Fe, Co and most of the spin magnetic moments of Cr coupled in the opposite direction of the former elements as has been observed by Niu *et al.* [133]. Also, Calvo-Dahlborg *et al.* [134] reports a ferromagnetic alignment of the magnetic moments of Ni, Fe, Co with Cr magnetic moments coupled in opposite direction. There is also experimental evidence of this magnetic structure in experiments of X-ray Magnetic Circular Dichroism (XMCD) done by our group [135].

NiFeCoCr HEAs possess unusual combinations of strength, ductility, thermal stability, corrosion, and wear resistance [136]. They exhibit a Yield Strength (YS) of 359 MPa [122] or 271 MPa [137], an Ultimate Tensile Strength (UTS) of 712.5 MPa [122], and a total elongation of 56% [122]. Also, the alloy possesses an excellent strain hardening capability. NiFeCoCr compared with austenitic steels appears to have similar plasticity, but much higher strength [122]. The dislocation lines in HEAs are not straight due to the local lattice distortion, which makes the deformation mechanism of HEAs different from that of traditional alloys [138].

The electrical resistivity at 5 K is 77.1 $\mu\Omega$cm [14] and it reaches approximately 91 $\mu\Omega$cm [14, 33] when the temperature increases at 300 K. Then, NiFeCoCr has higher electrical resistivity than a typical conductor like Cu which has an electrical resistivity of 1.72 $\mu\Omega$cm [139] at 300 K. This electronic transport property is important to study the energy transport under radiation for nuclear construction applications [140].

The total thermal conductivity at 50 K is 6.2 $Wm^{-1}K^{-1}$ [33], meanwhile at room temperature

is 12.9 $Wm^{-1}K^{-1}$ [137]. The increment of thermal conductivity in this interval of temperature is due to the high residual resistivity of approximately 77.1 $\mu\Omega$cm [33]. This behaviour differs from pure metals where the thermal conductivity starts to decrease at a few tens of K.

The specific heat capacity at constant pressure C_p is 0.456 $Jg^{-1}K^{-1}$ [137]. It has been found that the temperature dependence of the specific heat is influenced by the magnetic state and possible short range order-disorder transitions [140]. Therefore, NiFeCoCr could be used for magnetic refrigeration applications [141].

For all above, the determination of the electronic structure and the magnetisation of equiatomic NiFeCoCr HEA becomes an important task to increase the knowledge about this alloy.

5.3 Electronic Structure Calculations on NiFeCoCr HEA

As was discussed in Ch. 3, the compositional disorder present in a HEA can be simulated by two principal methods: the SQS method and the CPA method. In the present work SQS within DFT were used to study the electronic structure and determine the MCPs of NiFeCoCr HEA. Also, KKR-CPA calculations were done by S. B. Dugdale using the LDA-VWN as exchange-correlation functional. They are presented as a complement to understand the physics behind HEAs.

Two supercells of NiFeCoCr with 32 and 72 atoms were created by the ATAT package with a lattice parameter a=3.58 Å [129] (Figs. 5.2a and 5.3a). The structural relaxation of the NiFeCoCr SQS of 32 atoms was done in the Quantum Espresso package with the BFGS algorithm using a US PP with the GGA-PBE approximation for the exchange-correlation functional [76]. The convergence was achieved with 20 **k**-points in the Irreducible Part of the Brillouin Zone (IBZ) equivalent to a **k**-point mesh of $2 \times 4 \times 4$. The wave-function and charge-density cut-offs were 90 Ry and 500 Ry respectively. After that, a spin polarised calculation with the GGA-PBE [68] approximation for the exchange-correlation functional was done using the Elk code with an APW+lo basis. The calculation with the SQS of 32 atoms converged on 256 **k**-points within the IBZ equivalent to a **k**-point mesh of $4 \times 8 \times 8$. The cut-off for plane waves in the interstitial

region defined by $|\mathbf{G}+\mathbf{k}|_{\mathbf{max}}=7/\bar{r}_{MT}$ where $\bar{r}_{MT}$ is the average muffin-tin radius.

The spin magnetic moment for this SQS was 0.514 μ_B/atom, whereas the spin magnetic moment

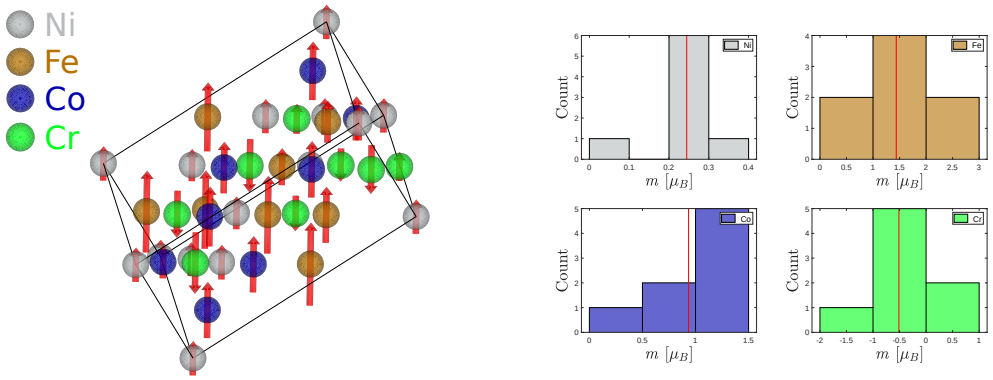

(a) (b)

Figure 5.2: (a) SQS supercell of 32 atoms used to model NiFeCoCr HEA. The red arrows represent the projection of the spin moment in the z-direction, their magnitude is scaled to the results obtained from the DFT calculations done with the Elk code. (b) Histogram of the distribution of atoms of the SQS according to their spin magnetic moment m.

with the KKR-CPA method was 0.650 μ_B/atom and the magnetic orbital moment was 0.033 μ_B/atom. This magnetic orbital moment corresponds to 4.83% of the total magnetic moment in the KKR-CPA method. Then, it was decided not consider the Spin Orbit Coupling (SOC) for the SQS method because SOC increases considerably the computation time in SC calculations.

Fig. 5.2a shows the magnetic structure where the spin moments of Ni, Fe, Co atoms are aligned in the same direction but Cr present both spin directions along the z-axis with most of the atoms with an opposed direction to the former elements. The average spin moment (red line in Fig. 5.2b) of each species for the SQS of 32 atoms, KKR-CPA calculations and XMCD measurements are summarised in Table 5.2. There is a satisfactory agreement between these observations and the works done by Niu *et al.* [133] and Calvo-Dahlborg *et al.* [134].

For the NiFeCoCr SQS of 72 atoms, the structural relaxation was done also in Quantum Espresso with the BFGS algorithm using the same exchange-correlation functional as in the SQS of 32 atoms. Then, the convergence was achieved with 2 **k**-points in the IBZ equivalent to a **k**-point mesh of $2 \times 1 \times 1$. The wave-function and charge-density cut-offs were 90 Ry and 500 Ry respectively. After that, a spin polarised calculation with the GGA-PBE [68] approximation for the exchange-correlation functional was done using the Elk code with an APW+lo basis. The calculation with the SQS of 72 atoms converged on 32 **k**-points within the IBZ equivalent to

Table 5.2: The spin magnetic moments of NiFeCoCr HEA from the SQS of 32 atoms, SQS of 72 atoms, SQS-$L2_1$, KKR-CPA calculations and XMCD measurements.

Alloy	Species	SQS-32 atoms	SQS-72 atoms	SQS-$L2_1$	KKR-CPA	XMCD
		m^{spin} (μ_B)	m^{spin} (μ_B)	m^{spin} (μ_B)	m^{spin} (μ_B)	$m_z^{spin,eff}$ (μ_B)
NiFeCoCr	Ni	0.245	0.183	0.133	0.274	0.508
	Fe	1.438	1.598	1.680	1.915	1.776
	Co	0.934	0.899	0.746	1.061	1.125
	Cr	-0.512	-0.578	-1.732	-0.651	-0.758
NiFeCoCr	Average	0.514	0.509	0.174	0.650	0.662

a **k**-point mesh of $2 \times 4 \times 4$. The cut-off for plane waves in the interstitial region defined by $|\mathbf{G}+\mathbf{k}|_{\mathbf{max}}=7/\bar{r}_{MT}$ where $\bar{r}_{MT}$ is the average muffin-tin radius.

The magnetic structure (Fig. 5.3a) was the same as in the SQS of 32 atoms. The spin magnetic moment of the SQS of 72 atoms was 0.509 μ_B/atom. The average spin moment (red line in Fig. 5.3b) of each species with the SQS of 72 atoms is summarised in Table 5.2. These values are very close to the respective values found with the SQS of 32 atoms.

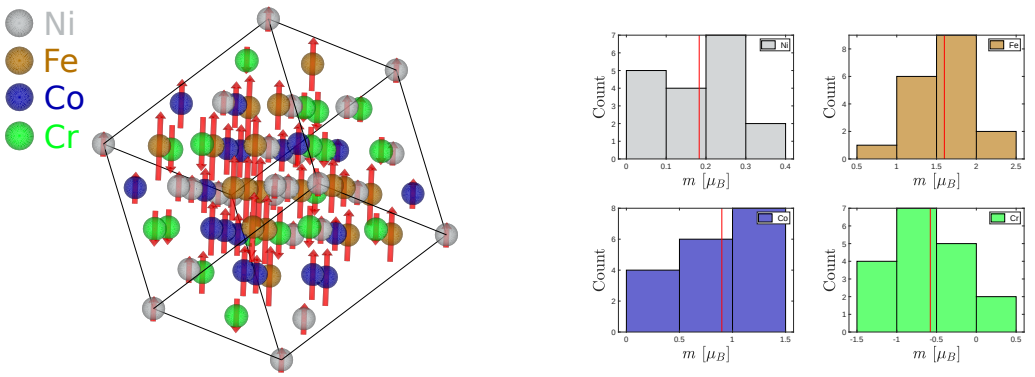

(a) (b)

Figure 5.3: (a) SQS supercell of 72 atoms used to model NiFeCoCr HEA. The red arrows represent the projection of the spin moment in the z-direction, their magnitude is scaled to the results obtained from the DFT calculations done with the Elk code. (b) Histogram of the distribution of atoms of the SQS according to their spin magnetic moment m.

The DOS (Fig. 5.4a) of NiFeCoCr modelled with a SQS of 32 atoms at the Fermi level in the majority spin band was 16.72 states/cell eV and in the minority spin was -22.65 states/cell eV. The negative sign in the minority spin is only to differentiate from the majority spin but both are positives in reality. At the Fermi level the contribution of the Partial Density of States (PDOS)

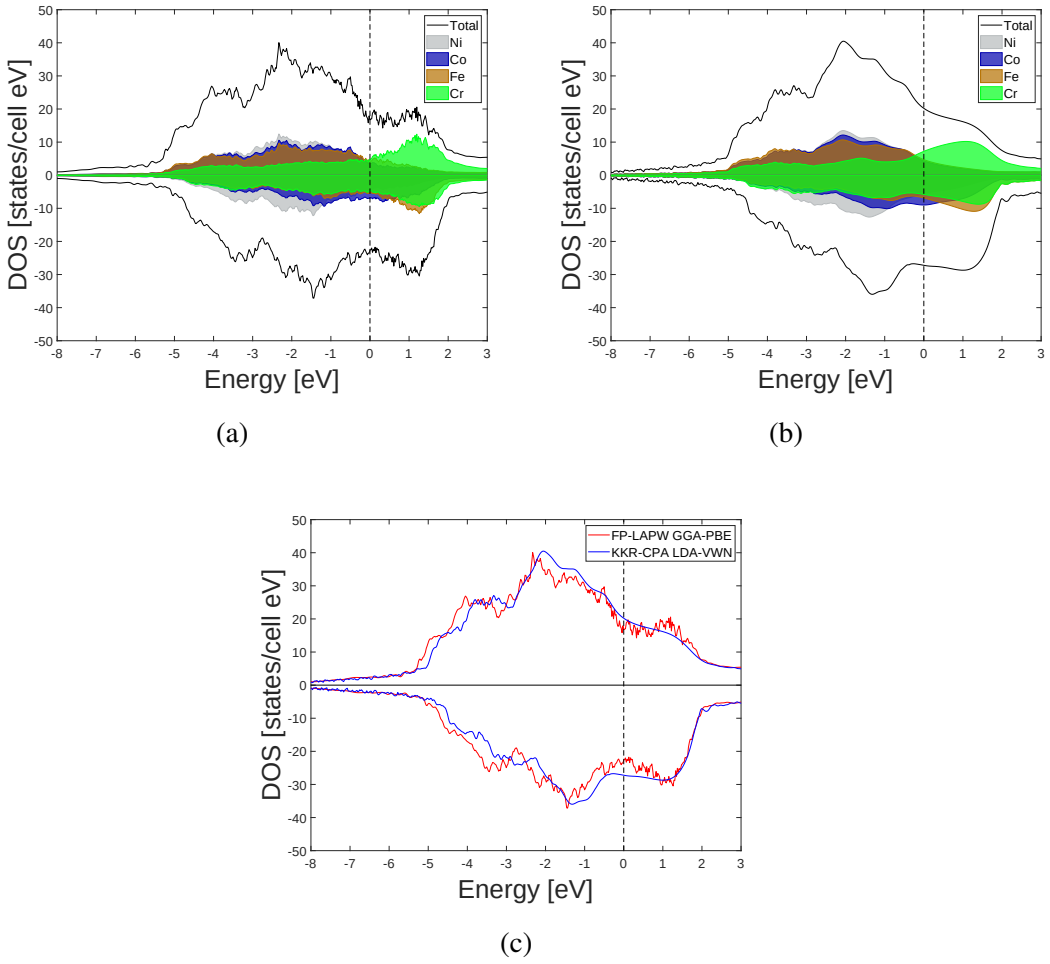

Figure 5.4: DOS and PDOS of NiFeCoCr HEA (a) obtained from a SQS of 32 atoms, (b) calculated with the KKR-CPA method and (c) SQS of 32 atoms and KKR-CPA method.

to the total DOS, ordering from the highest to the lowest contributor were: Cr, Fe, Co and Ni in the majority spin and Co, Fe, Cr and Ni in the minority spin as can be seen from Fig. 5.4a.

Further, the DOS obtained by the KKR-CPA method (Fig. 5.4b) at the Fermi level for the minority spin corresponded to -27.19 states/cell eV and for the majority spin to 20.28 states/cell eV. In both KKR-CPA spin bands, the order of species by PDOS contribution to the total DOS at the Fermi level remains the same as in the SQS method. This order differs from earlier studies done by Tian *et al.* [142, 143] with the EMTO-CPA method. On the other hand, the d character is dominant at the Fermi level in all the species and for both methods.

Fig. 5.4c presents a comparison of the DOS between both theoretical methods. In all figures, FP-LAPW is used to describe all SQS calculations done with the Elk code. There is a slight difference between both densities: below the Fermi level, the band width obtained by the SQS

method is wider than its counterpart calculated with KKR-CPA. The most likely explanation of this discrepancy is because the structural relaxation is present in the SQS method but not in the KKR-CPA method [79]. Actually, the total volume of the SQS was reduced by 6.80% compared with the unrelaxed structure. The magnitude of the displacements of each atom in the relaxed SQS of 32 atoms with respect to their original positions in the unrelaxed structure and the average of the magnitude of the displacements per specie for NiFeCoCr HEA are presented in Table 5.3.

Fig. 5.5c shows the total BSF of NiFeCoCr HEA. The bands are smeared near the Fermi level as is expected owing to the compositional disorder present in the alloy [124]. Also, from Fig. 5.4b it can be seen that the majority spin PDOS of Ni, Co and Fe are overlapping and they have similar width. In contrast, the minority spin PDOS of those elements have different widths and look shifted in relation to their majority spin counterparts. However, for Cr the majority and minority PDOS are slightly shifted and have most of the states over the Fermi level.

These observations support the idea of Mu *et al.* [119] that the intensity of the smearing induced by the chemical disorder can be explained by a relation between the band width and the band centre mismatch between different species. Consequently, the majority spin band (Fig. 5.5a) looks less smeared than the minority spin band (Fig. 5.5b) near the Fermi level where the d character is dominant. This is in good agreement with previous studies of Zhang *et al.* [14] and Mu *et al.* [119].

Unfortunately, reproducing the band smearing for the SQS method is not trivial. In general, a SC is generated stacking a Primitive Cell (PC) along one or more spatial directions. The band structure of a SC may seem somewhat confusing because its BZ is smaller than its PC. Then, interpreting the band structure of the SC in terms of its PC is more meaningful. For this, it is necessary to unfold the band structure of the SC to recover the picture of energy vs. wavevector in the PC. Each atomic position in a SQS may be surrounded by different species which means different local atomic environments. The SQS eigenvalues should be projected on a reference Hamiltonian defined over the correspondent PC [144], for NiFeCoCr HEA the PC corresponds to the FCC structure. Thus, after an unfolding step it would be possible to get the EBS of the alloy.

There are several packages to unfold the band structure of a SC. For instance, Medeiros [145]

Table 5.3: The magnitude of the displacements of each atom in the relaxed SQS of 32 atoms with respect to their original positions in the unrelaxed structure and the average of the magnitude of the displacements per specie for NiFeCoCr HEA.

Atom	Coordinates			$\lvert\Delta r\rvert$
	x (Å)	y (Å)	z (Å)	(Å)
Ni1	0	0	0	0
Ni2	-0.003	4.339	2.336	0.138
Ni3	0.748	2.290	3.545	0.106
Ni4	2.882	1.192	2.935	0.110
Ni5	0.001	-0.754	6.498	0.162
Ni6	2.162	-1.903	5.900	0.164
Ni7	0.728	-2.819	7.682	0.188
Ni8	0.008	2.157	1.170	0.079
Ni Average				0.118
Fe1	2.148	2.505	8.268	0.230
Fe2	0.741	4.416	4.749	0.182
Fe3	-0.681	3.458	6.504	0.205
Fe4	1.472	2.402	5.916	0.154
Fe5	2.139	1.060	0.557	0.089
Fe6	3.569	-0.888	4.146	0.127
Fe7	-1.425	5.466	5.260	0.290
Fe8	0.764	0.067	2.366	0.086
Fe Average				0.170
Co1	1.431	5.317	0.573	0.128
Co2	2.117	5.432	2.968	0.160
Co3	2.869	3.399	4.157	0.115
Co4	0.724	-0.678	8.890	0.199
Co5	2.849	-1.724	8.313	0.179
Co6	1.459	4.484	7.046	0.303
Co7	-0.014	6.490	3.548	0.201
Co8	-0.707	6.411	1.175	0.145
Co Average				0.179
Cr1	-1.395	0.436	9.451	0.250
Cr2	-0.703	1.370	5.318	0.133
Cr3	0.078	1.397	7.713	0.194
Cr4	2.142	0.252	7.085	0.221
Cr5	2.139	3.265	1.727	0.126
Cr6	1.424	0.158	4.653	0.213
Cr7	0.019	3.574	8.840	0.275
Cr8	1.445	7.471	1.825	0.191
Cr Average				0.201

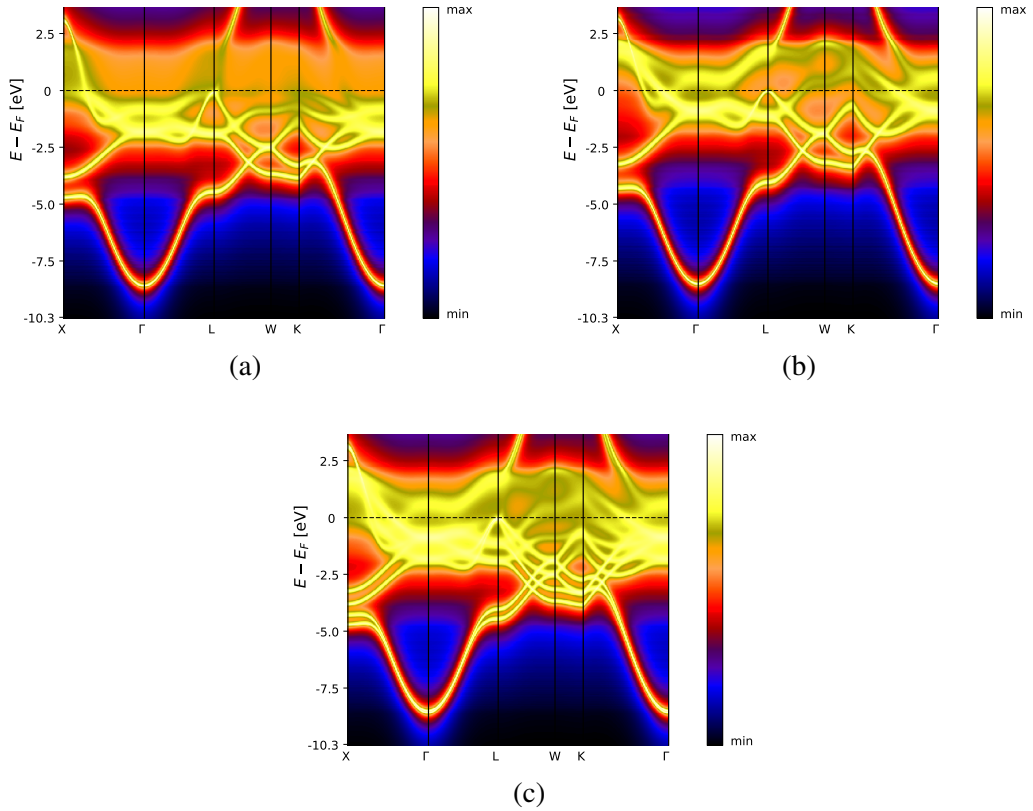

Figure 5.5: BSF of NiFeCoCr HEA of (a) majority spin band, (b) minority spin band and (c) both spin bands calculated with the KKR-CPA method.

developed an unfolding method that is compatible with Quantum Espresso. One disadvantage is that his code, *Band Up*, only works with non-spin polarised calculations. Further work beyond the scope of this thesis, needs to be done to adapt *Band Up* for spin polarised calculations.

5.4 Magnetic Compton Scattering Results

The Elk code uses Eq. 3.76 to calculate the MCP and it is therefore necessary to specify the scattering vector p_z where the MDME will be projected. ATAT can generate SQS with different Bravais lattices i.e. FCC, BCC, HCP, etc. Therefore, it is necessary to know the orientation of the lattice vectors of the SQS relative to their counterparts in the PC. For this purpose, a powder XRD spectra of the SQS was obtained with the help of software such as VESTA [146] or PowderCell [147]. For a cubic system, the Miller indexes of the planes (*h k l*) are the same as their respective perpendicular directions [*h k l*] [148]. Then, the resulting theoretical spectra was

compared with experimental data of Lui *et al.* [122] to determine the peaks and its associated Miller indexes. Thus, it was possible to define a coordinate system for the FCC lattice embedded into the SQS. Then, through a rotation matrix the lattice vectors of the SQS were associated with those of the FCC sublattice. In this way, the scattering vector was defined to get the MCPs.

Fig. 5.6 depicts the MCPs of NiFeCoCr HEA along the main three high symmetry directions [1 0 0] (Fig. 5.6a), [1 1 0] (Fig. 5.6b) and [1 1 1] (Fig. 5.6c). They are normalised to the experimental value of the spin magnetic moment measured by our group and convoluted to the experimental resolution. At first glance the shape of the MCPs is well reproduced by both theoretical methods, especially for the [1 1 1] and [1 1 0] directions along all the momentum scale. However, in the low momentum region from 0 a.u. to 0.5 a.u. the theoretical values of J_{mag} in the [1 0 0] direction are overestimated.

Also, between 0.5 a.u. and 2.2 a.u. both theoretical methods overestimate the value of J_{mag} in all the high symmetry directions. The insets in Fig. 5.6 help to identify the differences between theory and experiment: ΔJ_{mag}. One and the other theoretical method present similar performance in reproducing the MCPs along all the momentum axis. The differences in this region can be explained because the LDA and GGA approximations are based on properties of the uniform electron gas at densities that occur in solids. These approximations describe the magnetism at the Stoner level. Then, they neglect the spin fluctuations at these densities and ignore the magnetic instabilities [149].

Further, in the high momentum region ($p_z > 2.2$ a.u.) the theoretical values of J_{mag} fit relatively well with the experimental ones. This is important because in the IA the Hartree-Fock profile must reproduce the MCPs in this region [150].

In general, for the SQS method the values of $|\Delta J_{mag}|$ shown in the insets of Fig. 5.6 are slightly higher than their counterparts for the KKR-CPA method. Nevertheless, they have an identical trend along all the momentum axis. It seems to be that KKR-CPA does a satisfactory representation of the magnetism in HEA regardless of the fact that the spin magnetic moments of the species are a single-site approximation. In contrast, in real alloys the spin magnetic moments of each atom can take a plethora of values [151], then the SQS method can capture this as is shown in Fig. 5.2b.

Note the magnitude of the error bars in the experimental data along the [1 1 0] direction. The

reason for this was that two data sets were not considered during the data analysis [O'Neill D. (private communication)]. It is recommended to measure again this direction to improve the quality of the results.

The differences between pairs of high symmetry directions or anisotropies can be found in

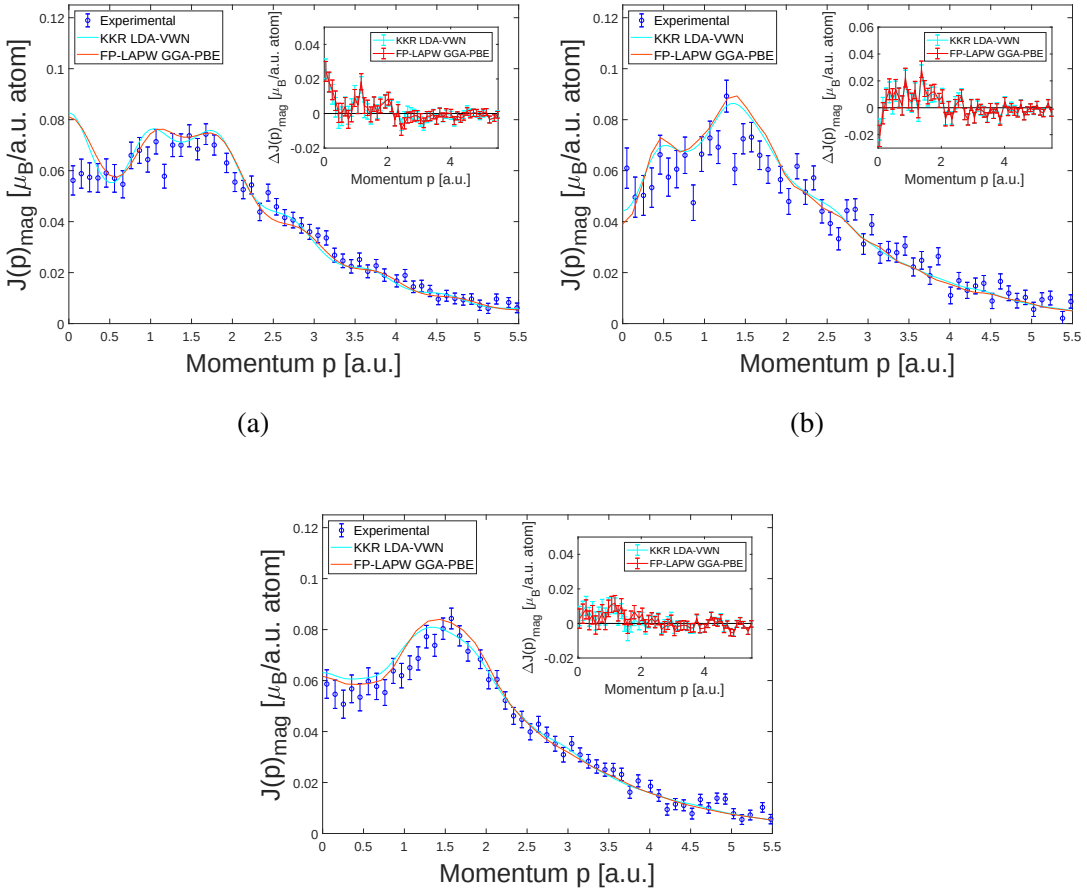

Figure 5.6: MCPs of NiFeCoCr HEA calculated with a SQS of 32 atoms (red) and KKR-CPA method (cyan) compared with experimental measurements (blue) along (a) [1 0 0], (b) [1 1 0] and (c) [1 1 1] directions. The insets show the difference between the theoretical and the experimental measurements.

Fig. 5.7. One of the advantages of analysing the anisotropies is the cancellation of systematic errors in experimental and theoretical methods such as multiple scattering corrections and the isotropic contribution of core electrons respectively [152, 153]. Despite the high error present in the [1 1 0] direction which makes difficult to visualize a trend in Figs. 5.7a and 5.7c, it is still possible to identify some coincidences between peaks and valleys in the low momentum

region of Fig 5.7b between 0.5 a.u. and 2.2 a.u.. However, the theoretical values of ΔJ_{mag} for both methods look clearly overestimated in this region, and this is a well known effect present in 3d transition metals because the theory only considers the homogeneous electron gas correlation [154].

Additionally, the theoretical ΔJ_{mag} values are close to zero in the high momentum region but the experimental values of ΔJ_{mag} are not negligible, and they are oscillating through the momentum axis as can be seen from Fig. 5.7. This theoretical result means that there are not enough high momentum components in the electron wave functions [154]. In other words, there is not enough states with d-character over the Fermi energy. For a better description of 3d transition metals the electrons of occupied states below the Fermi energy should be transferred to the unoccupied states above the Fermi due to correlation effects [155, 156].

Inevitably, there are some discrepancies between the experimental and theoretical anisotropies. It would seem that the correlation is beyond the LDA and GGA approximations. Based on Fig. 5.7, the experimental MCPs are much more isotropic than theory suggests.

The NiFeCoCr HEA MCPs need to be interpreted with attention. Stripping down the MCPs to its components is not viable. Unlike in Ni or Fe where it is enough with six bands to analyse the MCPs, in a SQS calculation there are hundreds of bands and doing this procedure is unpractical. Then, one alternative is comparing the MCPs of NiFeCoCr HEA with Ni MCPs as shown in Fig. 5.8. This is reasonable since Ni is the only ferromagnetic component of the HEA with a FCC structure. The MCPs were normalised to one for their comparison. Like in Ni, the Umklapp contributions to the MCPs are present in the theoretical and experimental MCPs of NiFeCoCr HEA. Figs. 5.8a and 5.8b clearly illustrate the Umklapp processes attributed to contributions of high BZs to the MDME via the reciprocal lattice vector $\mathbf{G}$. Nevertheless, the Umklapp peaks almost disappear in the [1 1 1] direction (Fig. 5.8c) for the SQS calculation.

Furthermore, the theoretical MCPs of NiFeCoCr HEA are less than or equal to their Ni analogous in the low momentum region between 0.5 a.u. and 2.2 a.u.. This would appear to indicate that the d electrons of the 3d transition metals are more delocalised than d electrons in pure Ni. It is well known that itinerant d electrons are the responsible for the magnetic properties in transition metals [83, 34]. Also, in the [1 0 0] direction, J_{mag} of NiFeCoCr takes an opposite trend compared to Ni between 0 a.u. and 0.5 a.u.. The most likely explanation of this difference

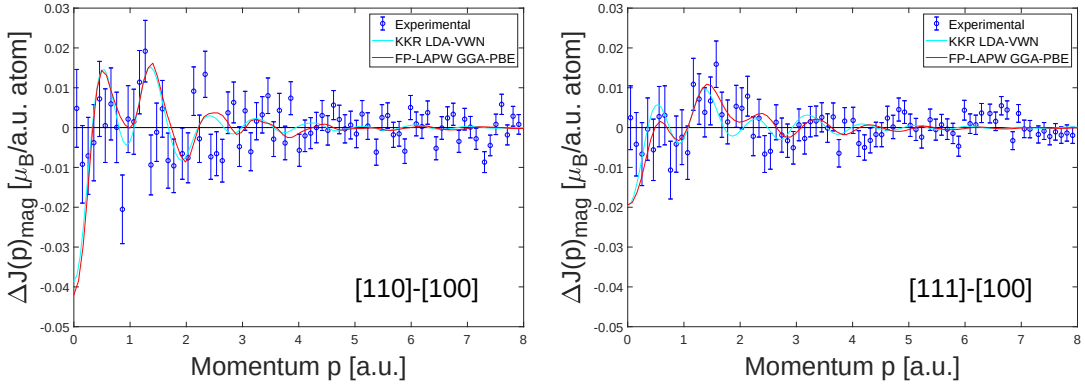

(a)

(b)

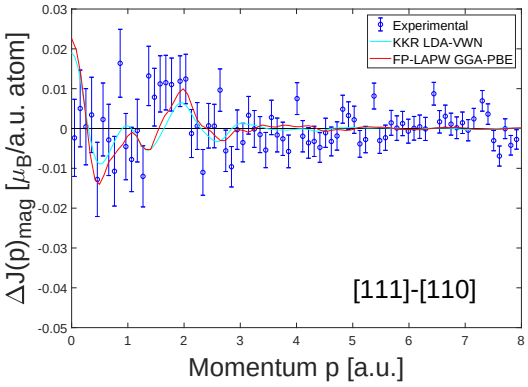

(c)

Figure 5.7: Directional differences in MCPs of NiFeCoCr HEA calculated with a SQS of 32 atoms (red) and KKR-CPA method (cyan) and experimental data (blue): (a) [1 1 0]-[1 0 0], (b) [1 1 1]-[1 0 0] and (c) [1 1 1]-[1 1 0].

is that the contribution to the theoretical MCP of NiFeCoCr due to the bands with p and d character are stronger than those with s character in that interval [90].

The MDME projected on the plane (1 0 0) for the KKR-CPA and SQS method are given in Fig. 5.9. Qualitatively, the MDMEs obtained with both methods look similar: At Γ, the centre of the first BZ, a positive peak is present.

Additionally, along the [0 0 1] or [0 1 0] axis is easy to identify four positive peaks which are the Umklapp contributions of the Γ point in the centres of the neighbouring first BZs. Next, a negative peak is placed near each one of the four K points in the central first BZ.

Following the [0 1 1] and [0 $\bar{1}$ 1] directions, there are two positive peaks near the W points of its surrounding first BZs. They correspond to Umklapp contributions of the X points in the central

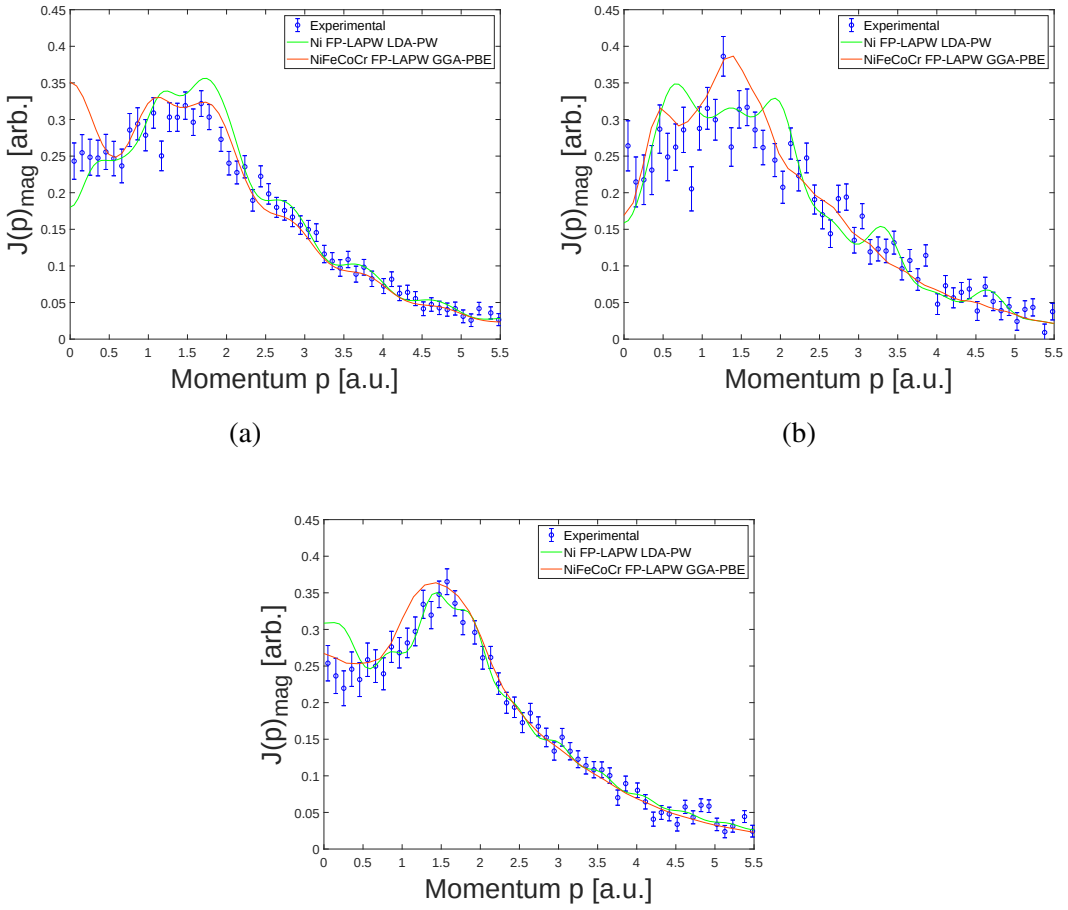

Figure 5.8: Theoretical MCPs of NiFeCoCr HEA from a SQS of 32 atoms (red) and Ni (green) and experimental MCPs of NiFeCoCr HEA (blue) along (a) [1 0 0], (b) [1 1 0] and (c) [1 1 1] directions.

first BZ.

Fig. 5.10 illustrates the MDME of NiFeCoCr HEA projected on the plane (1 1 0) with the KKR-CPA and the SQS method. As in Fig. 5.9, these MDME projections with both theoretical methods look almost identical: In the central first BZ, there are a couple of positive peaks along the [0 0 1] axis. Also, between L and U points there are four negative peaks. Further, a couple of negative peaks, not so deep as the previous ones, are placed in both K points along the [$\bar{1}$ 1 0] axis.

Following the [0 0 1] axis, in the next first BZs there are a couple of positive peaks between their respective Γ and X points. They are Umklapp additions to the MDME from the positive peaks in the central first BZ. The neighbouring first BZs placed along [$\bar{1}$ 1 1] and [$\bar{1}$ $\bar{1}$ 1] directions have

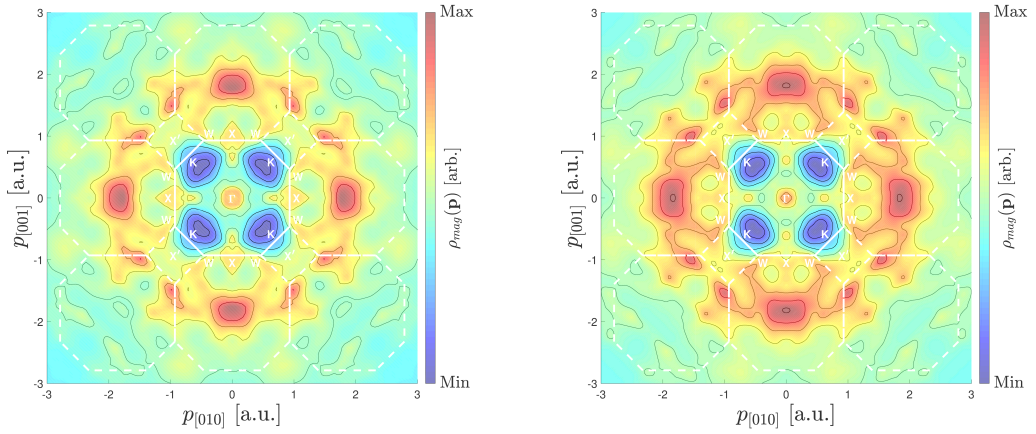

(a) (b)

Figure 5.9: Theoretical MDMEs of (100) NiFeCoCr HEA with (a) KKR-CPA method and (b) a SQS of 32 atoms. White lines are the first BZ boundary and high symmetry points are labelled with white letters.

a couple of positive peaks each one. They are along the segments $\overline{LU}$ in the neighbouring first BZs which are parallel to the segments $\overline{ULK}$ of the central first BZ. Their shapes suggest that they are Umklapp contributions owe to the geometry of the first BZ.

However, in the KKR-CPA more and higher peaks are located along these directions compared to the SQS method. This factor may be responsible for the absence of well defined Umklapp peaks in the SQS MCP along [1 1 1] direction.

On the other hand, the negative peaks in the central first BZ of Figs. 5.9 and 5.10 can be related to delocalised s and d electrons of Cr due to the configuration of its spin moments.

Consider Fig. 5.11, which plots the NiFeCoCr MCPs of the SQS of 72 atoms compared to their counterparts of the SQS of 32 atoms. The semi-core states were removed to get the MCPs of the SQS of 72 atoms. The MCPs along [1 0 0] (Fig. 5.11a) and [1 1 0] (Fig. 5.11b) present similar behaviour to the MCPs of the SQS of 32 atoms. In the low momentum region the values of J_{mag} for the SQS of 72 atoms are higher than J_{mag} for the SQS of 32 atoms. The inverse trend affects J_{mag} in the high momentum region. However, no significant difference was found in the [1 1 1] direction (Fig. 5.11c). It is recommended that further research need to be done to achieve convergence in the shape of MCPs increasing the number of atoms of the SQS.

The most important limitation of calculating the MDME in bigger SQSs is the amount of Random Access Memory (RAM) needed to perform this task. For instance, the calculation of

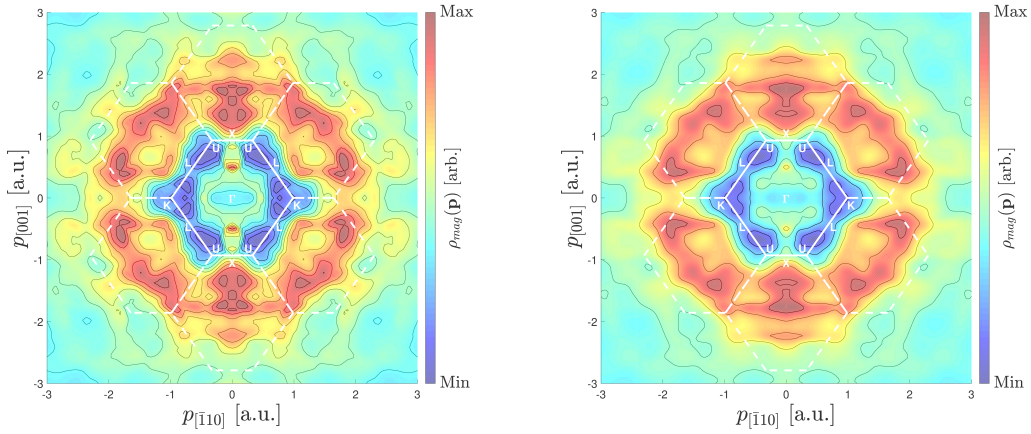

(a) (b)

Figure 5.10: Theoretical MDMEs of (110) NiFeCoCr HEA with (a) KKR-CPA method and (b) a SQS of 32 atoms. White lines are the first BZ boundary and high symmetry points are labelled with white letters.

the MDME for a SQS of 72 atoms required 500 GB of RAM per node. These findings suggest that the SQS of 32 atoms is good enough to describe the theoretical MCPs of NiFeCoCr HEA.

The effects of relaxation in the MDME of NiFeCoCr HEA can be seen in Fig. 5.12. The MDME projection over the (100) plane for the unrelaxed SQS of 72 atoms (Fig. 5.12a) shows a more pronounced positive peak than in the relaxed SQS (Fig. 5.12b) at the Γ point of the central first BZ. The same behaviour is observed in the Umklapp positive peaks in the surrounding first BZs. Also, the negative peaks located near the K points in the unrelaxed SQS look deeper than in the relaxed SQS. Therefore, it may be assumed that the relaxation leaks the MDME from these accumulation points to other regions of the first BZ or higher BZs.

Also, as was mentioned above the KKR-CPA method neglects the structural relaxation. Then, some differences in the projected MDMEs between both theoretical methods would be related to this fact.

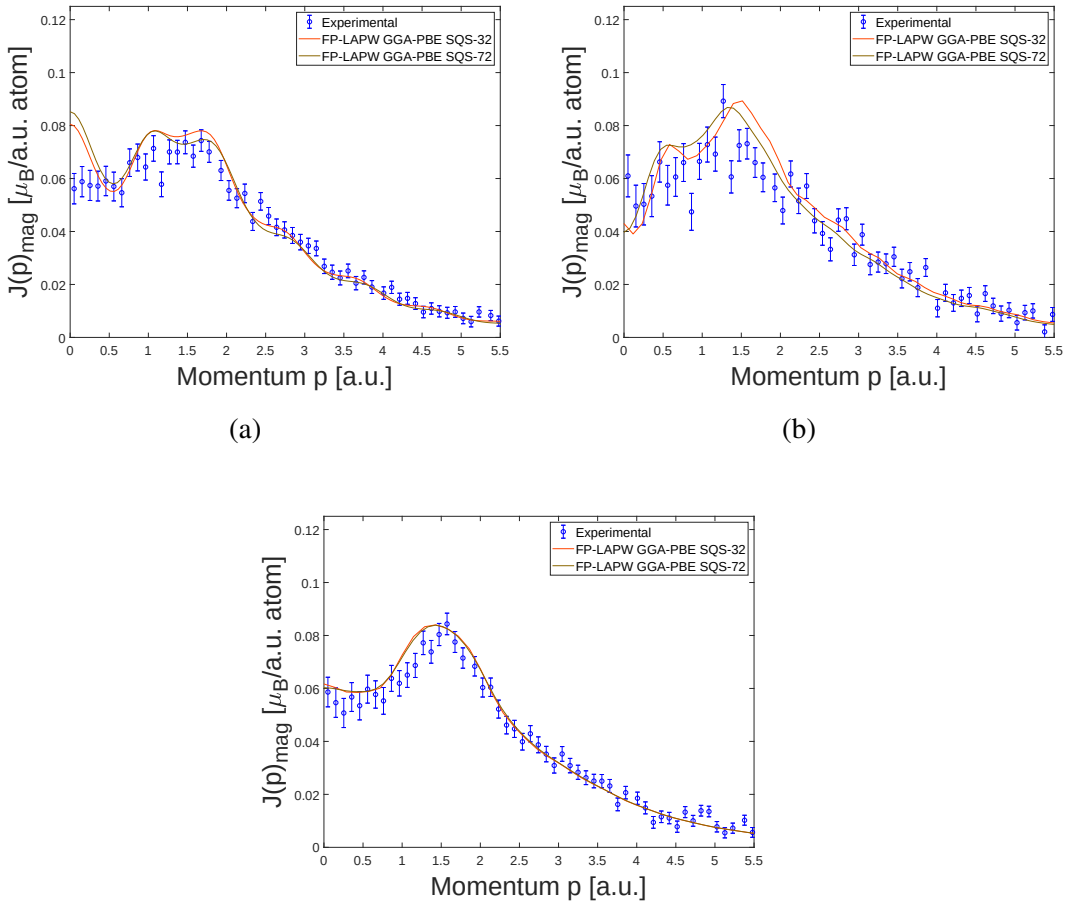

Figure 5.11: MCPs of NiFeCoCr HEA calculated with SQSs of 32 atoms (red) and 72 atoms (brown) compared with experimental data (blue) along (a) [1 0 0], (b) [1 1 0] and (c) [1 1 1] directions.

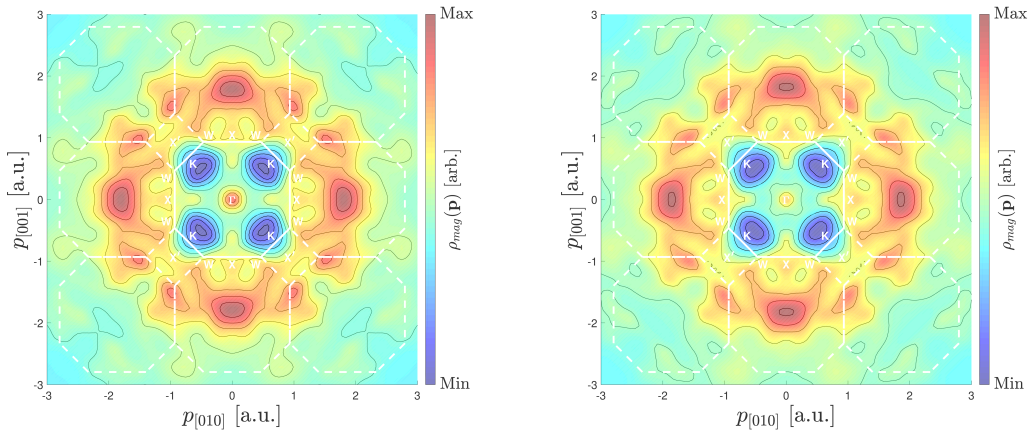

(a) (b)

Figure 5.12: Theoretical MDMEs of (100) NiFeCoCr HEA with (a) a unrelaxed SQS of 72 atoms and (b) its relaxed version.

5.5 Does a Cr sublattice exist in NiFeCoCr HEA?

There are a couple of theoretical studies done by Niu *et al.* [133] and Middleburgh *et al.* [130] suggesting the feasibility of short range order in NiFeCoCr HEA. The antiferromagnetic nature of Cr makes this element the perfect candidate to form a sublattice or cluster with the objective to reduce the total energy of the alloy. The interaction of the magnetic moment of Cr with the moments of its ferromagnetic neighbours (Fe, Ni and Co) impedes the antiferromagnetic coupling of Cr. Thus, Cr atoms prefer to be located outside the first nearest neighbours shell to avoid the repulsion and align their magnetic moments in the opposite direction to the ferromagnetic species [133].

Also, the migration of Cr is the most likely due to its migration activation energy being the lowest followed by Co, Fe and Ni. In this way, a Cr stabilisation or trapping may be possible in the structure of the NiFeCoCr HEA [130].

In this section, a supercell of NiFeCoCr of 32 atoms with the $L2_1$ structure (Fig. 5.13a) was created by the ATAT package in order to investigate Cr clustering from the MDME perspective. Cr atoms occupied the central position of the cubes and the other atoms were randomly placed in the other available positions. The lattice parameter selected was a=3.58 Å [129]. The structural relaxation of the SQS with $L2_1$ structure was done in the Quantum Espresso package with the BFGS algorithm using a US PP with the GGA-PBE approximation for the exchange-correlation functional [76]. The convergence was achieved with 20 **k**-points in the IBZ equivalent to a **k**-point mesh of $8 \times 2 \times 2$. The wave-function and charge-density cut-offs were 75 Ry and 750 Ry respectively. After that, a spin polarised calculation with the GGA-PBE [68] approximation for the exchange-correlation functional was done using the Elk code with an APW+lo basis. The calculation with this SQS converged on 256 **k**-points within the IBZ equivalent to a **k**-point mesh of $16 \times 4 \times 4$. The cut-off for plane waves in the interstitial region defined by $|\mathbf{G}+\mathbf{k}|_{\mathbf{max}}=7/\bar{r}_{MT}$ where $\bar{r}_{MT}$ is the average muffin-tin radius.

The magnetic structure (Fig. 5.13a) illustrates the magnetic moments of Fe, Co, Ni aligned along the positive direction of the z-axis and all Cr atoms aligned in the opposite direction. The spin magnetic moment for the SQS with $L2_1$ structure was 0.174 μ_B/atom, this value being lower than the spin magnetic moment for the SQS of 32 and 72 atoms previously analysed. The average

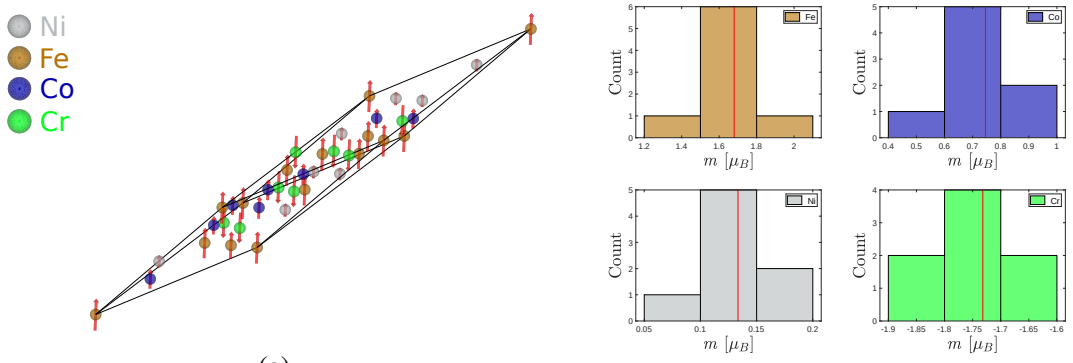

(a) (b)

Figure 5.13: (a) SQS supercell of 32 atoms used to model NiFeCoCr HEA with $L2_1$ structure. The red arrows represent the projection of the spin moment in the z-direction, their magnitude is scaled to the results obtained from the DFT calculations obtained with the Elk code. (b) Histogram of the distribution of atoms of the SQS according to their spin magnetic moment m.

spin moment (red line in Fig. 5.13b) of each species with this SQS is summarised in Table 5.2. As can be seen from Fig. 5.14, J_{mag} in the MCPs of the SQS with $L2_1$ structure along [1 0 0] (Fig. 5.14a), [1 1 0] (Fig. 5.14b) and [1 1 1] (Fig. 5.14c) directions takes negative values in the low momentum region. Also, the shapes of the theoretical MCPs are totally different to their experimental data. This demonstrates just how inaccurate the postulate of Cr clustering is in this alloy due to negative values of J_{mag} have never been observed for a 3d transition metal HEA.

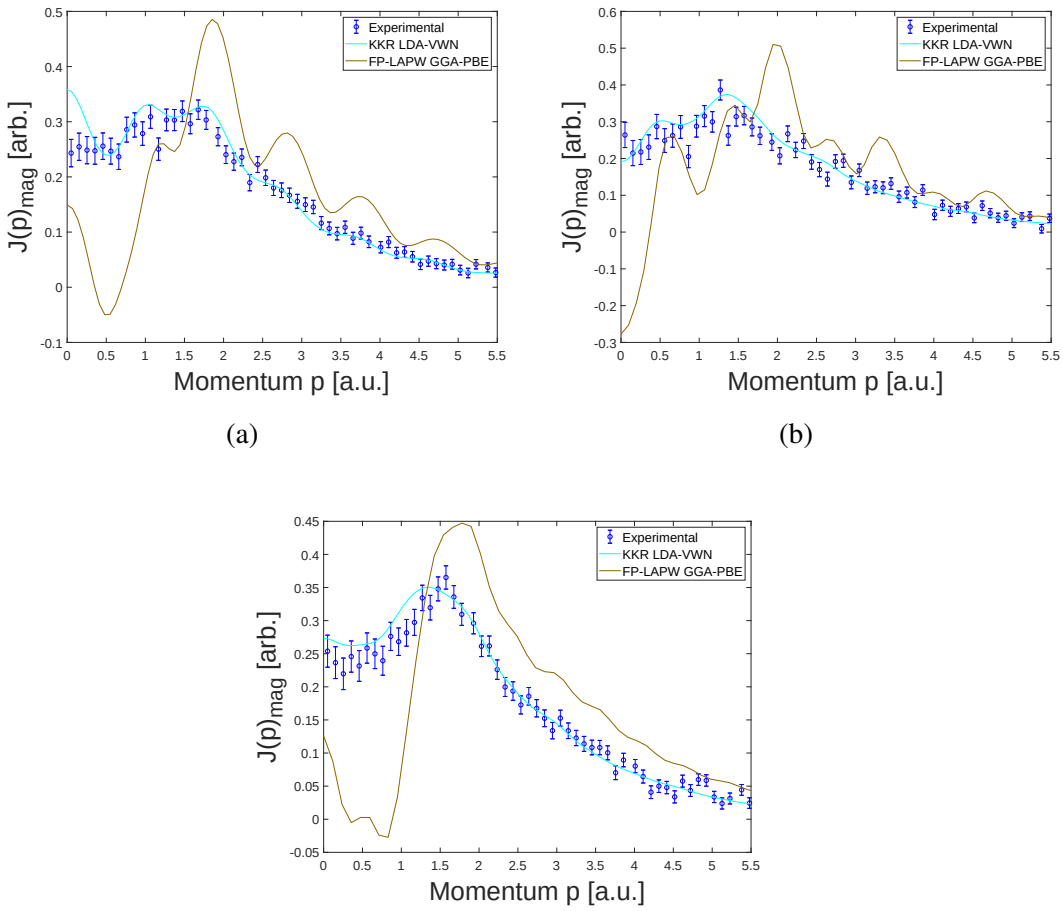

Figure 5.14: MCPs of NiFeCoCr HEA calculated from a SQS of 32 atoms with $L2_1$ structure (gold) and KKR-CPA method (cyan) compared with experimental measurements (blue) along (a) [1 0 0], (b) [1 1 0] and (c) [1 1 1] directions.

5.6 Summary and Conclusions

Traditionally, KKR-CPA method has been the battle horse for simulating disordered alloys because the calculation time is low compared to the SQS method. However, the SQS method presented in this chapter looks to be good approach for modelling the chemical disorder in NiFeCoCr HEA. The values of spin magnetic moment were similar between both methods, but they were higher than the experimental one measured by magnetic Compton scattering. Also, the magnetic structure captured by the SQS method was in agreement with the magnetic structure of the XMCD experiments done by our group.

The MCPs calculated by both theoretical methods had small differences between them in the three high symmetry directions, specially in the low momentum region. In general, the same amount of theoretical points passed through the experimental error bars along all the momentum axis. This implies that their performance in representing the MCPs was equal.

The theoretical anisotropies presented the same number of peaks and valleys. However, there were small differences in their amplitude in the low momentum region between them. Given that the experimental MCP along the [1 1 0] direction had bigger error bars due to two data sets were not combined, this direction needs to be measured again. However, from the difference between the [1 1 1] and [1 0 0] directions, the theoretical and the experimental anisotropies followed the same trend between 0.5 a.u. and 2.2 a.u.. Outside this interval there were discrepancies between theory and experiment.

The MDME projected on (1 0 0) and (1 1 0) planes shown many resemblances between both methods. The negative peaks located near the K points of the central first BZ in the (1 0 0) projection and those around the boundary of the central first BZ in the (1 1 0) projection can be related to delocalised s and d electrons of Cr.

Relaxation effects of the SQS were analysed in the SQS of 72 atoms. The peaks in the MDME were more pronounced in the unrelaxed version than in the relaxed version. This is related with the change of volume in the SQS because if the volume in the direct space is compressed the opposite happens in the reciprocal space. Hence, the KKR-CPA calculations neglect structural relaxation, some differences in intensity and concentration of the MDME with the SQS method can be explained by this reason.

In summary, the disagreements found between the theoretical MCPs and anisotropies against the experimental data can be attributed to the electron correlations are beyond LDA and GGA. It seems to be that the one-electron wave function and the exchange-correlation functional derived from it are not the most optimal models to capture the complexity of the MDME of the NiFeCoCr HEA. However, some insight has been gained with the regard to the magnetisation of this compound.

Furthermore, previous works speculated about Cr clustering in NiFeCoCr HEA. Studying this issue from the MDME perspective suggest that a Cr clustering like in the $L2_1$ structure did not produce reliable MCPs.

Chapter 6

The Electronic Structure and Magnetisation of NiFeCoCrPd HEA

As was mentioned in the previous chapter, Pd was the missing piece needed to generate a new set of alloys from the 3d transition metals found in the Cantor alloy NiFeCoCrMn. Pd is a 4d transition metal in the same group of the periodic table as Ni. Pd has a bigger mass than 3d transition metals. Also, it is a strongly enhanced paramagnet in its ground state.

In the present chapter, the effect in the magnetism due to the addition of Pd to NiFeCoCr HEA is going to be discussed. This new equiatomic HEA will be characterised experimentally by magnetic Compton scattering. The aim is to study the electronic structure of NiFeCoCrPd and to understand the magnetisation from its MDME projections.

6.1 Pd a 4d transition metal

Pd presents a FCC structure at ambient pressure. This 4d transition metal has a band structure similar to 3d transition metals [157]. Also, the number of valence electrons in Pd is equal to Ni. On the basis of above, Pd may be a ferromagnet but this is not the case.

The 4d electron wave function extends more in the direct space than the 3d wave function. Thus, the correlations between electrons are smaller in Pd than Ni. Also, Pd has a larger lattice parameter than Ni unit cell. Then, the DOS at Fermi energy of Pd is smaller than Ni [157]. Therefore, the Stoner criterion for ferromagnetism is not satisfied by Pd.

The d bands in Pd are broader and higher-lying than in noble metals. The number of electrons per atom is smaller, thus the Fermi level crosses the d bands [30]. For this reason, its Fermi surface is more complex than in noble metals. Indeed, the Fermi surface of Pd contains three sheets [158].

On the other hand, spin polarised calculations has shown that Pd can reach a ferromagnetic state when the lattice parameter is increased by 5% to 6% [158]. This is because the magnetism in Pd is related to the degree of s-d hybridisation which usually depends on the lattice constant.

Additionally, Pd has an uniform paramagnetic spin susceptibility. Also, the temperature dependence of the susceptibility shows effects of long-lived spin fluctuations or paramagnons [159].

It has been found that the addition of Pd to NiFeCoCr HEA increases its magnetic moment and Curie temperature [132]. Thus, the resultant NiFeCoCrPd HEA may be useful for magnetic refrigeration applications near room temperature.

6.2 Equiatomic NiFeCoCrPd HEA

NiFeCoCrPd HEA is a material that presents configurational disorder in the bulk. APT has proved that there is not clustering or short-range order of its atoms but on the surface of the crystal sample was found some Pd accumulation by sedimentation [128]. However, this last fact does not affect our results because magnetic Compton scattering is a bulk probe. Also, Energy Dispersive X-ray (EDX) spectroscopy shows a uniform distribution of the constituent

elements [140].

At room temperature it is ferromagnetic, the following values of Curie temperature T_C has been reported: 440 K [132] and 374 K [33]. Their constituent atoms are placed in a FCC structure as X-ray [129, 160, 161] and neutron [129, 160] diffraction experiments have shown. The lattice parameter of this HEA is a=3.65 Å [132]. The saturation magnetisation: 0.39 μ_B/atom with a sample prepared by arc melting using 96.06% Fe and pure Co, Cr and Ni [132] or 0.52 μ_B/atom with a sample prepared arc melting with the appropriate amounts of pure Ni, Fe, Co and Cr [33]. DFT calculations shown that the magnetic moment of Fe, Ni, Co and Pd have their magnetic moments aligned ferromagnetically and Cr is aligned in the opposite direction, this coupling of the magnetic moments of Cr can be present in every Cr atom as was examined by Mu *et al.* [151] or in most of them as described by Calvo-Dahlborg *et al.* [134]. There is also experimental evidence of this magnetic structure in XMCD experiments done by our group [135].

The single crystal sample used in the magnetic Compton scattering experiments was prepared by arc melting Pd, Ni, Fe, Co and Cr in a water-cooled copper hearth, under an Ar atmosphere [125] with approximate dimensions of $3\times3\times2$ mm. The bulk magnetic moment measured on a SQUID was 0.541 μ_B/atom. The spin magnetic moment obtained by magnetic Compton scattering was 0.474 μ_B/atom. Therefore, the orbital magnetic moment corresponds to 0.067 μ_B/atom.

The thermal conductivity at 50 K is 4.2 $Wm^{-1}K^{-1}$, meanwhile at 300 K is 10.3 $Wm^{-1}K^{-1}$ [33]. The experimental residual resistivity is 126.6 $\mu\Omega$cm [33], meanwhile its theoretical counterpart is 124.8 $\mu\Omega$cm [119]. These values are close to the Mott-Ioffe-Regel (MIR) limit, which is characterised by a value of the electron mean free path (λ_e) being comparable to the lattice spacing. Whereas, the experimental electrical resistivity at 300 K is 134 $\mu\Omega$cm [33].

The understanding of electronic transport and magnetic properties is important to know the possible practical applications of this alloy. For this reason, in the next sections the electronic structure and the magnetisation of NiFeCoCrPd will be studied.

6.3 Electronic Structure Calculations on NiFeCoCrPd HEA

In order to understand the effect of adding Pd to a NiFeCoCr HEA matrix, NiFeCoCrPd was simulated using the KKR-CPA and the SQS methods.

The KKR-CPA calculations using the LDA-VWN as exchange-correlation functional of NiFeCoCrPd was supplied by S. B. Dugdale. Also, a supercell of NiFeCoCrPd with 35 atoms (Fig. 6.1a) was created by the ATAT package with a lattice parameter a=3.65 Å [129]. The structural relaxation of the SQS of 35 atoms was done in the Quantum Espresso package with the BFGS algorithm using a US PP with the GGA-PBE approximation for the exchange-correlation functional [76]. The convergence was achieved with 20 **k**-points in the IBZ equivalent to a **k**-point mesh of $4 \times 4 \times 2$. The wave-function and charge-density cut-offs were 75 Ry and 750 Ry, respectively. After that, a spin polarised calculation with the GGA-PBE [68] approximation for the exchange-correlation functional was done using the Elk code with an APW+lo basis. The calculation with the SQS of 35 atoms was converged on 245 **k**-points within the IBZ equivalent to a **k**-point mesh of $7 \times 7 \times 5$. The cut-off for plane waves in the interstitial region defined by $|\mathbf{G}+\mathbf{k}|_{\mathbf{max}}=7/\bar{r}_{MT}$ where $\bar{r}_{MT}$ is the average muffin-tin radius.

The spin magnetic moment is 0.555 μ_B/atom for the SQS of 35 atoms, whereas the spin magnetic moment obtained from the KKR-CPA calculation is 0.676 μ_B/atom and the magnetic orbital moment is 0.033 μ_B/atom. This magnetic orbital moment corresponds to 4.65% of the total magnetic moment in the KKR-CPA method. For the same reasons mentioned in the previous chapter, it was decided not consider the SOC for the SQS calculations.

Fig. 6.1a shows the magnetic structure of NiFeCoCrPd HEA where the spin moments of Ni, Fe, Co, Pd atoms are aligned in the same direction but Cr present both spin directions along the z-axis with most of its spin moments aligned in a direction opposed to the former elements. This magnetic structure is in agreement with a previous work by Calvo-Dahlborg *et al.* [134].

The average spin moment (red line in Fig. 6.1b) for each species with the SQS method, KKR-CPA calculations and XMCD measurements are summarised in Table 6.1.

The spin magnetic moment in the KKR-CPA method is bigger than in the SQS method. However,

Table 6.1: The spin magnetic moments of NiFeCoCrPd HEA from the SQS of 35 atoms, KKR-CPA calculations and XMCD measurements. The average m^{spin} from the sum-rules were determined using their respective Pd d-moments from the KKR calculations and are indicated by asterisks.

Alloy	Species	SQS-35 atoms	KKR-CPA	XMCD
		m^{spin} (μ_B)	m^{spin} (μ_B)	$m_z^{spin,eff}$ (μ_B)
NiFeCoCrPd	Ni	0.374	0.423	0.606
	Fe	2.232	2.430	2.346
	Co	1.164	1.486	1.644
	Cr	-0.958	-1.061	-1.087
	Pd	0.086	0.104	0.139*
NiFeCoCrPd	Average	0.555	0.676	0.730*

the value in the SQS method is the closest to the experimental one measured by magnetic Compton scattering. On the other hand, the theoretical and experimental values of spin magnetic moment values are bigger than their analogues of NiFeCoCr. This finding confirms that the addition of Pd in NiFeCoCr HEA increases its total magnetic moment due to changes in the lattice parameter. The lattice parameter is affected by the local atomic arrangement and this fact has a significant effect on magnetic interactions [134].

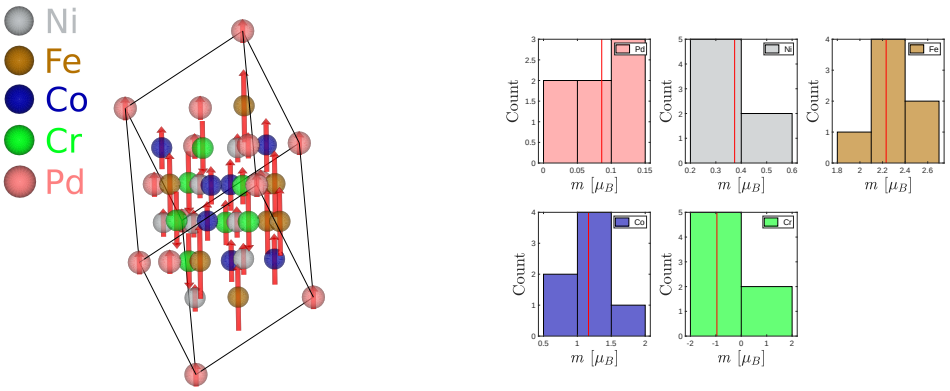

(a) (b)

Figure 6.1: (a) SQS supercell of 35 atoms used to model NiFeCoCrPd HEA. The red arrows represent the projection of the spin moment in the z-direction, their magnitude is scaled to the results obtained from the DFT calculations obtained with the Elk code. (b) Histogram of the distribution of atoms of the SQS according to their spin magnetic moment m.

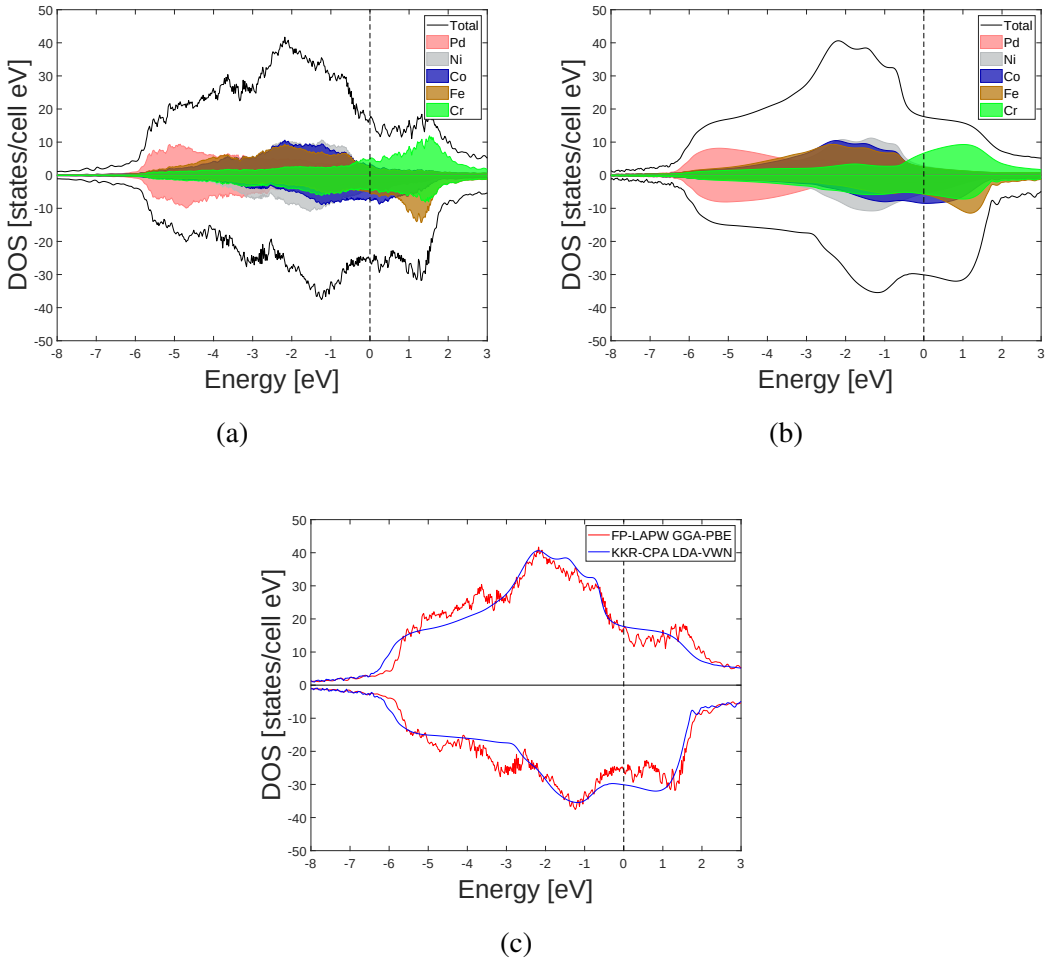

Figure 6.2: DOS and PDOS of NiFeCoCrPd HEA (a) obtained from a SQS of 35 atoms, (b) calculated with the KKR-CPA method and (c) SQS of 35 atoms and KKR-CPA method.

The DOS of NiFeCoCrPd SQS (Fig. 6.2a) at the Fermi level for the minority spin is -25.47 states/eV cell and for the majority spin is 17.13 states/eV cell. The negative sign in the minority spin is only to differentiate from the majority spin but both are positives in reality. At the Fermi level the PDOS contribution to the total DOS, ordering from the highest to the lowest contributor, the following order was obtained: Cr, Co, Fe, Ni and Pd in the majority spin and Co, Fe, Ni, Cr and Pd in the minority spin. Further, the DOS in KKR-CPA (Fig. 6.2b) at the Fermi level for the minority spin is -30.1 states/cell eV and for the majority spin is 17.72 states/cell eV.

Also, at the Fermi level ordering from the highest to the lowest contributor of the PDOS to the total DOS in the KKR-CPA calculation, the following sequence was obtained: Cr, Ni, Fe, Co and Pd for the majority spin and Co, Fe, Cr, Ni and Pd for the minority spin. Additionally, the d character is dominant at the Fermi level in the PDOS for all the species and in both methods.

The discrepancy in the PDOS states contribution between both methods may be associated to a difference in the binding energies considered for each species due to the lattice distortions present in the SQS method [162].

Obviously, the PDOS discrepancy is also reflected in the mismatch of the total DOS (Fig. 6.2c). There is not significant difference of the total DOS of the SQS along the energy axis with exception of the states over the Fermi level. Indeed, the volume of the relaxed structure is 3.92% smaller than its unrelaxed version. Table 6.2 shows the magnitude of the displacements of each atom in the relaxed SQS of 35 atoms with respect to their original positions in the unrelaxed structure and the average of the magnitude of the displacements per specie for NiFeCoCrPd HEA.

It would seem that the atomic mass of Pd, almost twice bigger than the 3d transition metals, minimizes the total DOS differences between a relaxed and an unrelaxed structure in the region where most of the filled Pd states are placed. Also, the addition of Pd atoms in a NiFeCoCr HEA increases the lattice parameter and so the 3d transition metals have more free space to move [161]. Thus, the differences in total DOS over the Fermi level are more visible in this region where most of the states belong to the 3d transition metals.

Fig. 6.3c illustrates the total BSF of NiFeCoCrPd HEA. This looks more smeared than the BSF of NiFeCoCr, hence the Pd bands are located far below the Fermi level. Doping a NiFeCoCr HEA with Pd results in an overall increasing of the smearing in the BSF because the atomic size of Pd produces displacement fluctuations [33]. This is an extra source of smearing added to the smearing due to compositional disorder also present in NiFeCoCrPd HEA. The origins and quantification of smearing in the electronic bands due to disorder was already discussed in the previous chapter.

The bands with d character of the 3d transition metals in the minority spin band (Fig. 6.3b) look more smeared and they are crossing the Fermi level. While in the majority band the bands with d character of 3d transition metals (Fig. 6.3a) look smeared as well but they are located bellow the Fermi level. Far below the Fermi level the semi-core s bands were the only ones without smearing. As far as is known, the BSFs of NiFeCoCrPd has been presented here for the first time.

As was mentioned in the previous chapter to get the EBS of a SQS is challenging. Further

Table 6.2: The magnitude of the displacements of each atom in the relaxed SQS of 35 atoms with respect to their original positions in the unrelaxed structure and the average of the magnitude of the displacements per specie for NiFeCoCrPd HEA.

Atom	Coordinates			$\lvert\Delta r\rvert$
	x (Å)	y (Å)	z (Å)	(Å)
Pd1	0	0	0	0
Pd2	7.187	6.761	0.267	0.137
Pd3	7.313	8.448	6.173	0.170
Pd4	5.844	8.174	3.994	0.220
Pd5	3.323	7.427	4.339	0.134
Pd6	8.663	4.553	7.327	0.195
Pd7	2.410	2.593	5.635	0.209
Pd Average				0.152
Ni1	5.285	1.592	3.799	0.245
Ni2	7.701	6.442	4.559	0.231
Ni3	5.315	5.738	4.822	0.118
Ni4	1.945	2.750	1.356	0.045
Ni5	3.805	5.438	2.660	0.181
Ni6	2.931	4.993	4.978	0.161
Ni7	5.741	3.893	3.145	0.168
Ni Average				0.164
Fe1	9.294	6.866	6.734	0.080
Fe2	6.677	4.343	0.947	0.152
Fe3	4.431	5.282	7.093	0.156
Fe4	8.175	4.649	2.914	0.171
Fe5	3.316	3.104	3.303	0.228
Fe6	7.627	2.379	3.533	0.299
Fe7	3.839	1.237	1.739	0.183
Fe Average				0.181
Co1	4.827	7.579	6.500	0.174
Co2	8.605	7.066	2.303	0.181
Co3	6.220	6.191	2.510	0.174
Co4	4.280	3.537	1.072	0.146
Co5	6.225	1.963	1.619	0.118
Co6	6.217	3.711	7.531	0.216
Co7	4.901	3.428	5.475	0.145
Co Average				0.165
Cr1	6.685	1.910	5.850	0.310
Cr2	4.824	5.827	0.479	0.174
Cr3	2.406	5.056	0.652	0.138
Cr4	4.415	7.879	1.982	0.132
Cr5	6.613	6.066	6.909	0.240
Cr6	7.148	4.175	5.156	0.272
Cr7	4.003	2.980	7.800	0.206
Cr Average				0.210

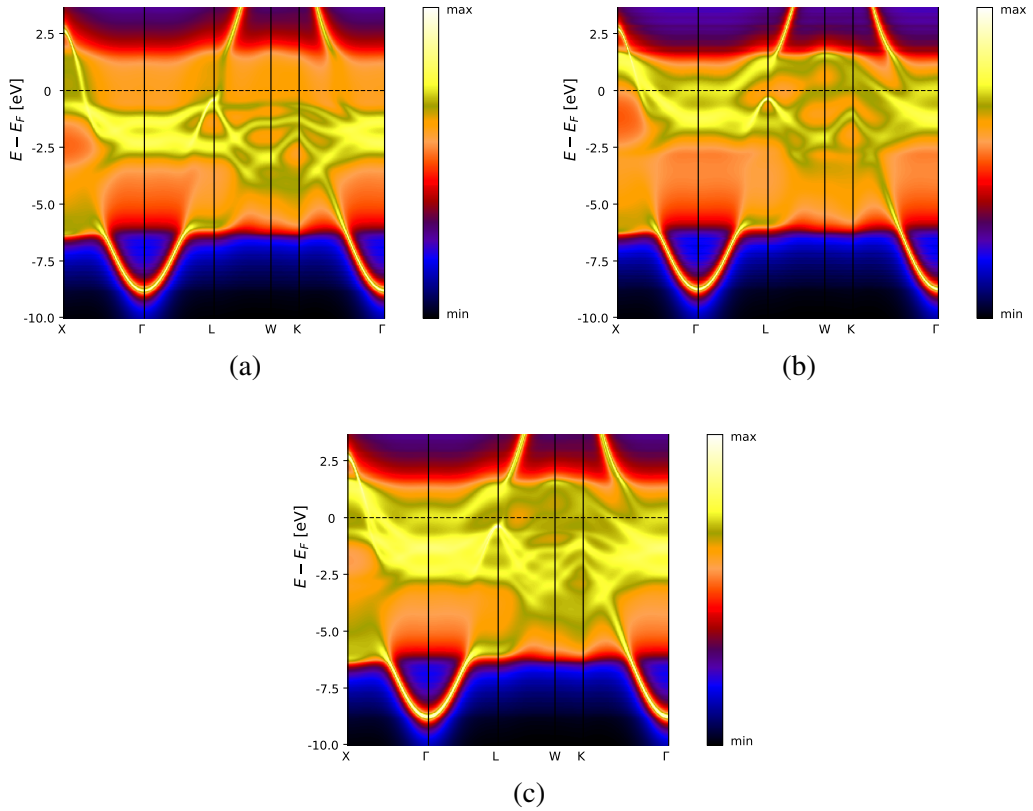

Figure 6.3: BSF of NiFeCoCrPd HEA of (a) majority spin band, (b) minority spin band and (c) both spin bands calculated with the KKR-CPA method.

work beyond the scope of this thesis, needs to be done to adapt unfolding band codes like *Band Up* [145] to Quantum Espresso or even to the Elk code for spin polarised calculations.

6.4 Magnetic Compton Scattering Results

Following the same methods as for the NiFeCoCr HEA, the lattice vectors of the SQS generated with ATAT need to be related with its embedded PC. For NiFeCoCrPd the PC corresponds to the FCC structure as in NiFeCoCr. Then, the powder XRD spectrum of the NiFeCoCrPd SQS was obtained using software like VESTA [146] or PowderCell [147]. After that, the theoretical spectra was compared with the experimental one obtained by Dahlborg *et al.* [129]. The Miller indexes ($h\ k\ l$) of the planes correspond to their respective perpendicular directions [$h\ k\ l$] in a cubic system. Thus, a new reference framework was defined with its origin in the FCC sublattice. Then, the lattice vectors of the SQS and the FCC sublattice can be associated through a rotation

matrix. Thus, the scattering vector p_z needed to get the MCPs was defined.

Fig. 6.4 presents the MCPs of NiFeCoCrPd HEA along the three high symmetry directions

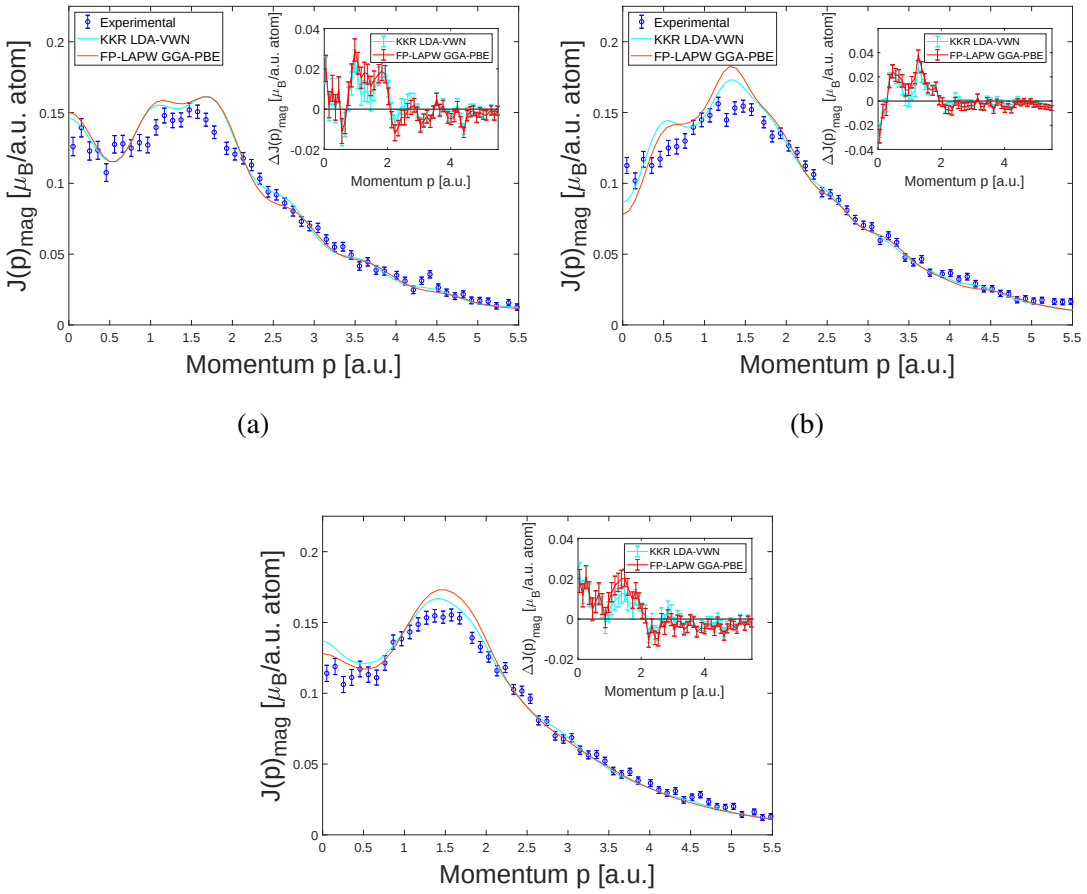

Figure 6.4: MCPs of NiFeCoCrPd HEA calculated with a SQS of 35 atoms (red) and KKR-CPA method (cyan) compared with experimental measurements (blue) along (a) [1 0 0], (b) [1 1 0] and (c) [1 1 1] directions.

[1 0 0] (Fig. 6.4a), [1 1 0] (Fig. 6.4b) and [1 1 1] (Fig. 6.4c). In general, the shape of the experimental MCPs is well reproduced by both theoretical methods along the momentum axis in the three directions. The insets in Fig. 6.4 illustrates the performance of the theoretical methods measuring their difference against the experimental data. Then, $|\Delta J_{mag}|$ with the SQS method is slightly bigger than their counterparts calculated with the KKR-CPA method.

Looking at the momentum region from 0 a.u. to 0.5 a.u., there are some discrepancies between the theoretical values of J_{mag} and the experimental ones. Theoretical J_{mag} in the [1 0 0] and [1 1 1] looks overestimated, meanwhile in the [1 1 0] direction it is underestimated.

Then, from 0.5 a.u. to 2.1 a.u. J_{mag} is overestimated by the theoretical calculations. This is a well known behaviour because the LDA and GGA exchange-correlations functionals have problems describing the behaviour of itinerant electron ferromagnets [149, 163].

Theoretical J_{mag} in the high momentum region matches very well with the experimental data for all the directions. Then, the validity of the IA is corroborated by the experimental and theoretical data. The humps produced by the Umklapp scattering are well represented in the [1 0 0] and [1 1 0] directions. Though, in the [1 1 1] the theoretical MCP did not show any Umklapp peaks in this region.

Fig. 6.5 presents the differences between couples of high symmetry directions or anisotropies.

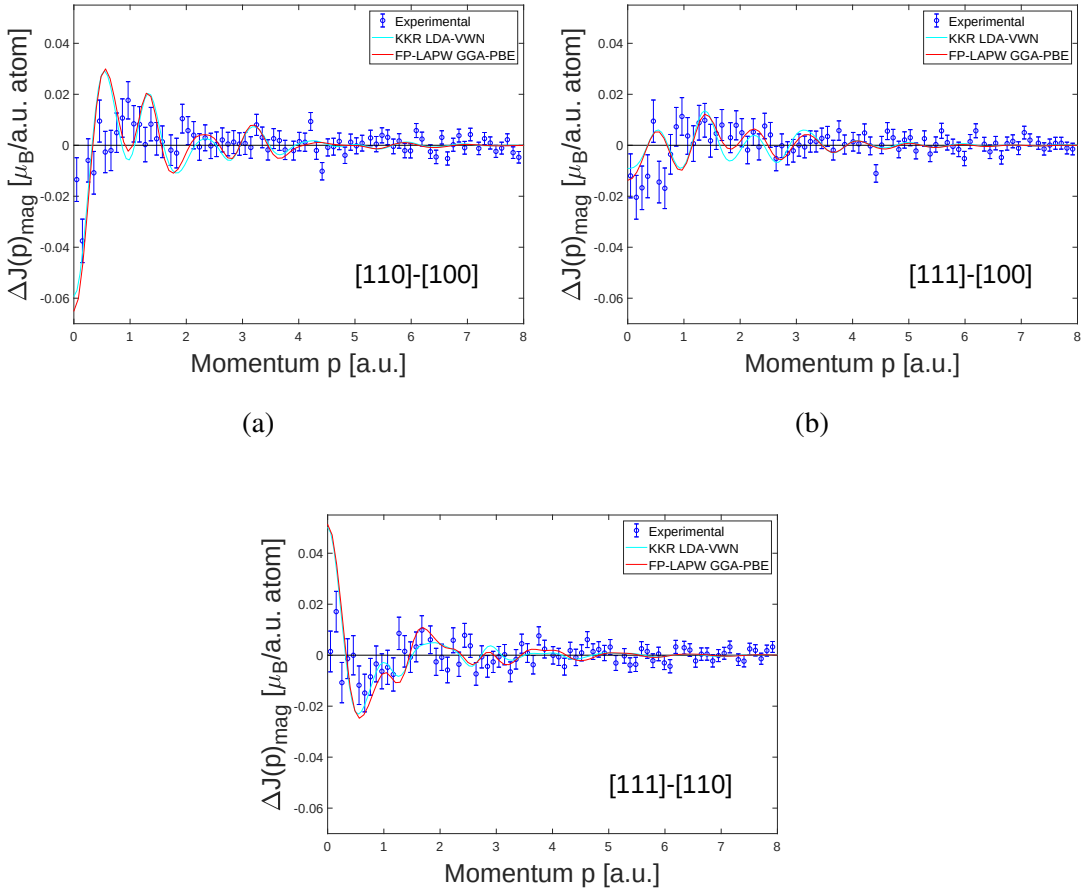

(a) (b)

(c)

Figure 6.5: Directional differences in MCPs of NiFeCoCrPd HEA calculated with a SQS of 35 atoms (red) and KKR-CPA method (cyan) and experimental data (blue): (a) [1 1 0]-[1 0 0], (b) [1 1 1]-[1 0 0] and (c) [1 1 1]-[1 1 0].

In general, there are no significant differences in the anisotropies between the KKR-CPA and

SQS method along all the momentum axis.

In Figs. 6.5a and 6.5c the theoretical ΔJ_{mag} differ slightly from the experiment between 0 a.u. and 0.5 a.u. Nevertheless, in the difference between [1 1 1] and [1 0 0] directions (Fig. 6.5b) the shape is better reproduced in this interval by both theoretical methods. These discrepancies can be explained by the fact that the theory overestimates the values of ΔJ_{mag} near p_z= 0 a.u. [11, 164]. From 0.5 a.u. to 2.1 a.u., the theoretical ΔJ_{mag} are inside the expected error in Fig. 6.5b and Fig. 6.5c. Though, in Fig. 6.5a the theoretical calculations are outside the error bars and present a different trend. For 3d transition metals is well known that in this region the GGA and LDA approximation overestimate the values of ΔJ_{mag} [154].

In the high momentum region ($p_z > 2.1$ a.u.), theoretical ΔJ_{mag} oscillates and decreases until reach an amplitude of zero as is expected in all three high symmetry directions differences, this is illustrated in Fig. 6.5. However, the experimental values of ΔJ_{mag} still oscillate, fortunately they have a small amplitude in this region. Then, many of the theoretical values pass through the experimental error bars.

Given the complex nature of HEA, the interpretation of the MCPs should be treated with attention. As in NiFeCoCr MCPs some insights about MCPs of NiFeCoCrPd can be deduced from the comparison with MCPs of Ni. For this, the MCPs and the experimental data has been normalised to one as shown in Fig. 6.6.

From 0 a.u. and 0.5 a.u., J_{mag} of NiFeCoCrPd in the [1 0 0] direction takes and opposite trend compared to Ni. Next, the MCPs of NiFeCoCrPd look narrower than MCPs of pure Ni in the low momentum region between 0.5 and 2.1 a.u.. It seems to be that the d valence electrons of the transition metals in the HEA alloy are more delocalised than in Ni. This is because the 4d wave function extends more in the direct space than the 3d wave function. Then, there are more overlap between the d wave functions in NiFeCoCrPd HEA.

Also, in the high momentum region of [1 0 0] (Fig. 6.6a) and [1 1 0] (Fig. 6.6b) directions the Umklapp peaks appears as a consequence of the contribution of high BZs via a reciprocal lattice vector **G** but they are not as big as in Ni due to the disorder present in NiFeCoCrPd HEA. As was mentioned above, Umklapp peaks are not visible in the [1 1 1] direction.

The theoretical MDMEs projected over the (1 0 0) plane are shown in Fig. 6.7, both present a similar distribution. A positive peak appears in Γ inside the central first BZ for both methods.

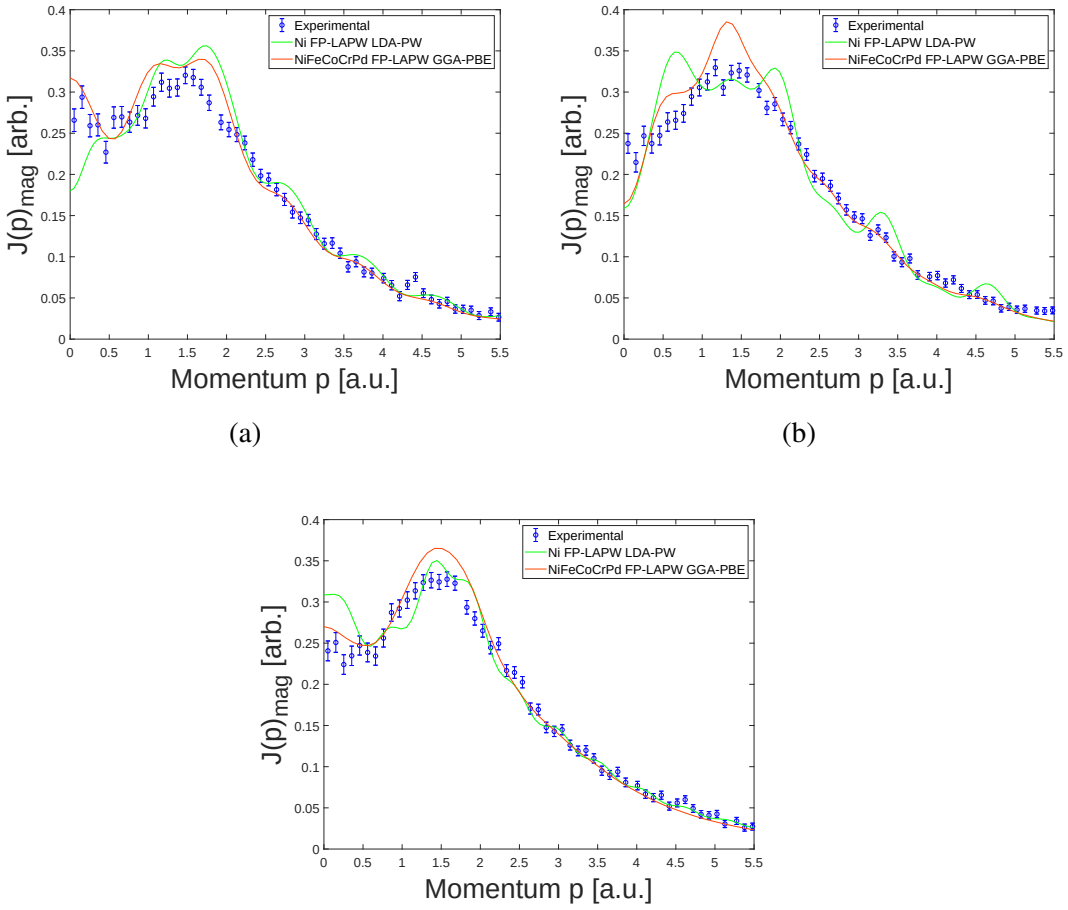

Figure 6.6: Theoretical MCPs of NiFeCoCrPd HEA from a SQS of 35 atoms (red) and Ni (green) and experimental MCPs of NiFeCoCrPd (blue) along (a) [1 0 0], (b) [1 1 0] and (c) [1 1 1] directions.

Also, four negative peaks are located near each one of the four K points in the central first BZ. Further, following the [0 1 0] and [0 0 1] axis there are four peaks in the neighbouring first BZs which correspond to the Umklapp contributions of the Γ point. In despite of the satisfactory agreement between both theoretical methods, the leaking of MDME from the central first BZ to their neighbouring first BZs is stronger in the SQS than in the KKR-CPA method. As in NiFeCoCr HEA, this behaviour can be explained by the lack of structural relaxation in the KKR-CPA method. The reduction in volume of the SQS means that in the momentum space the volume is bigger than its unrelaxed version in that space.

Fig. 6.8 depicts the theoretical MDME projections on the (1 1 0) plane. For the SQS, a dip can be found in the Γ point of the central first BZ. This feature is not well defined in the KKR-CPA. In

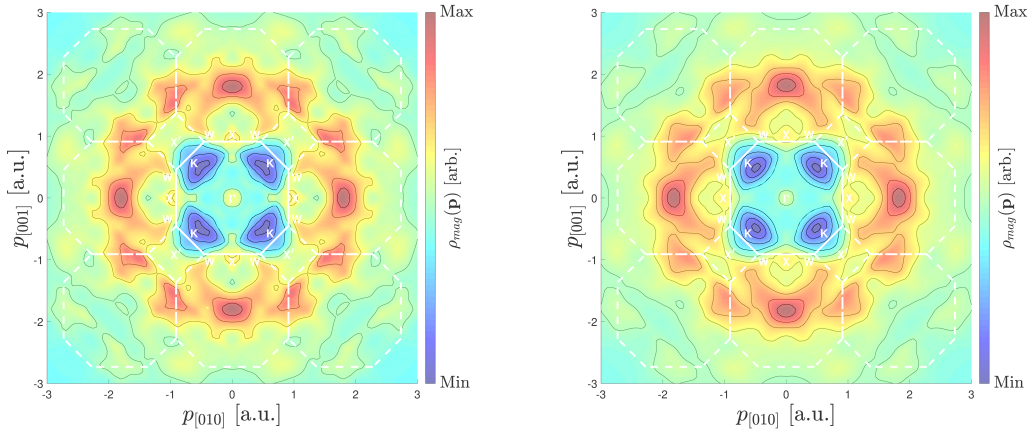

(a) (b)

Figure 6.7: Theoretical MDMEs of (100) NiFeCoCrPd HEA with (a) KKR-CPA method and (b) a SQS of 35 atoms. White lines are the first BZ boundary and high symmetry points are labelled with white letters.

contrast, four positive peaks appear in the KKR-CPA along the [$\bar{1}$ 1 0] and [0 0 1] axis but only two in the MDME with the SQS method in this zone. Also, four negative peaks are placed near each U point and two more near the K points in the central first BZ. Presumably these negative peaks are related with the delocalised s and d electrons of Cr due to its magnetic structure.

Furthermore, there are a couple of positive peaks around the Γ points in the nearest first BZs placed along [0 0 1] axis. They correspond to Umklapp contributions. Finally, there are a couple of positive peaks in each one of the remaining neighbouring zones located along [$\bar{1}$ 1 1] and [$\bar{1}$ $\bar{1}$ 1] directions. These peaks are distributed along the segment $\overline{LU}$ which is parallel to the segment $\overline{ULK}$ of the central first BZ. The most likely explanation to their appearance is the Umklapp scattering due to the geometry of the first BZ.

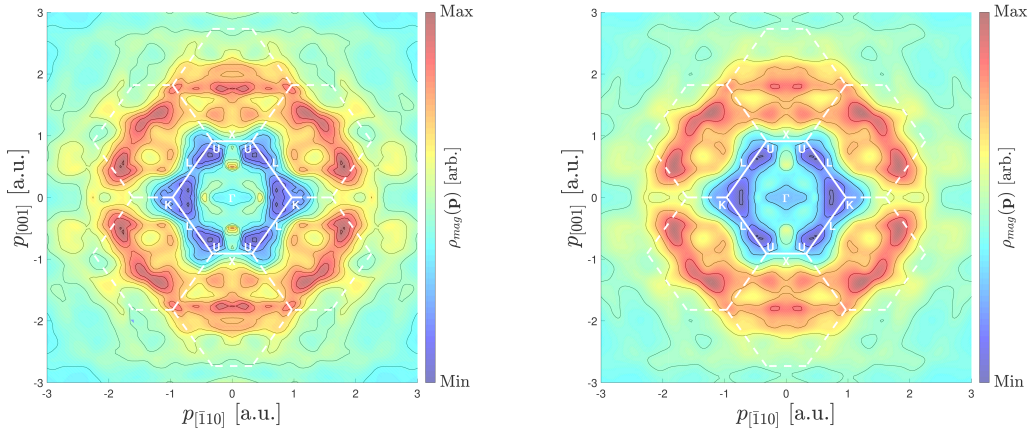

(a) (b)

Figure 6.8: Theoretical MDMEs of (110) NiFeCoCrPd HEA with (a) KKR-CPA method and (b) a SQS of 35 atoms. White lines are the first BZ boundary and high symmetry points are labelled with white letters.

6.5 Summary and Conclusions

The addition of Pd to the NiFeCoCr HEA matrix resulted in a higher spin magnetic moment than NiFeCoCr HEA. The KKR-CPA spin magnetic moment was bigger than the experimental value measured by magnetic Compton scattering, whereas the spin magnetic moment obtained by the SQS method was closest to the experimental one. The magnetic structure of NiFeCoCrPd HEA obtained by the SQS method is in agreement with the XMCD measurements done by our group. Also, the highest weight of Pd increase the lattice parameter and so it is possible to understand the differences in the DOS between a relaxed and an unrelaxed structure. Most of the filled states of Pd are far below the Fermi level, this increases considerably the smearing in the band structure in comparison to NiFeCoCr HEA.

The theoretical MCPs presented differences in the low momentum region in the three high symmetry directions. The LDA and GGA exchange-correlation functionals overestimated the MDME in the low momentum region for transition metals. On the other hand, in the high momentum region the MCPs fit well with the experimental data.

The discrepancies in the anisotropies shown that the one electron wave function model was not ideal to describe the MDME in the low momentum region. This is related to the neglect of the electron-electron correlation effects. However, the theoretical anisotropies were inside the error bars of the experimental data in the high momentum region.

The bi-dimensional projections of the MDME are qualitatively similar between the two theoretical methods. As in NiFeCoCr HEA, the lack of structural relaxation in KKR-CPA method can explain some differences in the MDME with the SQS method. The Umklapp peaks in neighbouring first BZs are recognisable, and they are related to the geometry of the first BZ.

Chapter 7

Conclusions

In the present work the chemical disorder present in NiFeCoCr HEA and NiFeCoCrPd HEA has been simulated by SQSs. Electronic structure calculations have been done to determine the magnetic structure and the MDME of these alloys. These calculations have been compared with the KKR-CPA method and validated with experimental data from magnetic Compton scattering and XMCD measurements.

In chapter five, NiFeCoCr HEA was simulated by SQSs of 32 atoms and 72 atoms. The SQSs shown a magnetic structure of NiFeCoCr HEA with the spin moments of Ni, Fe and Co aligned ferromagnetically and most of the spin moments of Cr coupled in an opposite direction. This result is in agreement with the XMCD measurements and other theoretical works. Also, the spin magnetic moments obtained by SQSs calculations were higher than the spin magnetic moment measured by magnetic Compton scattering.

Theoretical MCPs overestimated the experimental values in the low momentum region for [1 0 0], [1 1 0] and [1 1 1] high symmetry directions. However, the shape of the MCPs was well reproduced by the theory. The theoretical anisotropies between these high symmetry directions also overestimated the experiments in the low momentum region. Therefore, the MCPs are more isotropic than theory suggest. Also, the bi-dimensional projection of the MDME on the (1 0 0) plane shown four negative peaks localised near the K points of the central first BZ. On the other hand, a possible Cr clustering in NiFeCoCr HEA has been discarded by MCPs calculations.

In chapter six, NiFeCoCrPd HEA was simulated by a SQS of 35 atoms. The SQS shown a

magnetic structure of NiFeCoCrPd HEA with the spin moments of Ni, Fe, Co and Pd aligned ferromagnetically and most of the spin moments of Cr coupled in an opposite direction. This result is in agreement with the XMCD measurements and other theoretical works. Also, the spin magnetic moment obtained by the SQS method was close to experimental value measured by magnetic Compton scattering.

Additionally, the theoretical MCPs overestimated the experimental values in the low momentum region in the three high symmetry directions. Nevertheless, the shape of the MCPs was well reproduced by the theory. The theoretical anisotropies also overestimated the experimental values in the low momentum region. The bi-dimensional projection of the MDME on the (1 0 0) plane shown four negative peaks near the K points of the central first BZ.

In conclusion, SQS and KKR-CPA methods shown similar performance in the calculation of MCPs. These SQS results are promising and should be validated by a larger supercell size until achieve convergence of the MCPs. However, the KKR-CPA method is computationally cheaper than the SQS method. Therefore, future work must be focused in this direction at least for HEAs where the atomic displacements are small.

On the other hand, the measurement of the MCP along the [1 1 0] direction in the NiFeCoCr HEA should be repeated to improve the results.

It has been confirmed that the addition of Pd to NiFeCoCr HEA increased the spin magnetic moment of the resultant equiatomic alloy. In both HEAs, the projections of the MDME on the (1 0 0) plane shown four negative peaks near the K points of the central first BZ. Also, there were negative peaks around the central first BZ boundary in the projections of the MDME on the (1 1 0) plane. Additionally, these negative peaks looked more smeared in NiFeCoCrPd HEA than in NiFeCoCr HEA. These negative peaks can be related with the s and d delocalised electrons of Cr.

The electrical resistivity depends on the electron mean free path. The electron is scattered in a Cantor-Wu alloy by the potential originated via the chemical disorder, displacement fluctuations and local moments [151]. Then, the large smearing present in the negative peaks of the bi-dimensional projections of the MDMEs near the central BZ boundary remarks the important role of the minority spin band in the residual resistivity of NiFeCoCr and NiFeCoCrPd HEAs.

Furthermore, it has been demonstrated the impossibility of Cr clustering in NiFeCoCr HEA, and

thus it can be concluded that NiFeCoCr does not posses a ferrimagnetic structure in the strict sense.

The overestimation of the MCPs in the low momentum region of these transition metal HEAs is because the electron correlations are beyond the LDA and GGA approximations. Future work would involve calculations with the GW approximation and Dynamical Mean Field Theory (DMFT). Also, noncollinear spin calculations should be included in the EMD task of the Elk code to verify the existence of a noncollinear spin [140] ground state of NiFeCoCrPd HEA.

Bibliography

[1] J. B. KETTERSON, *The Physics of Solids*, Oxford University Press, Croydon, 1 ed. (2016).

[2] P. HOFMANN, *Solid State Physics*, Wiley-VCH, Darmstadt, 2 ed. (2015).

[3] T. S. CHOY, *Fermi Surface Data Base*, URL `http://www.phys.ufl.edu/fermisurface/` (2007).

[4] F. NIX AND W. SHOCKLEY, *Order-Disorder Transformations in Alloys*, Reviews of Modern Physics, **10**, 1–72 (1938).

[5] Y. KAKEHASHI, *Modern Theory of Magnetism in Metals and Alloys*, Springer, Heidelberg, 1 ed. (2012).

[6] J. W. YEH, *Alloy design strategies and future trends in high-entropy alloys*, JOM, **65**, 1759–1771 (2013).

[7] J. KOHANOFF, *Electronic Sructure Calculations for Solids and Molecules: Theory and Computational Methods*, Cambridge University Press, Cambridge, 1 ed. (2006).

[8] A. V. RUBAN AND I. A. ABRIKOSOV, *Configurational thermodynamics of alloys from first principles: Effective cluster interactions*, Reports on Progress in Physics, **71**, 1–30 (2008).

[9] M. J. COOPER, *Compton scattering and electron momentum determination*, Reports on Progress in Physics, **48**, 415–481 (1985).

[10] A. KOIZUMI, M. ITOU AND Y. SAKURAI, *Recent progress in the study of electronic states by means of Compton scattering*, The Japanese Society For Synchrotron Radiation Research, **25**, 153–165 (2012).

[11] M. A. G. DIXON, J. A. DUFFY, S. GARDELIS, J. E. MCCARTHY, M. J. COOPER, S. B. DUGDALE, T. JARLBORG AND D. N. TIMMS, *Spin density in ferromagnetic nickel: a magnetic Compton scattering study*, Journal of Physics: Condensed Matter, **10**, 2759–2771 (1998).

[12] Y. KAKUTANI, Y. KUBO, A. KOIZUMI, N. SAKAI, B. L. AHUJA AND B. K. SHARMA, *Magnetic Compton profiles of Fcc-Ni, Fcc-$Fe_{50}Ni_{50}$ and Hcp-Co*, Journal of the Physical Society of Japan, **72**, 599–606 (2003).

[13] M. W. BUTCHERS, *Magnetic Compton scattering studies of novel phases*, Ph.D. thesis, University of Warwick (2013).

[14] Y. ZHANG, G. M. STOCKS, K. JIN, C. LU, H. BEI, B. C. SALES, L. WANG, L. K. BÉLAND, R. E. STOLLER, G. D. SAMOLYUK, M. CARO, A. CARO AND W. J. WEBER, *Influence of chemical disorder on energy dissipation and defect evolution in concentrated solid solution alloys*, Nature Communications, **6**, 8736 (2015).

[15] W. R. FEHLNER AND S. H. VOSKO, *A Product Representation for Cubic Harmonics and Special Directions for the Determination of the Fermi Surface and Related Properties.*, Canadian Journal of Physics, **54**, 2159–2169 (1976).

[16] Y. F. YE, Q. WANG, J. LU, C. T. LIU AND Y. YANG, *High-entropy alloy: challenges and prospects*, Materials Today, **19**, 349–362 (2016).

[17] W. HUME-ROTHERY, G. W. MABBOTT AND K. M. C. EVANS, *The Freezing Points, Melting Points, and Solid Solubility Limits of the Alloys of Silver and Copper with the Elements of the B Sub-Groups*, Philosophical Transactions of the Royal Society A: Mathematical, Physical and Engineering Sciences, **233**, 1–97 (1934).

[18] E. SCHRÖDINGER, *Quantisierung als Eigenwertproblem*, Annalen der Physik, **384**, 489–527 (1926).

[19] A. SOMMERFELD AND H. BETHE, *Handbuch der Physik*, Julius Springer-Verlag, Berlin, 1 ed. (1933).

[20] U. MIZUTANI, *Hume-Rothery Rules for Structurally Complex Alloys Phases*, Taylor and Francis Group, Boca Ratón, 1 ed. (2011).

[21] N. F. MOTT AND H. JONES, *The Theory of the Properties of Metals and Alloys*, Claredon Press, Oxford, 1 ed. (1936).

[22] J. FRIEDEL, *Metallic alloys*, Il Nuovo Cimento, **7**, 287–311 (1958).

[23] P. W. ANDERSON, *Localized Magnetic States in Metals*, Physical Review, **75**, 542–544 (1961).

[24] H. HASEGAWA AND J. KANAMORI, *An Application of the Coherent Potential Approximation to Ferromagnetic Alloys*, J. Phys. Soc. Jpn., **31**, 382–393 (1971).

[25] Y. KAKEHASHI AND O. HOSOHATA, *CURIE-TEMPERATURE 'SLATER-PAULING CURVE'*, Journal de Physique, **49**, 73–74 (1988).

[26] W. HEISENBERG, *Über den anschaulichen Inhalt der quantentheoretischen Kinematik und Mechanik*, Zeitschrift für Physik, **43**, 172–198 (1927).

[27] S. C. WALLWORK, *Introduction to the Calculation of Structure Factors*, International Union of Crystallography, 12 (1980).

[28] T. NORSEN, *Foundations of Quantum Mechanics*, Springer International Publishing, Cham, 1 ed. (2017).

[29] U. SHMUELI, *International Tables for Crystallography, Volume B, Reciprocal Space*, Kluwer Academic Publishers, Bristol, 1 ed. (1993).

[30] M. SPRINGFORD, *Electrons at the Fermi surface*, Cambridge University Press, Cambridge, 1 ed. (1980).

[31] S. B. DUGDALE, *Life on the edge: a beginner's guide to the Fermi surface*, Physica Scripta, **91**, 053009 (2016).

[32] J. M. ZIMAN, *Electrons in metals: A short guide to the fermi surface*, Contemporary Physics, **3**, 241–256 (1962).

[33] K. JIN, B. C. SALES, G. M. STOCKS, G. D. SAMOLYUK, M. DAENE, W. J. WEBER, Y. ZHANG AND H. BEI, *Tailoring the physical properties of Ni-based single-phase equiatomic alloys by modifying the chemical complexity.*, Scientific reports, **6**, 1–10 (2016).

[34] G. A. LANDRUM AND R. DRONSKOWSKY, *The orbital origins of magnetism: from atoms to molecules to ferromagnetic alloys*, Angewandte Chemie, **39**, 1560–1585 (2000).

[35] F. E. LUBORSKY, J. D. LIVINGSTON AND G. Y. CHIN†, *Magnetic Properties of Metals and Alloys*, Elsevier B.V., 4 ed. (1996).

[36] C. P. POOLE, *Encyclopedic Dictionary of Condensed Matter Physics*, Elsevier Ltd, Kidlington, 1 ed. (2004).

[37] C. KITTEL, *Introduction to solid state physics*, Wiley, New York, 7 ed. ed. (2005).

[38] B. L. GYORFFY AND G. M. STOCKS, *Concentration waves and Fermi surfaces in random metallic alloys*, Physical Review Letters, **50**, 374–377 (1983).

[39] I. WILKINSON, R. J. HUGHES, Z. MAJOR, S. B. DUGDALE, M. A. ALAM, E. BRUNO, B. GINATEMPO AND E. S. GIULIANO, *Fermi surface nesting in disordered $Cu_{1-x}Pd_x$ alloys*, Physical Review Letters, **87**, 2164011–2164014 (2001).

[40] W. L. BRAGG AND E. J. WILLIAMS, *The effect of thermal agitation on atomic arrangement in alloys-I*, Proceedings of the Royal Society of London. Series A - Mathematical and Physical Sciences, **145**, 699–730 (1934).

[41] W. L. BRAGG AND E. J. WILLIAMS, *The effect of thermal agitation on atomic arrangement in alloys-II*, Proceedings of the Royal Society of London. Series A - Mathematical and Physical Sciences, **151**, 540–566 (1935).

[42] E. J. WILLIAMS, *The effect of thermal agitation on atomic arrangement in alloys-III*, Proceedings of the Royal Society of London. Series A - Mathematical and Physical Sciences, **152**, 231–252 (1935).

[43] H. A. BETHE, *Statistical Theory of Superlattices*, Proceedings of the Royal Society of London. Series A - Mathematical and Physical Sciences, **150**, 552–575 (1935).

[44] J. L. MORAN-LOPEZ AND L. M. FALICOV, *Ferromagnetism and Spatial Long-Range Order At the Surface of Binary Alloys.*, Journal of Physics C: Solid State Physics, **13**, 1715–1723 (1980).

[45] S. CHIKAZUMI, *Physics of Ferromagnetism*, Oxford University Press, Oxford, 1 ed. (1997).

[46] T. MIYAZAKI, *The Physics of Ferromagnetism*, Springer, Heidelberg, 1 ed. (2012).

[47] D. B. MIRACLE AND O. N. SENKOV, *A critical review of high entropy alloys and related concepts*, Acta Materialia, **122**, 448–511 (2017).

[48] R. KOZAK, A. SOLOGUBENKO AND W. STEURER, *Single-phase high-entropy alloys - An overview*, Zeitschrift fur Kristallographie, **230**, 55–68 (2015).

[49] B. S. MURTY, J. W. YEH AND S. RANGANATHAN, *High-Entropy Alloys*, Elsevier, Oxford, 1 ed. (2014).

[50] E. J. PICKERING AND N. G. JONES, *High-entropy alloys: a critical assessment of their founding principles and future prospects*, International Materials Reviews, **61**, 183–202 (2016).

[51] K.-Y. TSAI, M.-H. TSAI AND J.-W. YEH, *Sluggish diffusion in Co–Cr–Fe–Mn–Ni high-entropy alloys*, Acta Materialia, **61**, 4887–4897 (2013).

[52] J. W. YEH, *Physical Metallurgy of High-Entropy Alloys*, JOM, **67**, 2254–2261 (2015).

[53] R. K. MISHRA AND R. R. SHAHI, *Magnetic Characteristics of High Entropy Alloys*, Intech open, 67–80 (2018).

[54] R. M. MARTIN, *Electronic Structure*, Cambridge University Press, Cambridge, 1 ed. (2010).

[55] E. EBERHARD AND R. M. DREIZLER, *Density Functional Theory*, Springer, Heidelberg, 1 ed. (2011).

[56] M. P. DAS AND F. GREEN, *Revisiting the Fermi Surface in Density Functional Theory*, Journal of Physics: Conference Series, **726**, 1–14 (2016).

[57] K. HORN AND M. SCHEFFLER, *Electronic Structure*, Elsevier, Amsterdam, 1 ed. (2000).

[58] J. P. PERDEW AND A. ZUNGER, *Self-interaction correction to density-functional approximations for many-electron systems*, Physical Review B, **23**, 5048–5079 (1981).

[59] C. PISANI, *Quantum-Mechanical Ab-initio Calculation of the Properties of Crystalline Materials*, Springer, Heidelberg, 1 ed. (1996).

[60] J. PERDEW AND Y. WANG, *Accurate and simple analytic representation of the electron-gas correlation energy*, Physical Review B, **45**, 13244–13249 (1992).

[61] U. VON BARTH AND L. HEDIN, *A local exchange-correlation potential for the spin polarized case. I*, Journal of Physics C: Solid State Physics, **5**, 1629–1642 (1972).

[62] C. S. WANG, B. M. KLEIN AND H. KRAKAUER, *Theory of magnetic and structural ordering in iron*, Physical Review Letters, **54**, 1852–1855 (1985).

[63] D. CLATTERBUCK, *The ideal strength of iron in tension and shear*, Acta Materialia, **51**, 2271–2283 (2003).

[64] P. BAGNO, O. JEPSEN AND O. GUNNARSSON, *Ground-state properties of third-row elements with nonlocal density functionals*, Physical Review B, **40**, 1997–2000 (1989).

[65] S. K. MA AND K. A. BRUECKNER, *Correlation energy of an electron gas with a slowly varying high density*, Physical Review, **165**, 18–31 (1968).

[66] F. HERMAN, J. VAN DYKE AND I. ORTENBURGER, *Improved Statistical Exchange Approximation for Inhomogeneous many-electron systems*, Physical Review Letters, **22**, 807–811 (1969).

[67] J. P. PERDEW, K. BURKE AND M. ERNZERHOF, *Generalized Gradient Approximation Made Simple*, Phys. Rev. Lett., **77**, 3865–3868 (1996).

[68] Y. ZHANG AND W. YANG, *Comment on "Generalized Gradient Approximation Made Simple"*, Phys. Rev. Lett., **80**, 890–890 (1998).

[69] J. K. DEWHURST AND S. SHARMA, *Development of the Elk LAPW Code*, URL `http://www2.mpi-halle.mpg.de/fileadmin/templates/images/articles/elk/article.pdf` (2011).

[70] D. SINGH AND L. NORDSTRÖM, *Planewaves, Pseudopotentials and the LAPW Method*, Springer, New York, 2 ed. (2006).

[71] E. SJOSTEDT, L. NORDSTROM AND D. J. SINGH, *An alternative way of linearizing the augmented plane-wave method*, Solid State Communications, **114**, 15–20 (2000).

[72] U. MIZUTANI, *Introduction to the Electron Theory of Metals*, Cambridge University Press, Cambridge, 1 ed. (2001).

[73] J. PHILLIPS AND L. KLEINMAN, *New Method for Calculating Wave Functions in Crystals and Molecules*, Physical Review, **116**, 287–294 (1959).

[74] N. TROULLIER AND J. L. MARTINS, *Efficient pseudopotentials for plane-wave calculations*, Physical Review B, **43**, 1993–2006 (1991).

[75] P. GIANNOZZI, *Notes on pseudopotential generation*, URL `https://www.quantum-espresso.org/Doc/pseudo-gen.pdf` (2017).

[76] D. VANDERBILT, *Soft self-consistent pseudopotentials in a generalized eigenvalue formalism*, Physical Review B, **41**, 7892–7895 (1990).

[77] R. FLETCHER, *Practical Methods of Optimization*, Wiley, Chichester, 2 ed. (2000).

[78] P. GIANNOZZI, S. BARONI, N. BONINI, M. CALANDRA, R. CAR, C. CAVAZZONI, D. CERESOLI, G. L. CHIAROTTI, M. COCOCCIONI, I. DABO, A. DAL CORSO, S. DE GIRONCOLI, S. FABRIS, G. FRATESI, R. GEBAUER, U. GERSTMANN, C. GOUGOUSSIS, A. KOKALJ, M. LAZZERI, L. MARTIN-SAMOS, N. MARZARI, F. MAURI, R. MAZZARELLO, S. PAOLINI, A. PASQUARELLO, L. PAULATTO, C. SBRACCIA, S. SCANDOLO, G. SCLAUZERO, A. P. SEITSONEN, A. SMOGUNOV, P. UMARI AND R. M. WENTZCOVITCH, *QUANTUM ESPRESSO: A modular and open-source software project for quantum simulations of materials*, Journal of Physics Condensed Matter, **21** (2009).

[79] C. ZHANG AND M. C. GAO, *CALPHAD modeling of high-entropy alloys*, Springer, Cham, 1 ed. (2016).

[80] A. ZUNGER, S. H. WEI AND L. G. FERREIRA, *Special quasirandom structures*, Physical Review Letters, **65**, 353–356 (1990).

[81] A. VAN DE WALLE, P. TIWARY, M. DE JONG, D. L. OLMSTED, M. ASTA, A. DICK, D. SHIN, Y. WANG, L. Q. CHEN AND Z. K. LIU, *Efficient stochastic generation of special quasirandom structures*, Calphad: Computer Coupling of Phase Diagrams and Thermochemistry, **42**, 13–18 (2013).

[82] A. VAN DE WALLE, *Multicomponent multisublattice alloys, nonconfigurational entropy and other additions to the Alloy Theoretic Automated Toolkit*, Calphad: Computer Coupling of Phase Diagrams and Thermochemistry, **33**, 266–278 (2009).

[83] P. PHARISEAU, B. L. GYORFFY AND L. SCHEREI, *Electrons in Disordered Metals and Metallic Surfaces*, Plenum Press, New York, 1 ed. (1979).

[84] S. H. VOSKO, L. WILK AND M. NUSAIR, *Accurate spin-dependent electron liquid correlation energies for local spin density calculations: a critical analysis*, Canadian Journal of Physics, **58**, 1200–1211 (1980).

[85] M. J. COOPER AND P. E. MIJNARENDS, *X-Ray Compton Scattering*, Oxford University Press, Oxford, 1 ed. (2004).

[86] G. KONTRYM-SZNAJD, *Fermiology via the electron momentum distribution*, Transform, **599**, 1–22 (2009).

[87] S. B. DUGDALE, *Probing the Fermi surface by positron annihilation and Compton scattering*, Low Temperature Physics, **40**, 328–338 (2014).

[88] D. G. LOCK, V. H. C. CRISP AND R. N. WEST, *Positron annihilation and Fermi surface studies: a new approach*, J. Phys. F: Metal Phys., **3**, 561 (1973).

[89] Y. TANAKA, N. SAKAI, Y. KUBO AND H. KAWATA, *Three-Dimensional Momentum Density of Magnetic Electrons in Ferromagnetic Iron*, Physical Review Letters, **70**, 8–11 (1993).

[90] T. NAGAO, Y. KUBO, A. KOIZUMI, H. KOBAYASHI, M. ITOU AND N. SAKAI, *Momentum-density distribution of magnetic electrons in ferromagnetic nickel*, Journal of Physics Condensed Matter, **20** (2008).

[91] J. A. DUFFY, *What we can learn from magnetic Compton scattering: application to the determination of spin polarization*, Journal of Physics: Conference Series, **443**, 1–6 (2013).

[92] J. K. DEWHURST AND S. SHARMA, *The Elk Code*, URL `http://elk.sourceforge.net`. (2018).

[93] D. BENEA, S. MANKOVSKY AND H. EBERT, *Fully relativistic description of magnetic Compton profiles with an application to UFe_2*, Physical Review B - Condensed Matter and Materials Physics, **73**, 1–6 (2006).

[94] A. H. COMPTON, *A Quantum Theory of the Scattering of X-Rays By Light Elements*, The Physical Review, **21**, 483–502 (1923).

[95] P. A. M. DIRAC, *Relativity Quantum Mechanics with an Application to Compton Scattering*, Proceedings of the Royal Society A: Mathematical, Physical and Engineering Sciences, **111**, 405–423 (1926).

[96] P. A. M. DIRAC, *The Quantum Theory of the Electron*, Proc. R. Soc. A, **117**, 610 (1927).

[97] Y. YAZAKI, *How the Klein – Nishina formula was derived : Based on the Sangokan Nishina Source Materials*, Proceedings of the Japan Academy, **93**, 399–421 (2017).

[98] O. KLEIN AND T. NISHINA, *Uber die Streuung von Strahlung durch freie Elektronen nach der neuen relativistischen Quantendynamik von Dirac*, Zeitschrift fur Physik, **52**, 853–868 (1929).

[99] J. W. M. DU MOND, *Compton modified line structure and its relation to the electron theory of solid bodies*, Physical Review, **33**, 643–658 (1929).

[100] W. SCHÜLKE, *Solid State Information From the Fourier Transform of Compton Profiles.*, Japanese Journal of Applied Physics, **17**, 332–336 (1978).

[101] P. M. PLATZMAN AND N. TZOAR, *Magnetic scattering of x rays from electrons in molecules and solids*, Physical Review B, **2**, 3556–3559 (1970).

[102] N. SAKAI AND K. ONO, *Compton Profile Due to Magnetic Electrons in Ferromagnetic Iron Measured with Circularly Polarized Gamma Rays*, Phys. Rev. Lett., **37**, 351–353 (1976).

[103] K. SUZUKI, B. BARBIELLINI, Y. ORIKASA, S. KAPRZYK, M. ITOU, K. YAMAMOTO, Y. J. WANG, H. HAFIZ, Y. UCHIMOTO, A. BANSIL, Y. SAKURAI AND H. SAKURAI, *Non-destructive measurement of in-operando lithium concentration in batteries via X-ray Compton scattering*, Journal of Applied Physics, **119**, 0–6 (2016).

[104] A. H. COMPTON, *Absorption Measurements of the Change of Wave - Length accompanying the Scattering of X-rays*, Proceedings of the Royal Society, **46**, 897–911 (1923).

[105] A. H. COMPTON, *The Spectrum of Scattered X-rays*, Physical Review B, **22**, 409–413 (1923).

[106] J. E. MCCARTHY, M. J. COOPER, V. HONKIMAKI, T. TSCHENTSCHER, P. SUORTTI, S. GARDELIS, K. HAMALAINEN, S. O. MANNINEN AND D. N. TIMMS, *The cross-section for magnetic Compton scattering up to 1 MeV*, Nuclear Instruments and Methods in Physics Research, Section A: Accelerators, Spectrometers, Detectors and Associated Equipment, **401**, 463–475 (1997).

[107] G. SHARMA, K. B. JOSHI, M. S. DHAKA, M. C. MISHRA, R. K. KOTHARI AND B. K. SHARMA, *Compton profile and charge transfer study in intermetallic Ti-Al system*, Intermetallics, **19**, 1107–1114 (2011).

[108] A. ERBA AND C. PISANI, *Evaluation of the electron momentum density of crystalline systems from ab initio linear combination of atomic orbitals calculations*, Journal of Computational Chemistry, **33**, 822–831 (2012).

[109] JASRI 'INFORMATION AND OUTREACH SECTION', *Spring-8*, URL `http://www.spring8.or.jp/en/about_us/whats_sp8/faq/` (2018).

[110] M. BLUME, *Magnetic scattering of x rays (invited)*, Journal of Applied Physics, **57**, 3615–3618 (1985).

[111] M. J. COOPER AND J. A. DUFFY, *Spin densities studied in momentum space*, Journal of Physics and Chemistry of Solids, **61**, 345–352 (2000).

[112] D. M. MILLS, *Third-Generation Hard X-ray Synchrotron Radiation Sources*, Wiley, New York, 1 ed. (2002).

[113] M. SANO, S. TAKAHASHI, T. MOCHIZUKI, A. WATANABE, M. OURA AND H. KITAMURA, *Quantitative estimation of thermal contact conductance of a real front-end component at SPring-8 front-ends*, Journal of Synchrotron Radiation, **15**, 1–7 (2007).

[114] M. SANO, *High heat resistant front-end XY slit at SPing-8*, URL `https://medsi.lbl.gov/SysIncludes/retrieve.php?url=https://medsi.lbl.gov/files/page_145/Session_4_Front_Ends_Beamline_and_Utilities/High_Heat_Resistant_Front-end_XY_Slit_at_SPring-8_Sano_Mutsumi_PAPER.pdf` (2008).

[115] P. HOLM, *Relativistic Compton cross section for general central-field Hartree-Fock wave functions*, Physical Review A, **37**, 3706–3719 (1988).

[116] J. R. TAYLOR, *Error Analysis*, University Science Books, Sausalito, 2 ed. (1997).

[117] H. J. C. BERENDSEN, *A Student's Guide to Data and Error Analysis*, Cambridge University Press, Cambridge, 1 ed. (2011).

[118] E. ZUKOWSKI, S. P. COLLINS, M. J. COOPER, D. N. TIMMS, F. ITOH, H. SAKURAI, H. KAWATA, Y. TANAKA AND A. MALINOWSKI, *The magnetic Compton profile of ferrimagnetic $HoFe_2$*, Journal of Physics: Condensed Matter, **5**, 4077–4090 (1993).

[119] S. MU, Z. PEI, X. LIU AND G. M. STOCKS, *Electronic transport and phonon properties of maximally disordered alloys: From binaries to high-entropy alloys*, Journal of Materials Research, **33**, 2857–2880 (2018).

[120] B. CANTOR, I. T. CHANG, P. KNIGHT AND A. J. VINCENT, *Microstructural development in equiatomic multicomponent alloys*, Materials Science and Engineering A, **375-377**, 213–218 (2004).

[121] M. S. LUCAS, G. B. WILKS, L. MAUGER, J. A. MUÑOZ, O. N. SENKOV, E. MICHEL, J. HORWATH, S. L. SEMIATIN, M. B. STONE, D. L. ABERNATHY AND E. KARAPETROVA, *Absence of long-range chemical ordering in equimolar FeCoCrNi*, Applied Physics Letters, **100**, 1–5 (2012).

[122] B. LIU, J. WANG, Y. LIU, Q. FANG, Y. WU, S. CHEN AND C. T. LIU, *Microstructure and mechanical properties of equimolar FeCoCrNi high entropy alloy prepared via powder extrusion*, Intermetallics, **75**, 25–30 (2016).

[123] F. X. ZHANG, S. ZHAO, K. JIN, H. BEI, D. POPOV, C. PARK, J. C. NEUEFEIND, W. J. WEBER AND Y. ZHANG, *Pressure-induced fcc to hcp phase transition in Ni-based high entropy solid solution alloys*, Applied Physics Letters, **110**, 0119021–0119025 (2017).

[124] A. BANSIL, *Modern Band Theory of Disordered Alloys: Basic Concepts Including a Discussion of Momentum Densities*, Zeitschrift fur Naturforschung - Section A Journal of Physical Sciences, **48**, 165–179 (1993).

[125] H. C. ROBARTS, T. E. MILLICHAMP, D. A. LAGOS AND S. DUGDALE, *Extreme Fermi Surface smearing in a maximally disordered concentrated solid solution*, Phys. Rev. Lett., **124**, 1–6 (2020).

[126] G. KONTRYM-SZNAJD AND M. SAMSEL-CZEKATA, *Special directions in momentum space . I . Cubic symmetries*, Journal of Applied Crystallography, **44**, 1246–1254 (2011).

[127] Y. BRIF, M. THOMAS AND I. TODD, *The use of high-entropy alloys in additive manufacturing*, Scripta Materialia, **99**, 93–96 (2014).

[128] J. CORNIDE, M. CALVO-DAHLBORG, S. CHAMBRELAND, L. ASENSIO DOMINGUEZ, Z. LEONG, U. DAHLBORG, A. CUNLIFFE, R. GOODALL AND I. TODD, *Combined atom probe tomography and TEM investigations of CoCrFeNi, CoCrFeNi-Pd_x (x = 0.5, 1.0, 1.5) and CoCrFeNi-Sn*, Acta Physica Polonica A, **128**, 557–560 (2015).

[129] U. DAHLBORG, J. CORNIDE, M. CALVO-DAHLBORG, T. C. HANSEN, Z. LEONG, L. ASENSIO DOMINGUEZ, S. CHAMBRELAND, A. CUNLIFFE, R. GOODALL AND I. TODD, *Crystalline structures of some high entropy alloys obtained by neutron and X-ray diffraction*, Acta Physica Polonica A, **128**, 552–556 (2015).

[130] S. C. MIDDLEBURGH, D. M. KING, G. R. LUMPKIN, M. CORTIE AND L. EDWARDS, *Segregation and migration of species in the CrCoFeNi high entropy alloy*, Journal of Alloys and Compounds, **599**, 179–182 (2014).

[131] F. KÖRMANN, D. MA, D. D. BELYEA, M. S. LUCAS, C. W. MILLER, B. GRABOWSKI AND M. H. F. SLUITER, *'Treasure Maps' for Magnetic High-Entropy-Alloys From Theory and Experiment*, Applied Physics Letters, **107**, 1424041–1424045 (2015).

[132] M. S. LUCAS, L. MAUGER, J. A. MUOZ, Y. XIAO, A. O. SHEETS, S. L. SEMIATIN, J. HORWATH AND Z. TURGUT, *Magnetic and vibrational properties of high-entropy alloys*, Journal of Applied Physics, **109** (2011).

[133] C. NIU, A. J. ZADDACH, A. A. ONI, X. SANG, J. W. HURT, J. M. LEBEAU, C. C. KOCH AND D. L. IRVING, *Spin-driven ordering of Cr in the equiatomic high entropy alloy NiFeCrCo*, Applied Physics Letters, **106**, 1619061–1619064 (2015).

[134] M. CALVO-DAHLBORG, J. CORNIDE, J. TOBOLA, D. NGUYEN-MANH, J. S. WRÓBEL, J. JURASZEK, S. JOUEN AND U. DAHLBORG, *Interplay of electronic , structural and magnetic properties as the driving feature of high-entropy CoCrFeNiPd alloys*, Journal of Physics D: Applied Physics, **50**, 1–12 (2017).

[135] E. HARRIS-LEE, *Unpublished Thesis*, Ph.D. thesis, University of Bristol (2019).

[136] M. C. TROPAREVSKY, J. R. MORRIS, M. DAENE, Y. WANG, A. R. LUPINI AND G. M. STOCKS, *Beyond Atomic Sizes and Hume-Rothery Rules: Understanding and Predicting High-Entropy Alloys*, Jom, **67**, 2350–2363 (2015).

[137] J. I. LEE, H. S. OH AND E. S. PARK, *Manipulation of σ/k ratio in single phase FCC solid-solutions*, Applied Physics Letters, **109** (2016).

[138] H. SONG, F. TIAN, Q.-M. HU, L. VITOS, Y. WANG, J. SHEN AND N. CHEN, *Local lattice distortion in high-entropy alloys*, Physical Review Materials, **023404**, 1–8 (2017).

[139] D. R. LIDE, *CRC Handbook of Chemistry and Physics*, CRC Press, Boca Raton, 75 ed. (1994).

[140] K. JIN, S. MU, K. AN, W. D. PORTER, G. D. SAMOLYUK, G. M. STOCKS AND H. BEI, *Thermophysical properties of Ni-containing single-phase concentrated solid solution alloys*, Materials and Design, **117**, 185–192 (2017).

[141] M. S. LUCAS, D. BELYEA, C. BAUER, N. BRYANT, E. MICHEL, Z. TURGUT, S. O. LEONTSEV, J. HORWATH, S. L. SEMIATIN, M. E. MCHENRY AND C. W. MILLER, *Thermomagnetic analysis of $FeCoCr_xNi$ alloys: Magnetic entropy of high-entropy alloys*, Journal of Applied Physics, **113**, 1–4 (2013).

[142] F. TIAN, *Ab-initio Atomistic Simulation, Atomistic of Metals and Multicomponent Alloys*, Ph.D. thesis, KTH (2013).

[143] F. TIAN, L. K. VARGA, N. CHEN, L. DELCZEG AND L. VITOS, *Ab initio investigation of high-entropy alloys of 3d elements*, Physical Review B - Condensed Matter and Materials Physics, **87**, 1–8 (2013).

[144] V. POPESCU AND A. ZUNGER, *Effective band structure of random alloys*, Physical Review Letters, **104**, 1–4 (2010).

[145] P. V. C. MEDEIROS, S. STAFSTRÖM AND J. BJÖRK, *Effects of extrinsic and intrinsic perturbations on the electronic structure of graphene: Retaining an effective primitive cell band structure by band unfolding*, Physical Review B - Condensed Matter and Materials Physics, **89**, 0414071–0414074 (2014).

[146] K. MOMMA AND F. IZUMI, *VESTA: A three-dimensional visualization system for electronic and structural analysis*, Journal of Applied Crystallography, **41**, 653–658 (2008).

[147] W. KRAUS AND G. NOIZE, *POWDER CELL– a program for the representation and manipulation of crystal structures and calculation of the resulting X-ray powder patterns*, Journal of Applied Crystallography, **29**, 301–303 (1996).

[148] O. ENGLER AND V. RANDLE, *Introduction to Texture Analysis*, CRC Press, Boca Ratón, 2 ed. (2010).

[149] A. AGUAYO, I. I. MAZIN AND D. J. SINGH, *Why Ni_3Al is an itinerant ferromagnet but Ni_3Ga is not*, Physical Review Letters, **92**, 1472011–1472014 (2004).

[150] B. K. SHARMA, A. GUPTA AND H. SINGH, *Comptom profile of palladium*, Physical Review, **37**, 6821–6826 (1988).

[151] S. MU, G. D. SAMOLYUK, S. WIMMER, M. C. TROPAREVSKY, S. KHAN, S. MANKOVSKY, G. M. STOCKS, T. DIVISION, O. RIDGE AND O. RIDGE, *Uncovering electron scattering mechanisms in alloys possessing extreme disorder*, Arxiv, 1–19 (2019).

[152] T. BARUAH, R. ZOPE AND A. KSHIRSAGAR, *Full-potential LAPW calculation of electron momentum density and related properties of Li*, Physical Review B, **60**, 10770–10775 (1999).

[153] D. ERNSTING, D. BILLINGTON, T. D. HAYNES, T. E. MILLICHAMP, J. W. TAYLOR, J. A. DUFFY, S. R. GIBLIN, J. K. DEWHURST AND S. B. DUGDALE, *Calculating electron momentum densities and Compton profiles using the linear tetrahedron method*, Journal of Physics: Condensed Matter, **26**, 495501–495507 (2014).

[154] N. SHIOTANI, *Compton Scattering Study of Electron Momentum Density in Vanadium*, Journal of the Physical Society of Japan, **62**, 239–245 (1993).

[155] G. BAUER AND J. SCHNEIDER, *Electron correlation effect in the momentum density of copper metal*, Physical Review B, **31**, 681–692 (1985).

[156] D. A. CARDWELL, M. J. COOPER AND S. WAKOH, *Compton scattering studies of electron correlation effects in chromium*, Journal of Physics: Condensed Matter, **1**, 541–550 (1989).

[157] D. A. PAPACONSTANTOPOULOS, *Handbook of the Band Structure of Elemental Solids*, Springer, New York, 2 ed. (1986).

[158] H. CHEN, N. E. BRENER AND J. CALLAWAY, *Electronic structure, optical and magnetic properties of fcc palladium*, Physical Review B, **40**, 1443–1449 (1989).

[159] J. STAUNTON, J. POULTER, B. GINATEMPO, E. BRUNO AND D. JOHNSON, *Spin fluctuations in nearly magnetic metals from ab initio dynamical spin susceptibility calculations: Application to Pd and $Cr_{95}V_5$* , Physical Review B - Condensed Matter and Materials Physics, **62**, 1075–1082 (2000).

[160] U. DAHLBORG, J. CORNIDE, M. CALVO-DAHLBORG, T. C. HANSEN, A. FITCH, Z. LEONG, S. CHAMBRELAND AND R. GOODALL, *Structure of some CoCrFeNi and CoCrFeNiPd multicomponent HEA alloys by diffraction techniques*, Journal of Alloys and Compounds, **681**, 330–341 (2016).

[161] F. ZHANG, Y. TONG, K. JIN, H. BEI, W. J. WEBER AND Y. ZHANG, *Lattice Distortion and Phase Stability of Pd-Doped NiCoFeCr Solid-Solution Alloys*, Entropy, **20**, 1–9 (2018).

[162] A. MOOKERJEE AND D. D. SARMA, *Electronic Structure of Alloys, Surfaces and Clusters*, Taylor and Francis Group, London, 1 ed. (2003).

[163] D. BENEA, J. MINÁR, L. CHIONCEL, S. MANKOVSKY AND H. EBERT, *Magnetic Compton profiles of Fe and Ni corrected by dynamical electron correlations*, Physical Review B - Condensed Matter and Materials Physics, **85**, 4–7 (2012).

[164] J. W. TAYLOR, J. A. DUFFY, A. M. BEBB, J. E. MCCARTHY, M. R. LEES, M. J. COOPER AND D. N. TIMMS, *Spin-polarized electron momentum density distributions in the Invar system Fe_3Pt*, Physical Review B - Condensed Matter and Materials Physics, **65**, 2244081–2244088 (2002).